SCUOLA DI DOTTORATO
UNIVERSITÀ DEGLI STUDI DI MILANO-BICOCCA

Department of **Earth and Environmental Sciences**

Ph. D. program in **Chemical, Geological and Environmental Sciences**, **XXXVIII** cycle
Curriculum of **Geology**

Probing links between Cenozoic geodynamics and climate changes

Luca Castrogiovanni
Registration number: 789555

Tutor: **Nicola Piana Agostinetti**
Supervisor: **Pietro Sternai**

Coordinator: **Giovanni Marco Malusà**

Academic Year **2024/2025**

Abstract (English)

Paleoclimate archives allow the investigation of past climate changes, offering the unique chance to interpret and constrain future climate scenarios. Coupled carbon dioxide (CO_2) and temperature (T) trends affect Earth's system across time scales, resulting in non-linear interactions during Pleistocene glacial-interglacial cycles and Cenozoic climate. However, despite advances in constraining the absolute CO_2 budget through proxy reconstructions, so far works have overlooked the implications of underlying CO_2 fluxes. To address this question, the present work implements a Bayesian algorithm to invert temporal changes of paleo-CO_2 data to reconstruct continuous time histories of CO_2 source and sink fluxes. Coupled with a general formulation of the geological carbon cycle which links temporal changes of CO_2 to T trend, the algorithm is used in three different case studies. In the first study, the algorithm is validated through synthetic tests and applied to real case inversion of paleo CO_2 data from the Antarctic ice core of Dome Fuji, encompassing the last ~340 thousand years (kyrs). The study detects pulses of sources and sink fluxes during deglaciations and stability during glaciations. In the second study, the work extends the analysis to the last ~800 kyrs by inverting the paleo temporal CO_2 Antarctic ice core record of Dome C. The inversion reveals a shift in the carbon flux since ~400 kyrs, potentially ascribed to the effect of the Mid-Brunhes Transition. Quantitative and qualitative analyses hint at a driving role of the Solid Earth behind the detected shift, involving the interaction between sea level change and mid-ocean ridge volcanism. The third, final work deals with the inversion of a recent multi-proxy CO_2 reconstruction to reconstruct carbon flux time histories over the Cenozoic. The study detects high flux variability before ~34 million years (Myrs), potentially due to evolving geodynamic context of the Neo-Tethyan closure, and a stabilization thereafter. We ascribe the shift in the flux variability to stronger ice-albedo feedbacks since the onset of a perennial Antarctic ice cap ~34 million years ago (Ma). Finally, besides providing a novel tool and flux estimates to be used for constraining numerical forward models, this work leads the way to a new theoretical approach to the problem of carbon flux estimation.

Abstract (Italiano)

Gli archivi paleoclimatici permettono di indagare i cambiamenti climatici del passato, offrendo un'opportunità unica di interpretare e vincolare scenari climatici futuri. I trend accoppiati di anidride carbonica (CO_2) e temperatura influenzano il sistema Terra su diverse scale temporali dando origine a interazioni non lineari, come nel caso dei cicli glaciali-interglaciali pleistocenici o dell'era Cenozoica. Tuttavia, nonostante i progressi nella ricostruzione del bilancio di CO_2 tramite proxy paleoclimatiche, sono state finora trascurate le implicazioni legate ai flussi di CO_2. Per colmare questa lacuna, il presente lavoro introduce l'implementazione di un algoritmo bayesiano per l'inversione delle derivate temporali di CO_2 al fine di ricostruire serie temporali dei flussi di CO_2 in entrata e in uscita dalla superficie terrestre. Congiuntamente a un modello generalizzato del ciclo geologico del carbonio, il quale lega le variazioni temporali di CO_2 ai trend di temperatura, l'algoritmo viene qui applicato a tre diversi casi studio. Nel primo, l'algoritmo viene validato utilizzando test sintetici e successivamente applicato all'inversione reale dei dati di CO_2 provenienti dalla carota di ghiaccio antartica di Dome Fuji, relativa agli ultimi 340 mila anni. Lo studio rileva impulsi nei flussi superficiali durante le deglaciazioni e una loro stabilizzazione durante i periodi glaciali. Nel secondo studio, l'analisi viene estesa agli ultimi 800 mila anni utilizzando i dati della carota di ghiaccio di Dome C. L'inversione rivela un cambiamento nei flussi di carbonio a partire da 400 mila anni fa, potenzialmente legato alla Mid-Brunhes Transition. Analisi qualitative e quantitative suggeriscono un ruolo determinante della geosfera, in particolare l'interazione tra le fluttuazioni del livello marino e il vulcanismo di dorsale oceanica. Il terzo e ultimo studio riguarda l'inversione di una recente ricostruzione multiproxy dei valori superficiali di CO_2 per ottenere serie temporali dei flussi nel Cenozoico. L'analisi evidenzia un'elevata variabilità dei flussi prima di 34 milioni di anni fa, verosimilmente dovuta all'evoluzione del contesto geodinamico associato alla chiusura della Neo-Tetide, e una loro successiva stabilizzazione. Inoltre, la stabilizzazione dei flussi a partire da ˜34 milioni di anni fa è probabilmente dovuto al rafforzamento dell'interazione negativa tra ghiaccio e albedo successivo alla formazione della calotta polare antartica. Infine, oltre a fornire un nuovo strumento per la stima dei flussi di carbonio in superficie, utile anche ai fini di una migliore impostazione di modelli numerici, questo lavoro propone un nuovo approccio teorico al problema in analisi.

List of publications

As a **first author:**

- Castrogiovanni, L., Sternai, P., Agostinetti, N. P., & Pasquero, C. (2025). A reversible-jump Markov chain Monte Carlo algorithm to estimate paleo surface CO2 fluxes linking temperature to atmospheric CO2 concentration time series. Computers & Geosciences, 196, 105838.
- Luca Castrogiovanni, Pietro Sternai, Claudia Pasquero et al. Reconstructed late-Pleistocene CO2 fluxes reveal a shift in carbon cycling since the Mid-Brunhes transition, 22 October 2025, PREPRINT (Version 1) available at Research Square [https://doi.org/10.21203/rs.3.rs-7646995/v1].

As a **co-author:**

- Di Giulio, A., Sternai, P., Sacchi, R., & Castrogiovanni, L. (2025). Geodynamic pacemaker of Phanerozoic climate: A multivariate analysis of plate boundary processes and global temperature variations. Global and Planetary Change, 105173.

Contributions to conferences

As a **speaker:**

- "*Input and output fluxes of CO_2 during the late Quaternary*". International Union for Quaternary Sciences (INQUA) - Rome, Italy (July 2023).
- "*Input and output fluxes of CO_2 over the late Quaternary*". European Geosciences union (EGU) - Wien, Austria (April 2024).

As an **author:**

- Vaes, B., Sternai, P., Ostorero, L., Castrogiovanni, L., Gonzalez, C., & Donnadieu, Y. (2024, April). Numerical modelling of magmatic CO2 emissions from the Neo-Tethyan margin during the Early Cenozoic. In EGU General Assembly Conference Abstracts (p. 620).
- Sternai, P., Castelltort, S., Bouilhol, P., Vimpere, L., Ostorero, L., Ali, M., Castrogiovanni, L., Vaes, B., and Garzanti, E.: New constraints on the Neo-Tethyan carbon cycling and its forcing of early Cenozoic climate, EGU General Assembly 2024, Vienna, Austria, 14–19 Apr 2024, EGU24-4640, https://doi.org/10.5194/egusphere-egu24-4640, 2024.

Contents

1 Introduction **1**
- 1.1 Earth's Climate System . . . 2
  - 1.1.1 Atmosphere . . . 3
  - 1.1.2 Hydrosphere . . . 3
  - 1.1.3 Cryosphere . . . 4
  - 1.1.4 Biosphere . . . 5
  - 1.1.5 Geosphere . . . 5
- 1.2 Climate forcings . . . 6
  - 1.2.1 Astronomical forcings . . . 6
  - 1.2.2 Albedo . . . 7
  - 1.2.3 Atmospheric composition . . . 8
- 1.3 Carbon cycle . . . 8
- 1.4 Climate trends . . . 9
  - 1.4.1 Late Pleistocene . . . 10
  - 1.4.2 Cenozoic . . . 10

2 Aims and Methods **12**
- 2.1 Aims . . . 12
- 2.2 Methods . . . 13
  - 2.2.1 Reversible-jump Markov chain Monte Carlo algorithms . . . 14
- 2.3 The forward model . . . 16
- 2.4 Rj-McMC implementation for CO_2 flux estimation . . . 18
  - 2.4.1 Introduction . . . 19
  - 2.4.2 Data and Methodologies . . . 20
  - 2.4.3 Results . . . 27
  - 2.4.4 Discussion . . . 36
  - 2.4.5 Conclusion . . . 40
  - 2.4.6 Aknowledgments . . . 41
  - 2.4.7 Data availability . . . 41
  - 2.4.8 Code availability statement . . . 41

3 Carbon fluxes throughout the Late Pleistocene **42**
- 3.1 Introduction . . . 44
- 3.2 A marked shift in carbon cycling since MIS 10 . . . 45
- 3.3 Volcanic emissions conditioning surface CO_2 source fluxes? . . . 48

3.4 Figures . . . 49
3.5 Methods . . . 53
3.5.1 Data . . . 53
3.5.2 Rj-McMC algorithm . . . 53
3.5.3 Cross-correlation analysis . . . 57
3.5.4 Code availability . . . 57
3.5.5 Aknowledgments . . . 57
3.6 Figures methods . . . 58

4 Carbon fluxes throughout the Cenozoic **66**
4.1 Introduction . . . 67
4.2 Data and Methods . . . 69
4.2.1 Data . . . 69
4.2.2 Methods . . . 70
4.2.3 Prior information . . . 71
4.2.4 Computation time . . . 71
4.3 Results . . . 72
4.4 Discussion . . . 73
4.5 Conclusions . . . 76
4.6 Figures . . . 77

5 Conclusions **78**

6 Appendix **81**
6.1 Introduction . . . 83
6.2 Geodynamic drivers of phanerozoic global temperature: a short overview . . . 84
6.2.1 Global Temperature trends: models and proxies . . . 84
6.2.2 Oceanic ridges and spreading rate . . . 86
6.2.3 Continental magmatic arcs and subduction zones . . . 86
6.2.4 Suture zone length . . . 87
6.2.5 Continental Rifts Length . . . 88
6.2.6 Large Igneous Provinces . . . 88
6.3 Methods . . . 89
6.4 Results . . . 90
6.4.1 Cross-Correlation Functions between GAT and convergent plate margins dynamics . . . 90
6.4.2 Cross Correlation Functions between GAT and divergent plate margins dynamics . . . 92
6.5 Discussion . . . 94
6.6 Conclusions . . . 98
6.7 Acknowledgments . . . 99

Bibliography **100**

Acknowledgements **129**

Chapter 1

Introduction

Human-caused climate change has become a pressing issue over recent decades, highlighting the urgent need for governments to contain and mitigate its negative impact on both human and ecological communities. The latest IPCC report reveals anomalously high atmospheric greenhouse gases concentrations, with present-day levels of CH_4 and N_2O exceeding those of the last 800 kyrs, and CO_2 reaching unprecedented values in the last 2 Myrs [1]. Similarly, global average temperature (T) in 2001-2020 was 1.1°C higher than the period 1850-1950 [1], underscoring a rapid, warming trend in the current century. For this reason, governments and organizations involving experts in economics, risk management and politics have been working side by side with scientists to understand present-day climate change and estimate future scenarios accordingly. At a first-order, the scientific community has been addressing the problem following three main strategies: (1) examining the present by improving the quality and quantity of collected climatic data [2]; (2) projecting the future by implementing state-of-the-art models to reproduce highly confident scenarios [3] [4]; (3) investigating past climate trends to unveil how climate responded to climate forcings in the geological past[5] [6]. This doctoral work falls in the latter strategy.

The scientific discipline that studies past climate conditions is known as paleoclimatology (or palaeoclimatology), from the Greek word *study of past climate*. While occasional references during ancient and modern history suggest that philosophers and researchers were aware of the occurrence of past climate changes, it is only during the 19^{th} century, after the discovery of past glaciations, that scientists began to adopt a rigorous approach to the subject [7]. Since then, staggering advances

in climate theory and technologies have enabled the recovery of increasing number of paleoclimatic information [8], [9], [10], [11]. This information, stored in paleoclimate archives – geological sources (e.g., marine sediments, ice cores) containing direct or indirect information about past climate properties (e.g., surface CO_2, T) in the form of proxies – allow us to confidently constrain the Earth's climate history. Among the several, this PhD project mainly focuses on two of the most impacting climate factors, the surface CO_2 and T, and their evolution in the geological past.

The text structures as follows: the current Chapter, Chapter 1, covers an extended, although not exhaustive overview of the Earth's Climate System, including a short description of Earth's components (Section 1.1), the three main climate forcings (Section 1.2), mechanisms with which CO_2 circulates among Earth's reservoirs (Section 1.3), and a brief outline of CO_2 and T trends across time scales (Section 1.4). Chapter 2 begins with the formulation of the scientific problem (Section 2.1), providing a description of the methodologies adopted so far to address this question. It follows a general overview of the technique used (Section 2.2), the model formulation (Section 2.3), and the presentation of the first paper, which describes the developed algorithm and its application to a real case study (Section 2.4). Chapter 3 discusses the second paper, investigating climate trends over the last ˜1 Myr while Chapter 4 presents the most recent work, considering a third, different geological and climatic context. Chapter 5 contains the conclusions of this PhD, including implications for future research.

Finally, the reader is invited to approach this thesis not only as scientific research, but also as a narrative. While maintaining scientific rigor, the work aims to drive on a journey across different times, revealing known and yet unexplored aspects of past climate changes and offering new insights into the complex interactions among Earth's climate system components.

1.1 Earth's Climate System

As with every story worth telling, there is need for a setting. In this work, the setting is the Earth's Climate, a highly complex and interacting system consisting of five major spheres: the atmosphere, the hydrosphere, the cryosphere, the biosphere, and the geosphere [12] [13]. These components are in delicate balance each other's, with interactions occurring at time scales ranging from years to multimillion years. The following subsections shortly describe each of those spheres to introduce the key concepts discussed along the text.

1.1.1 Atmosphere

The atmosphere is the outer, gaseous envelop of Earth. It consists of different layers placed at different heights, each one characterized by different physical properties. These are, from bottom to the top: the troposphere, the stratosphere, the mesosphere, the thermosphere, and the exosphere. Most of the atmospheric processes occur in the troposphere which, in its present-day, dry concentration (i.e., without considering of the water vapor component) consists of: N_2 (78.01% volume mixing ratio), O_2 (20.9% volume mixing ratio), Ar (0.93% volume mixing ratio), and a small concentration of trace gases [12]. Some of these trace gases, such as the CO_2, have the property to trap the Earth's outcoming radiation, warming or cooling the surface if their concentration increases or decreases. However, the atmosphere is not stable and orbital rotation combined with air T differences generate winds, redistributing heat from low to high latitudes by convection [14]. In the short period (i.e., days to years), atmospheric motion regionally affects the surface ocean and define precipitation patterns. At 10^2 - 10^3 years time scales, changes in wind's strength in specific regions, such as the Subantarctic Zone, facilitates the CO_2 outgassing from the deep ocean [15]. Likely, enhanced atmospheric circulation deliveries more nutrients into the upper ocean, increasing the photosynthetic activity of marine vegetation and acting therefore as a CO_2 sink [16], [17]. From a chemical perspective, changes in the wind speed [18] and T gradients [19] at the air-sea surface interface vary the CO_2 exchange rate, with warmer (or cooler) surface waters enhancing the CO_2 release (or store) from (to) the ocean. Persistent humid and warm climate over long-term time scales (i.e. 10^4 – 10^7 years) affects the geosphere through weathering of rocks. On the contrary, sustained volcanic activity raises the atmospheric CO_2 content, warming climate [20], [21], [22].

1.1.2 Hydrosphere

The hydrosphere includes all those elements related to water at the liquid state such as oceans, seas, lakes, rivers, and, more broadly, the hydrological cycle. In this work, I primarily consider the contribution of the oceans – the second largest CO_2 reservoir after the geosphere [23]. Unlike the atmosphere, a typical ocean mass consists of only two main layers: at surface, a thin water layer rapidly (i.e., < 10^3 years) mixes CO_2 with the atmosphere; at depth, a thick water layer exchanges CO_2 with the surface at time scales of 10^3 - 10^4 years [23]. Density differences between these layers enable the stable water transit in few spots concentrated at high latitudes, establishing

a complex ensemble of deep-surface currents known as the "global ocean conveyor belt" [24]. In addition, winds and orbital motion generate coastal downwelling (or upwelling), where water sinks (or ascents) to (from) the deep ocean. Upwelling regions convey CO_2 to the surface, acting as a net atmospheric carbon source at time scales of 10^3 – 10^4 years [25]. From the biological realm, photosynthetic activity mediates the CO_2 transfer from surface to depth, reducing the atmospheric CO_2 content. This process is known as the "biological pump" [26], [16]. Changes in the amount of dissolved CO_2 affects ocean pH and alkalinity – the water's ability to neutralize acids -, where higher or lower concentrations of dissolved CO_2 leads to a shallowing or deepening of the CCD - the depth under which carbonate minerals dissolve [27]. Consequently, the different preservation of carbonate sediments at the sea-bottom affects the carbonate sediment burial, which is critical to long-term (i.e., > 10^4 years) CO_2 removal. Finally, changes in sea-level linked to water mass redistribution between the hydrosphere and continental ice have been suggested to affect the geosphere, triggering (or inhibiting) mid-ocean ridge volcanism during low (or high) sea level stands [28].

1.1.3 Cryosphere

The cryosphere involves all forms of water at the solid state, including sea ice, perennial continental glaciers, and polar icecaps. I will here focus only on the contribution of the continental ice and polar ice caps. Earth's climate is in a greenhouse or icehouse state depending on the presence or lack of glaciated poles [29]. The formation of polar ice caps is facilitated by the presence of polar located continents [30] , changes in oceanic and atmospheric circulation [31], and low surface CO_2 concentrations [32]. The direct implication is a stronger climate response to radiative forcing – the difference between the shortwave incoming solar radiation and the outgoing longwave Earth's radiation –, resulting in energy imbalances at surface over different time scales. Ice volume growth or reduction between 10^4 – 10^5 years affects the hydrosphere, the atmosphere and the biosphere through climate aridification or humidification, winds strengthening or weakening [33], inhibition or enhancement of the hydrological cycle [34], and an overall vegetation shift across latitudes [35]. In the last decade, negative or positive ice volume changes have been also associated with increased or decreased continental volcanic CO_2 emissions [21].

1.1.4 Biosphere

The biosphere includes all processes originated by living organisms, mainly including animals and plants. Here, I present only features related to the plant's realm, specifically land vegetation (i.e., forests, grass) and ocean phytoplankton – microalgae floating in the upper water layer. Land and water plants exchange CO_2 with the surface quasi-instantaneously through photosynthesis, photorespiration and respiration activity [36]. However, considerations made in this text limit to the photosynthetic process, the entry point of CO_2 to the biosphere. Based on their efficiency in the CO_2 sequestration, plants can be divided into C_3 and C_4 clades. C_3 plants fix CO_2 less efficiently than C_4, making the latter having an evolutionary advantage in arid or low CO_2 concentration conditions. At time scales of 10^3-10^4 years, vegetation spreading and latitudinal shifts following ice growth or retreat change the solar surface reflection and the CO_2 uptake, driving T variations [35], [37]. Higher nutrient availability delivered by winds to the surface ocean during low T periods enhances the CO_2 sequestration due to increase in the planktonic photosynthetic activity. This mechanism is known as the "Iron Fertilization Hypothesis" [38]. Finally, the turnover of plant species over time scales $> 10^5$ years and climate-controlled changes in the CO_2 capturing strategies dominate the biosphere long-term interaction with other Earth's System spheres [39].

1.1.5 Geosphere

Among the Earth's Climate System spheres, the geosphere takes center stage in this text, including all short- to long-term geological processes interacting with climate. Among the five components, it is the only capable of transferring material – including CO_2 – between the deep and Earth's surface [40]. At short time scales (i.e., < 10 years), single volcanic eruptions interact with the atmosphere by ejecting a large amount of tephra that penetrate the stratosphere [41], thus increasing the amount of solar radiation reflected and leading to a temporary climate cooling [22]. During the last decades, one of the most fascinating hypotheses in recent science has suggested that changes in ice volume can trigger or inhibit volcanic eruptions. This has become known as the "Deglacial Triggering Hypothesis" [42], and demonstrate that volcanic activity paces with orbital cycles at time scales of 10^4 – 10^5 years [21], [43], [44], [45]. Flood basalts ascent in the form of LIPs release large amount of CO_2 in a relatively short time (i.e., 10^5 years), usually leading to large mass extinctions [46], [47]. Plate driven evolution of volcanic arcs and mid-ocean ridges control the

CO_2 emissions over time scales > 10^6 years [20], [48]. Likely, tectonic opening or seaways closures affect the oceanic circulation [49] while reliefs regionally change the atmospheric paths and the hydrological cycle, driving monsoon intensification [50]. Multimillion-year interaction among the atmosphere, hydrosphere and surface geological features (e.g., orogens) changes weathering rate of silicate minerals, removing CO_2 from the surface. At the same time, CO_2 emissions following carbonate weathering and sulfide oxidation counterbalance the CO_2 silicate weathering sink [20].

1.2 Climate forcings

As a second ingredient for a story, there is need for elements to perturb the background conditions. Earth's Climate depends on the stability of the radiative budget [51] – the difference between the solar incoming and Earth's outcoming radiation – which ensures the equilibrium state. Nevertheless, external and internal factors known as climate forcings can occasionally perturb climate equilibrium, triggering nonlinear positive or negative feedback responses depending on whether they enhance or reduce T [52], [53]. Based on their intensity and/or duration, forcings can push the Earth's System beyond a threshold – tipping point –, shifting climate semi-permanently or permanently toward a different state [54]. Examples of natural tipping points in the geological past are the shift from greenhouse to icehouse conditions and periodical Pleistocene glacial-interglacial cycles. This work neglects discussions related to human caused forcings and feedbacks; instead, it describes three mains natural forcings characterizing most of the Earth's history: (1) astronomical forcings; (2) albedo changes; (3) variation in the atmospheric composition.

1.2.1 Astronomical forcings

Sun provides energy to Earth in the form of solar radiation, without which life would not be possible. Acting as a climate engine, it triggers most of the Climate System interactions described in Section 1.1. Net of other conditions, Earth's shape prevents the equal insolation distribution, causing latitudinal radiative imbalances: the tropics receive more radiation – and are therefore warmer – while polar regions show a negative balance, being colder [55]. The result is that T differences trigger atmospheric and oceanic movements across latitudes. However, received radiation does not only rely on the shape of the planet: through times, two main astronomical mechanisms largely affect climate evolution. These are the long-term (i.e., > 10^7 years) increase in luminosity associated

with natural star life cycles [56], and changes in Earth insolation due to orbital changes [57]. I will not consider the first mechanism given its long duration compared to time scales analyzed in this work. On the contrary, periodical orbital shifts defined as Milankovitch cycles involve the variation in the orbit's eccentricity, Earth's axis obliquity, and axial precession position with periodicities of 100-kyrs, 41-kyrs, and 23-kyrs, respectively. These leave a climate mark at time scales of 10^4 – 10^5 years [57], [58]. One of the most iconic examples of how orbital configurations affect climate are the Pleistocene (˜2.6 - 0.012 Ma) glacial-interglacial cycles, where insolation changes force the growth or retreat of polar icecaps, pushing climate toward warming or cooling periods [57], [58] (Section 1.4). However, although orbital parameters alone can trigger climate changes, Earth's internal responses, such as the distribution of ice and the atmospheric composition critically control the actual impact of insolation on climate, driving nonlinear feedback responses [59], [60], [61].

1.2.2 Albedo

If changes in the amount of incoming solar radiation can drive climate disruptions, the other side of the coin is that Earth does not absorb radiation evenly in space. The fraction of solar energy scattered by Earth back is known as planetary albedo and involves the nonlinear, combined effects of atmospheric and surface albedos [62]. Here, I consider only the contribution of the surface albedo given its longer term effect (i.e., > 10^2 years) than the more impacting atmospheric one [63]. The main reason for which surfaces reflect less or more solar radiation is their color: oceans and dense vegetation regions absorb more radiation than they reflect, leading positive climate feedbacks [64],[65]. On the contrary, clearer surfaces such as ice or deserts are highly reflective, thus leading negative feedbacks [66]. This makes the different repartition of water, ice, and land masses a critical aspect to consider when discussing climate evolutions, specifically in the context of an icehouse climate state, where perennial glaciated poles interact with orbital forcings making climate more sensitive to ice volume changes. For instance, variations in the surface albedo at high latitudes has been suggested to be a significant climate forcing during Pleistocene glacial-interglacial cycles [67], [68]. In this context, ice melting driven by insolation forcings exposes the ocean surface to solar radiation and drives poleward shift of continental vegetation, warming the atmosphere and leading to further melting. On the contrary, growth and extension of ice caps reinforce climate cooling by covering more ocean surface and reducing land vegetation surfaces. In its most extreme scenario, the runaway of ice-albedo feedback can lead to the complete melting of ice at poles or the complete

Earth's glaciation – the so-called "snowball Earth" – if ice overcomes a latitude threshold [69], [70]. Given an established negative feedback, what does prevent, then, the onset of a fully, icy Earth?

1.2.3 Atmospheric composition

One of the main features that makes Earth a habitable planet is the anomalously warm surface compared to other similar rocky planets (e.g., Mars). The non-reflected incident solar radiation is absorbed and emitted back to the space by Earth in the form of Outgoing Longwave Radiation (OLR). In its path back, the OLR interacts with some of the tropospheric gases, including the CO_2, trapping the OLR in the lower atmosphere and causing climate warming. This process is known as greenhouse effect [71]. However, whereas natural greenhouse effect is necessary to life, abrupt increases or long-term decline in the atmospheric CO_2 content amplify climate trends toward warmer or cooler conditions establishing complex feedback responses within Earth's climate spheres and forcings. For instance, insolation-mediated sea ice melting can trigger deep-ocean degassing of stored CO_2 [72], [73]. Likely, continental unloading following glacial melting can trigger volcanic eruptions, thereby emitting CO_2 into the atmosphere and causing further warming [21]. In this work, I approach the scientific problem (Section 2.1) from the perspective that changes in the atmospheric composition – particularly the CO_2 – represent a primary climate driver in the Earth's history.

1.3 Carbon cycle

The comprehension of how surface CO_2, here broadly defined as carbon, affects the climate system requires the understanding of how this compound circulates among Earth's reservoirs. Neglecting the contribution of single volcanic eruptions and fast weathering processes - for instance, of ultramafic rocks [74] - surface reservoirs involving the atmosphere, hydrosphere, biosphere, and cryosphere exchange carbon each other's faster than they commonly do with the geosphere [23]. This temporal mismatch develops two parallel carbon cycling paths, progressing at uneven speeds: at short-term, surface carbon exchanges rapidly force climate at time scales of 10 - 10^4 years; at the long-term, carbon transfer between the deep and Earth's surface occur at times longer than 10^4 years. This latter cycle goes by the name of geological carbon cycle [75] and is the standard definition used along this work.

When considering the geological carbon cycle, surface transfers are at the equilibrium and motion occurs only between the deep and Earth's surface. In its classical formulation, two key mechanisms drive the carbon cycling: the sustained volcanic activity from different geodynamic settings (e.g., subduction zones, mid-ocean ridges) is a CO_2 source, while the surface weathering of silicate minerals a CO_2 sink [20], [75], [76]. The latter, expressed by the net, following reaction:

$$CO_2 + CaSiO_3 \rightarrow CaCO_3 + SiO_2 \tag{1.1}$$

involves the delivery of CO_2 from the atmosphere to the deep ocean via biological shell calcification. Precipitated carbonates undergo burial and diagenetic processes, removing CO_2 from the Earth's surface. In this scenario, higher CO_2 levels accelerate silicate weathering rates due to enhanced precipitation in a high T, humid climate, whereas cooler climates inhibit the the CO_2 removal, allowing the accumulation of CO_2 and resulting warming [77]. Weathering of young mountain ranges such as the Himalayas and the uplift of plateaus affect atmospheric circulation, further facilitating the CO_2 drawdown [78]. This "weathering thermostat" [77] is believed to maintain habitable conditions and restore climate equilibrium when perturbations of the carbon cycle leads to abrupt increases of CO_2.

Besides the above however, other mechanisms take part in the long-term carbon cycling, included CO_2 emissions from the breakup of carbonates at depth due to metamorphic processes, carbonate and organic sediment weathering. On the contrary, burial of organic sediments is an additional CO_2 sink mechanism [20]. The ensemble of mentioned mechanisms, jointly to climate forcings described in Section 1.2 keep in steady motion the carbon cycle across time scales and define climate trends accordingly.

1.4 Climate trends

The main timeline of this work develops along two time scales, the Pleistocene and the Cenozoic, involving the onset of very different processes and interactions among carbon reservoirs. During both periods, paleoclimate archives show a tight relation between T and CO_2, making the understanding of the cause-effect relationship between them a non-trivial problem. In the following, I provide a short, general climate description of these two time scales.

1.4.1 Late Pleistocene

The Pleistocene begins ˜2.6 Ma with the formation of a stable Northern Hemisphere ice cap [60]. Climate information from this epoch reveal repeated shifts between cooler and warmer periods, respectively called glacials and interglacials. During these periods, atmospheric CO_2 and T rapidly increase when shifting from a glacial to an interglacial phase, and slowly reduce entering a glacial phase, thus defining an asymmetric "saw-tooth" trend [79], [9], [8]. Spectral analyses show that glacial-interglacial cycles pace with orbital variations [79], which act as a primary climate forcing during this time scale. However, irregular CO_2 and T trends and changes in the dominant periodicity, for instance during the Mid-Pleistocene Transition (MPT), when glacial-interglacial cyclicity shifted from ˜41-kyrs to ˜100-kyrs, raised a strong debate against a fully driving role of orbital forcing, rather suggesting internal, nonlinear feedback responses [80]. With this regard, the ensemble of hypotheses explaining the abrupt deglacial CO_2 increases involve stronger ocean ventilation of the Southern Ocean [81], formation of subantarctic upwelling regions associated with shifts in wind position [82], carbon release from permafrost thawing [83], and increased volcanism linked to ice unloading of magmatic systems [21]. On the contrary, theories to explain the CO_2 removal come from land and marine biological processes, such as iron fertilization during late glacial phases, increased photosynthetic activity [16], [84], and fast, terrestrial weathering during the interglacial [85].

1.4.2 Cenozoic

The Cenozoic (˜66 - 0 Ma) is the most recent Era. Characterized by a first phase of warming, proxy records show an overall, almost stable decline in CO_2 and T since ˜50 Ma, driving the latest transition from greenhouse to icehouse conditions after the onset of an Antarctic ice cap ˜34 Ma [86]. Two key mechanisms have been invoked to unravel the polar ice sheet formation: on the one hand, the tectonic opening of the Tasmanian gateway and the Drake Passage may have facilitated the thermal isolation of Antarctica by establishing the Antarctic Circumpolar Current (ACC) [31], [87]. On the other hand, a reduction in CO_2 concentration may have promoted the ice formation which, reinforced by orbital cycles, allowed the onset of a stable Southern Hemisphere ice cap [86]. To explain the overall Cenozoic decline in CO_2 and T, classic, opposing mechanisms are the reduction in CO_2 emissions linked to volcanic arc extinction in the context of India-Eurasia subduction before

˜34 Ma [48], and enhanced silicate weathering following Himalaya's formation and Tibetan Plateau uplift since ˜10 Ma [78].

Superimposed to the background cooling, abrupt events of warming and longer periods - optima - of climate amelioration punctuate the overall Cenozoic trend [10]. The most prominent are the Paleocene-Eocene Thermal Maximum (PETM) ˜56 Ma, the Early Eocene Climatic Optimum (EECO) between ˜54-49 Ma, the Middle Eocene Climatic Optimum (MECO) ˜40 Ma, and the Middle-Miocene Climatic Optimum (MMCO) ˜15 Ma. Causes of these "aberrations" [10] remain debated, including LIPs processes [47], internal feedbacks related to orbital forcings [88], [89], gas hydrate release [90], or volcanic flare-ups of the Neo-Tethyan Margin [91].

Chapter 2

Aims and Methods

2.1 Aims

Despite substantial advances in reconstructing past atmospheric CO_2 levels and their evolution in time, key uncertainties remain in our understanding of the carbon cycle. While proxy records retrieve the absolute budget of CO_2, we lack of clear constraints on temporal CO_2 changes - fluxes - which could unveil underlying Earth's system responses to climate forcings. In literature, classic attempts to reproduce paleo CO_2 fluxes mainly rely on the use of paleo plate modeling tools which indirectly infer flux trends based on the amount of lithosphere that is consumed or produced through geological times [92], [93], [94]. Other ways to degassing estimates come from forward models, capable to predict the outcome fluxes through the solution of prescribed physical laws [6]. To this aim, models of increasing complexity have been developed, including box [95] and spatially-informed models [96]. While box models are usually fast to compute, allowing deep time climate studies, spatially-informed ones require high computational costs, preventing their use for long-term simulations. A trade-off method, incorporating benefits from both model types has been recently developed by [6]. However, forward models remain intrinsically dependent on subjective input choices, usually leading to analysis perception bias.

To overcome this issue, inversion approaches involving the use of output CO_2 data and the parametrization of a forward model to quantify past carbon fluxes can be a valuable solution. However, past attempts focused on linearized methods to retrieve paleoclimate information in the

near past [97], [98], which can be unsuitable to reproduce long-term, non linear CO_2 trends. In the geological past, works incorporating inverse modelling strategies were used to reconstruct paleo-CO_2 concentrations during the Pleistocene [99] and Cenozoic [100]. However, their study do not explicitly focus on CO_2 flux trends and do not take into account for the T-CO_2 relationships. In this work, I address the problem of carbon flux estimation by implementing a state-of-the-art inversion algorithm coupled to a formulation of the geological carbon cycle to invert on temporal changes of CO_2 (i.e., $\frac{dC}{dt}$). By minimizing the amount of subjective choices, the use of this methodology allows to robustly data-infer temporal evolution of CO_2 flux changes and reconstruct continuous time histories of source and sink CO_2 fluxes.

2.2 Methods

After defining the main challenges of this work, the present section introduces methodological notions and developed tools used to address the scientific question. As a general definition, inverse modelling refers to the process of inferring unknown features (e.g., carbon fluxes) based on observational data. The approach covers a wide range of Earth science problems, especially in geophysics, where surface collected seismic, electromagnetic, and gravity data allow to infer the distribution of subsurface properties, usually defined as "Earth Models" [101], [102]. In this study, the Earth model is the distribution of changes in the source and sink CO_2 fluxes over a certain time scale.

In solving an inverse problem, three key properties should be carefully considered: existence, stability, and uniqueness of the inverse solution [103]. The existence refers to the feasibility of solving the mathematical model used to fit the observed data. The stability guarantees that noise in the observed data do not result in drastic changes in the solution [104]. The uniqueness ensures that only a single parametrized model fits the observed data [105]. However, geophysical problems usually violate one or more of the above conditions, thus defining an ill-posed problem [104]. For instance, multiple combinations of CO_2 sources and sinks can produce the same $\frac{dC}{dt}$ signal, making the understanding of the actual fluxes unclear [106]. To address the problem of non-uniqueness, endless analytical strategies have been developed, including simple least-squares regressions, optimization, regularization, which are suitable when data linearly relate with the model and/or express low dimensionality in the model space - the abstract space containing all model solution of the physical system studied [107], [108]. On the other hand, probabilistic methods including random search

(e.g., Monte Carlo), simulated annealing, and genetic algorithms can solve nonlinear problems involving high dimensional models [109]. Given the nonlinearity of the climate system in relation to CO_2 changes, in this work the choice is to address the problem of carbon flux quantification by implementing a probabilistic inverse method based on a reversible-jump Markov chain Monte Carlo (rj-McMC) algorithm [110].

2.2.1 Reversible-jump Markov chain Monte Carlo algorithms

A general definition of Monte Carlo (MC) method is the use of a pseudorandom sampling in a parameter space - space of all possible parameter values defining a mathematical model - in order to return unkown information of interest [111]. This is possible through a stochastic sampling, exploring both realistic and unrealistic parameter space regions. While the non-uniqueness of the solution does not ensure a single model parametrization to represent the inverted data, MC algorithms allow to directly sample the parameter space without needing an objective function, generally devised to minimize the difference between model generated (i.e., synthetics) and observed data [112]. This prevents to fall in local maxima - regions which are not the most probable solution of the inverse problem [111] - by pseudorandomly sampling thousands to millions of possible representations of the Earth Model. Essentially, at each sampling a pure MC algorithm computes the picked parameters in a forward model to generate synthetic data and compares them with the observed ones through a likelihood function. Finally, the ensemble distributions arising from collected models should summarize the most representative parameter values for the observed data.

However, MC methods should not be seen as a panacea [111]. One of the risks is a too extensive sampling, preventing the effective exploration of promising parameter space regions. This, usually occurring if model dimensionality exceeds 10 parameters [113], would make the process long and computational expensive, limiting the convergence to the solution. To overcome the issue, developed strategies include the implementation of Markov chain Monte Carlo algorithms (McMC) [114] where a sampled model only depends on the previous one. This allows to obtain information about the nature of the target distribution effectively [115]. From a probabilistic perspective, most of McMC implementations operate in a Bayesian framework [116], meaning that the algorithm samples a posterior probability distribution (PPD), given by the product between prior information and observed data according to the following equation:

$$p(m|d) \propto p(m)L(d|m) \tag{2.1}$$

Where $p(m|d)$ represents the PPD of the model m given the data d, $p(m)$ the prior probability distribution on model parameters, and $L(d|m)$ the likelihood function, which measures the probability to retrieve the data d given the model m. In other words, it measures how comparable are synthetic data to the observed ones. Thus, the PPD describes the probability distribution of model parameters conditioned by the experimental data and prior knowledge about the physical process itself [116]. In this study, prior knowledge mainly relates to the physical law used to define carbon fluxes (i.e., the forward model definition) and assigned constraints to the parameter space during the sampling process. To sample effectively the PPD, different criteria are used including the well known Metropolis sampler [114] that involves the transition from a current model m_{curr} to a candidate model m_{cand} [117] whose acceptance or rejection only depends on m_{curr}. In the first case, m_{cand} becomes the current model and the sampling continues from such model. On the contrary, if the candidate model is rejected, m_{curr} is kept as the current model, participating twice in the final ensemble of sampled models. Criteria used for acceptance or rejection rely on the result of the likelihood function: if $L(m_{cand}) > L(m_{curr})$, the candidate model is accepted with a probability $\alpha = 1$. However, if $L(m_{cand}) < L(m_{curr})$, the candidate model can still be accepted, but with reduced probability equal to $\alpha = \dfrac{L(m_{cand})}{L(m_{curr})}$. Setting of this feature largely differentiates McMCs from best fit algorithms, as it prevents the chain from getting trapped in local maxima and represents a solution to the non-uniqueness issue.

However, although McMC methods are already suitable to constrain most of non linear inverse problems, a further difficulty to non-uniqueness arises when dealing with model complexity [101]. In the framework of this study, parametrization of the complexity involves the a priori, subjective definition of times at which source and sink fluxes may change. This assumption can bias the solution in two opposite ways: if the assumed model complexity is high, the McMC algorithm may overfit data, involving also a higher computational cost; if assumed model complexity is low, the algorithm may not adequately fit the observed data, preventing the acceptable understanding of the investigated problem. For this reason, almost 30 years ago a reversible-jump (rj) component to McMC algorithm was implemented by [110] to ensure that model complexity was inferred directly from data, thus avoiding the over or under parametrization of the inverse problem. This work

adopts a rj-based implementation to address the scientific problem.

2.3 The forward model

Once given a brief overview of the class of rj-McMC algorithms, I formally provide in this section the forward model definition used along the work. Forward models represent the physical assumption we use to describe the observed data and its definition is critical to achieve a suitable model parametrization. Here, we link temporal changes of CO_2 to T time series according to the following equation:

$$\frac{dC}{dt} = \gamma - \beta T \tag{2.2}$$

where the unknown γ and β model parameters represent the source and sink amplifier terms, respectively. T is the temperature time series which, as defined by the classical definition of the geological carbon cycle, drive temporal decline of CO_2 (Section 1.3). By this formulation, γ and βT encapsulate all possible source and T-dependent sink mechanisms, preventing the disentanglement of individual reservoir contributions to flux changes. In addition, T-dependent processes such as the oxidation of organic matter [118], sulfide-assisted weathering of carbonates [119], or biological processes [120] have been recently suggested to perturb the geological carbon cycle acting as a carbon source. However, although potentially contributing to temporal CO_2 variations, these processes lack definitive understanding and consensus [121], [118]. Consequently, I do not consider more complex model definitions in this thesis and instead adopt the simpler, widely accepted formulation of Eq.2.2.

Finally, Eq.2.2 allows: (1) to filter short-term mechanisms (i.e. $< 10^4$ years), allowing to explore the interaction between the Earth's surface and its solid Earth component; (2) to fastly converge to the solution given the reduced number of model parameters. Noteworthy, T time series is not treated as a datum in the forward computation, but as a supporting information. For this reason, retrieved changes (or stability) of both γ and β during the flux reconstruction reveal times of $\frac{dC}{dt}$ - T decoupling (or coupling), involving the inability (or ability) of the T time series to directly reproduce temporal CO_2 changes. Hence, although simply defined, this feature can significantly increment our knowledge about CO_2 - T relations over past climate trends. In the following section, I present my first study, including the description and validation of the implemented rj-McMC algorithm and its application in a real case study inverting on atmospheric CO_2 data from the Antarctic ice core

record of Dome Fuji.

2.4 Rj-McMC implementation for CO_2 flux estimation

CO_2 and T changes well correlate in the geological record, making the assessment of causative links between these two climate variables a non-trivial task. The unclear understanding of leading climate forcing factors thus prevents a thorough representation of the climate system. Through the following paper, I address this apparent "chicken and egg" problem by presenting the implementation of a rj-McMC algorithm which is capable to estimate paleo-source and sink CO_2 fluxes linking T changes to atmospheric CO_2 time series. The study, published in *Computers&Geosciences* in February 2025 [122], describes the newly developed method and validates it through synthetic tests. As a key to unlock unknown features of the climate system, its application to the real case inversion on $\frac{dC}{dt}$ record from Dome Fuji ice core (i.e., the last ˜340 kyrs) represents a first step for science toward a more reliable data-inferred quantification of carbon fluxes in the geological past. The possibility to quantify carbon fluxes using paleoclimate CO_2 data and, at the same time, detect timing at which carbon trends disentangle from T changes provides robust constraints for future modelling studies.

A reversible-jump Markov chain Monte Carlo algorithm to estimate paleo surface CO_2 fluxes linking temperature to atmospheric CO_2 concentration time series

Castrogiovanni L.[1], Sternai P.[1], Piana Agostinetti N.[1], Pasquero C.[1]

[1]Department of Earth and Environmental Sciences, University of Milano-Bicocca, Italy.

Status: Published in *Computers&Geosciences*

Abstract

Future goals and strategies for mitigating ongoing climate changes rely on the understanding of the global carbon cycle and its connections to climate. Evidence from ice cores regarding past atmospheric CO_2 and temperature changes through glacial-interglacial oscillations provide crucial insight into the natural variability of carbon cycling. However, poor constraints on atmospheric CO_2 input and output fluxes limit our quantitative understanding of late Pleistocene carbon cycling

and climate changes. In this study, we describe an inversion method based on a reversible-jump Markov chain Monte Carlo (rj-McMC) algorithm and a general formulation of the geological carbon cycle to estimate paleo-fluxes of CO_2. We present results from two synthetic tests and a real case study based on data from the ice core of Dome Fuji. Results from synthetic tests demonstrate the capability of the algorithm to retrieve reliable estimates of atmospheric CO_2 input and output fluxes inverting the time derivative of the atmospheric CO_2 record and using its temperature time series as a further constraint. Results from the Dome Fuji case study underscore systematic pulses of input CO_2 fluxes into the atmosphere during deglaciations predating peaks of T and output CO_2 fluxes by 2.5 kyrs. The retrieved surface source and sink CO_2 fluxes as well as future applications of the algorithm presented here will provide new insights to assess past climate driving mechanisms and inform projections of future climatic trajectories.

2.4.1 Introduction

Climate changes result from multiple forcing factors that interact across timescales [123], [124], [125], [126]. For instance, orbital parameters influence solar irradiation [127], [128], and the cascading effects on the global biogeochemical cycles [129], [130], [85], [131], [132], particularly that of carbon as CO_2 due to its greenhouse effects, affect climate and, in turn, are regulated by climate changes [133] [134]. Understanding the global carbon cycle and its connections to climate is increasingly important within the current geopolitical context, as it enhances our ability to predict Earth system responses to ongoing anthropogenic pressures. Geological archives provide invaluable insights into the natural variability of carbon cycling under different conditions. A classic example is the glacial-interglacial changes in atmospheric CO_2 concentrations which, ever since the first records were retrieved from ice cores [135], [136], has spurred significant advancements in our understanding of carbon cycling dynamics. However, while proposed mechanisms such as Southern Ocean dynamics [82], deep water isolation [137], the biological pump [138], and feedback processes involving continental ice extent, sea level changes, and global volcanism [21], [28], [139] contribute to the complexity of the carbon cycling and climate system, an overarching explanation for the oscillations in late Pleistocene atmospheric CO_2 concentrations and associated glacial-interglacial climate variability has yet to be found. Poor constraints on the surface fluxes of CO_2 are currently one of the greatest limitations to our quantitative and process-based understanding of ever-increasing measures of late Pleistocene atmospheric CO_2 concentrations in ice-cores [140], [141], [142], [143].

On the short term (i.e., centennial timescales), recent CO_2 fluxes have been assessed through linear regression-based models [144], [145], [98], [97], but these models are unsuited for assessing the highly non-linear climate variability of late Pleistocene glacial-interglacial cycles [146], [147]. At geological time scales (i.e., $> 10^3$ yrs), direct evidence from magmatic/metamorphic petrology allows constraining the background steady-state CO_2 degassing fluxes from the Solid Earth into surface reservoirs [148], [149], [150], [151]. Similarly, analyses of the sedimentary record allow assessing the output and input fluxes of atmospheric CO_2 via weathering of silicate minerals or sulfide and organic carbon within sediments [152], [77], [153], [154]. However, a continuous reconstruction of the global input and output fluxes of surface CO_2 via direct investigation of the geological archives is beyond possibilities. Here, we describe a novel inversion approach based on a reversible-jump Markov chain Monte Carlo (rj-McMC) algorithm to estimate atmospheric input and output fluxes of CO_2 from ice core data. The inversion approach is here tested with a simple formulation of the geological carbon cycle [155] that focuses on the longer term (i.e., $> 10^3$ yrs) paleo-CO_2 exchanges between the surface and Solid Earth. In the following, we first present the methodology, including an overview about rj-McMC algorithms, the required data, and the forward model. We then illustrate results obtained from two synthetic tests and a real case study that uses atmospheric CO_2 measurements from the Fuji Dome ice core [140], [156]. Finally, we discuss the modeled paleo CO_2 fluxes over the last 340 kyrs, the new opportunities for the interpretation of paleoclimate time-series that our algorithm provides and possible future applications involving more complex formulations of the geological carbon cycle that address the shorter-term (i.e., $\leq 10^3$ yrs timescales) CO_2 exchanges among surface reservoirs.

2.4.2 Data and Methodologies

2.4.2.1 Data

Air bubbles enclosed in ice-cores cavities allow measuring past atmospheric concentrations of climate-impacting greenhouse gases such as CO_2, and thus provide reliable constraints for reconstructions of paleo-climate conditions throughout recent glacial-interglacial cycles [157], [136]. In addition, independent time-histories of atmospheric temperature (T) obtained from analyses of water isotopes ratio (δD and $\delta^{18}O$), which are defined as the relative abundance of heavy to light isotope with respect to the Vienna Standard Mean Ocean Water value in ice-cores [158], [159] allow

to further constrain estimates of paleo-climate conditions. As we demonstrate based on synthetic data and measurements from the Dome Fuji ice-core (Fig. 2.1) [140], [156], the new formal method presented here enables to retrieve paleo atmospheric input and output fluxes of CO_2 using the time derivative of measured CO_2 concentrations (i.e., $\frac{dC}{dt}$) as data and the T record as a further constraint.

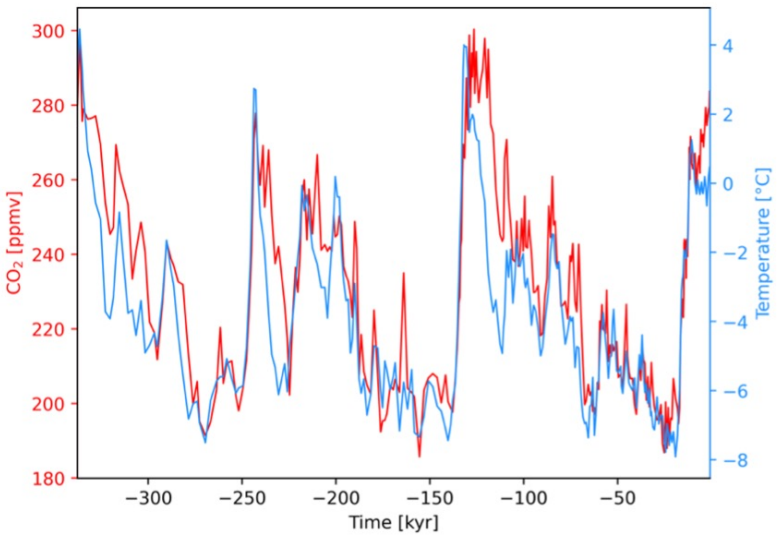

Figure 2.1: *CO_2 (red line) and T (blue line) time histories from Dome Fuji ice Core. T refers to the T anomaly with respect to the present day T.*

2.4.2.2 Methodology

Our goal consists in finding a link between the atmospheric T and CO_2 time-histories from ice cores data. With the term link we mean a set of consecutive-in-time 1-D functions where time is the independent variable, which can be applied to the T time-series to reproduce the observed atmospheric CO_2 record. We use a Bayesian approach, which enable us to measure the uncertainty in the retrieved set of functions. Bayes' theorem defines the posterior probability distribution (PPD) of a model as proportional to its prior probability distribution (or simply prior) multiplied by the likelihood of the model to certain data:

$$P(m \mid I, d) \propto P(m)L(d \mid m, I) \tag{2.3}$$

where $P(m \mid I, d)$ is the PPD, $P(m)$ is the prior (i.e., our knowledge of the set of functions before considering the data), $L(d \mid m, I)$ is the likelihood function, which measures the discrepancies between the observed data and the predictions obtained using a model m, and I represents the hypotheses behind the study. Here, the model m represents the set of functions, and the data is the time derivative of observed (or synthetic) atmospheric CO_2 concentrations, $\frac{dC}{dt}$. The T time-series, that we use to reconstruct the atmospheric $\frac{dC}{dt}$ concentration, is considered known with infinite precision. The PPD applies to the model parameters (i.e., the parameters describing the set of functions) and is conditioned by $\frac{dC}{dt}$ and the a priori information about the parameters themselves [116]. Despite the simple definition given in Eq.2.3, the PPD cannot be analytically solved for non-linear problems. However, it can be numerically estimated using statistical methods, i.e., model-space sampling [160]. The most used approach is the Metropolis-Hasting sampling, where a Markov chain Monte Carlo (McMC) workflow is applied to sample the model-space proportional to the PPD. In this way, the final ensemble of collected models will have a density in the model-space which will be proportional to the PPD (see [161], [109], and Section 2.2 for more details).

Here, we use the trans-dimensional McMC method, also called reversible-jump Markov chain Monte Carlo (rj-McMC), to reduce the degree of subjectiveness in the choice of the set of functions, including the number of functions as an unknown itself. The rj-McMC algorithm [110] has been increasingly used to solve geophysical inverse problems [101], [162], [102], [163], [164], [165]. In its most common implementation, the birth-death algorithm, it allows to estimate a PPD for the number of functions used to describe the data by adding/removing a function from the model and comparing the likelihood of models with different numbers of parameters.

2.4.2.3 Hierarchical Bayes

To test the reliability of the uncertainty estimated on the $\frac{dC}{dt}$ time-series, we extend the rj-McMC method to the Hierarchical Bayes' approach [166], [102]. We thus implement an additional model parameter, ω, to allow the algorithm to vary the noise of the data [167]. For the computation of the model likelihood, the data uncertainty is estimated as follows:

$$\sigma(m) = \sigma_0 10^{\omega} \tag{2.4}$$

where $\sigma(m)$ represents the data error estimate, σ_0 the original uncertainty estimated on the $\frac{dC}{dt}$

time-series, and ω a model parameter that scales the data uncertainty.

2.4.2.4 The forward model

To reconstruct a CO_2 time-series that can be compared to observations from ice core data, we refer to a simple formulation of the geological carbon cycle that link the CO_2 concentration changes to long term variations of surface CO_2 source and sink fluxes where the latter term is assumed to be linearly dependent on T [168], [75], [169], [76], [170] such that:

$$\frac{dC}{dt} = \gamma(t) - \beta(t)T \tag{2.5}$$

where γ is the surface CO_2 input flux, and β modulates the surface CO_2 output flux (βT). The defined model poorly captures the complex short-term CO_2 exchanges among the ocean, atmosphere, and land. However, it offers the key advantage to reduce the number of parameters required to invert for, making it well-suited for testing the algorithm, namely, the primary goal of this work. Additionally, it allows for the exploration of long-term temporal trends in CO_2 exchange between the Earth's surface and its solid components, providing valuable insights.

Since the parameters γ and β vary in time, we consider multiple step functions to map T into atmospheric $\frac{dC}{dt}$ time-series (Figure 2.2). The number of step functions, k, is unknown and therefore treated as a model parameter itself. Thus:

$$m = (k, t, \gamma, \beta, \omega) \tag{2.6}$$

where k is the number of step functions, t is the temporal mid-point of the k-vector, γ and β are the k-vectors and ω is the model parameter described in Equation Eq.2.4. Each ith data-point of the $\frac{dC}{dt}$ time-series is simulated using Eq.2.5, T assumes the value of the ith data point of the T time-series, while γ and β assume a constant value throughout each ti time interval.

2.4.2.5 Implementation of the Markov chain Monte Carlo based on Metropolis' rule

The parameters of the first model of the chains are sampled stochastically from the prior distributions, which we assume to be uniform (e.g., Table I). Then, a candidate model is proposed according to the following recipe. The algorithm perturbs the current model through the application of one randomly selected move among:

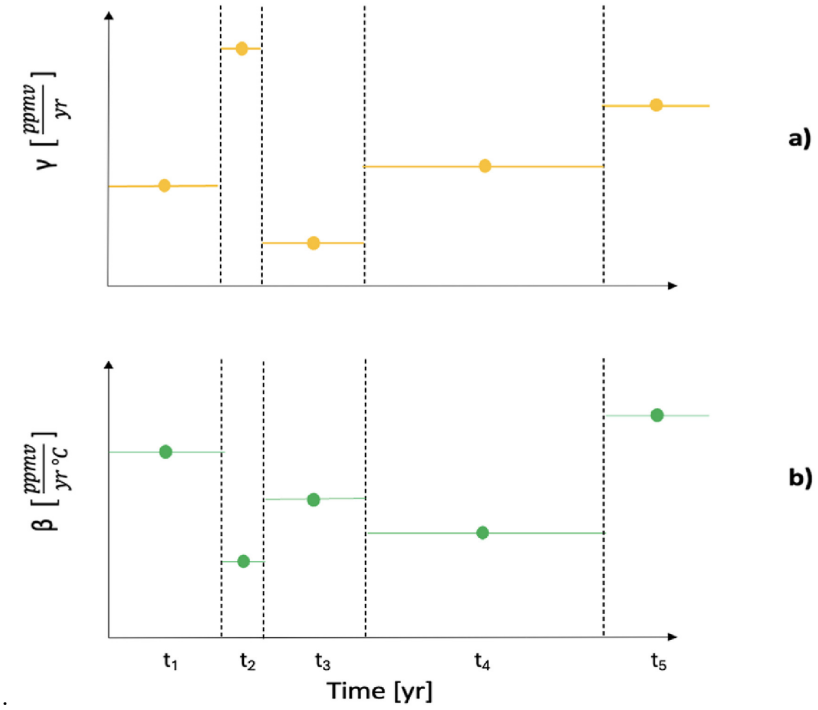

Figure 2.2: *Explanatory sketch depicting the model time series for γ (a) and β (b). γ_i and β_i are constant throughout each ti time interval (e.g., t_1, t_2, t_3, t_4, t_5).*

1. perturb the noise scale factor ω;
2. perturb the time location of a randomly selected nucleus;
3. perturb β of a randomly selected function;
4. perturb γ of a randomly selected function;
5. add/remove a function.

For moves 1-4, the values of the perturbed parameters are selected using the workflow illustrated in Appendix 1 of [102], which guarantees the sampling of the prior distributions, asymptotically, if the data are not informative (i.e., all models have the same likelihood). For move 5, in case of a birth of a new function, i.e., a new function is added to the set, we randomly select the origin-time and two parameters of the new function from the priors. In case of a death of a function, i.e., it is removed from the set of functions, we randomly select one existent function, and we remove it. $\frac{dC}{dt}$ predictions are computed from every candidate model proposed, following Eq. 2.5. Along the workflow, the algorithm selects one of the five moves with an equal probability of 20% to avoid biased or subjective move selection.

Model Parameter	**Min**	**Max**
t [kyrs]	-337.0	0.0
γ $[\frac{ppmv}{yr}]$	0.000	0.045
β $[\frac{ppmv}{yr\,^{\circ}C}]$	0.0007	0.0040
k	1	100
ω	-1.0	3.0

Table I: *Minimum and maximum values for uniform sampling of model parameters used in the real case inversions. k and ω are dimensionless quantities.*

Such predictions are used to compute the likelihood of the candidate model following a standard Gaussian error model, that is:

$$l(d|m,I) = \frac{1}{[2\pi\sigma(m)]^{N/2}} exp^{(-\frac{1}{2}\phi)} \tag{2.7}$$

with $\phi = \sum_i (\frac{d_i - p_i}{\sigma(m)})^2$, where ϕ represents the sum of squares of the residuals weighted for the data uncertainty, $d_i - p_i$ is the discrepancy between the ith data-point and its prediction with model m (so called residual), and N is the number of data-points. $\sigma(m)$ refers to Eq. 2.4. The likelihood of the candidate model is used to accept it or reject it from the sampling. The probability α of a candidate model (m_{cand}) to be accepted is based on Metropolis' rule [114]. If the likelihood of m_{cand} is higher than the likelihood of the current model, m_{curr}, the candidate is always accepted, that is its acceptance probability $\alpha = 1$. If the likelihood of m_{cand} is lower than the that of m_{curr}, the candidate is accepted with probability $\alpha = \frac{L(m_{cand})}{L(m_{curr})}$ [116], [102]. When the candidate model is accepted, m_{cand} becomes m_{curr} and the sampling continues on such model. When m_{cand} is rejected, m_{curr} is kept as the current model and once again stored into the final ensemble of sampled models (i.e. a model with a high likelihood can appear multiple times in the sampled population). Starting from a random point in the model-space, the rj-McMC sampling is likely to initially sample not representative models. Thus, we discard the first half of the sampling as a burn-in phase, and only keep samples that belong to the second half of the chains.

2.4.2.6 Computation time

Tests were performed running independent chains in serial on a single node of a High-Performance Computing cluster, which exploits an Intel OmniPath Cluster architecture and Intel® Xeon Phi^{TM} processors. The inversion of two synthetic tests running 10 chains of 5 x 10^6 models (Sections 2.4.3.1 and 2.4.3.2) is performed in 30 minutes. The inversion of the real case study running 50 chains of 2 x 10^6 models and collecting 1 every 10^4 models to generate the final model ensemble, derive γ and β, and reconstruct $\frac{dC}{dt}$ (Experiment 1, Section 2.4.3.3) is performed in 2 hours. The inversion of the real case study running 20 chains of 1 x 10^6 models, collecting 1 every 10^3 models (Experiment 2, Section 2.4.3.3), and running 50 chains of 3 x 10^6 models, collecting 1 every 10^4 models (Experiment 3, Section 2.4.3.3), are performed in 4 hours. In all tests the first half of each chain models was discarded as burn-in phase.

2.4.3 Results

2.4.3.1 Synthetic test 1

We first test a 340 kyrs long synthetic CO_2 time series based on increasing T from 0 °C to 10 °C. The synthetic CO_2 record is defined through a set of five functions where γ and β are arbitrarily selected (II). The algorithm could uniformly sample k, t, γ and β within fixed ranges where $1 \leq k \leq 100$; $-340 \leq t \leq 0$ [kyrs]; $0 \leq \gamma \leq 0.1$ $[\frac{ppmv}{yr}]$; $0 \leq \beta \leq 0.1$ $[\frac{ppmv}{yr°C}]$. Uncorrelated noise was added during the CO_2 synthetic generation and a constant standard deviation of 1 x $10^{-5}$$[\frac{ppmv}{yr}]$ was associated to the generated CO_2 data. The scale parameter ω was allowed to vary between -1 and 3. The inversion was performed by collecting 1 every 10^4 models to generate the final model ensemble, derive γ and β, and reconstruct $\frac{dC}{dt}$.

Time [kyrs]	$\boldsymbol{\beta[\frac{ppmv}{yr°C}]}$	$\boldsymbol{\gamma[\frac{ppmv}{yr}]}$
-340.0; -212.5	0.001	0.030
-212.5; -150.0	0.050	0.001
-150.0; -102.5	0.001	0.050
-102.5; -50.0	0.050	0.001
-50; 0	0.001	0.030

Table II: *Values of γ and β at different times used for the generation of the synthetic time history of CO_2. Time is reported as range interval.*

As shown in Fig. 2.3, the algorithm successfully reconstructs both the CO_2 (t) through the integration of the reconstructed $\frac{dC}{dt}$, and the $\frac{dC}{dt}$ record itself, marked by abrupt changes when γ and β assume different values (Fig. 2.3a, b). The time histories of γ and β were successfully reproduced within an overall constant error (Fig. 2.3c, d) while the final number of dimensions sampled from the posterior distribution fits the imposed number of functions (Fig. 2.3e).

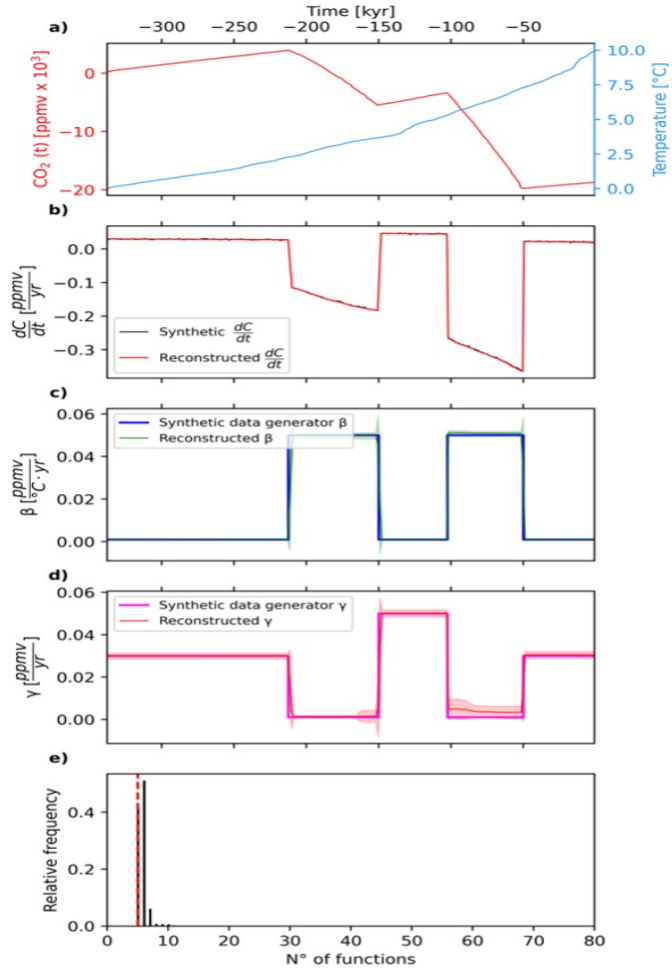

Figure 2.3: *Output from test 1: (a) CO_2 reconstruction obtained through the integration of the reconstructed (red line). The increasing T used for synthetic generation is also shown (dodger blue line). (b) Comparison between the synthetic (black) and reconstructed (red). (c) Time history retrieved from the generated(blue) and reconstructed (green) values of β. (d) Time history retrieved from the generated (magenta) and reconstructed (red) values for γ. (e) Most frequent number of functions sampled for the inversion expressed as model relative frequency.*

2.4.3.2 Synthetic test 2

As a second test, we create a synthetic time series of CO_2 starting from the T histories derived from the Dome Fuji ice core [156] (Fig. 2.1). We generate a non-negative time history of T, subtracting the minimum value of T to all entries to avoid misleading interpretation of the resulting input and

output flux time histories. The synthetic record of CO_2 is based on eight functions with associated, arbitrarily selected, γ and β values (Fig. 2.4a and III). The algorithm could uniformly sample k, t, γ and β within fixed ranges ($1 \leq k \leq 100$, $-340 \leq t \leq 0$ [kyrs]; $0 \leq \gamma \leq 0.1$ $[\frac{ppmv}{yr}]$; $0 \leq \beta \leq 0.1$ $[\frac{ppmv}{yr°C}]$). Uncorrelated noise was added during the CO_2 synthetic generation and constant standard deviation of 1 x 10^{-5} $[\frac{ppmv}{yr}]$ was associated to the time history of CO_2. The scale parameter ω was allowed to vary between -1 and 3. The inversion was performed by collecting 1 every 10^4 models to generate the final model ensemble, derive γ and β, and reconstruct $\frac{dC}{dt}$.

Time [kyrs]	$\boldsymbol{\beta[\frac{ppmv}{yr°C}]}$	$\boldsymbol{\gamma[\frac{ppmv}{yr}]}$
-340.0; -275.0	0.020	0.005
-275.0; -225.0	0.001	0.030
-225.0; -187.5	0.020	0.010
-187.5; -150.0	0.050	0.001
-150.0; -112.5	0.001	0.050
-112.5; -90.0	0.020	0.020
-90.0; -50.0	0.050	0.001
-50; 0	0.001	0.030

Table III: *Values of γ and β at different times used for the generation of the synthetic time history of CO_2. Time is reported as range interval*

As shown in Fig. 2.4, the algorithm successfully reconstructs both the CO_2(t) through the integration of the reconstructed $\frac{dC}{dt}$, and the $\frac{dC}{dt}$ record itself, marked by abrupt changes when γ and β assume different values (Fig. 2.4a, b). The synthetic time histories of γ and β are successfully reproduced within an overall constant error (Fig. 2.4c, d) The final number of functions sampled from the posterior distribution slightly exceeds the number of imposed ones (Fig. 2.4e).

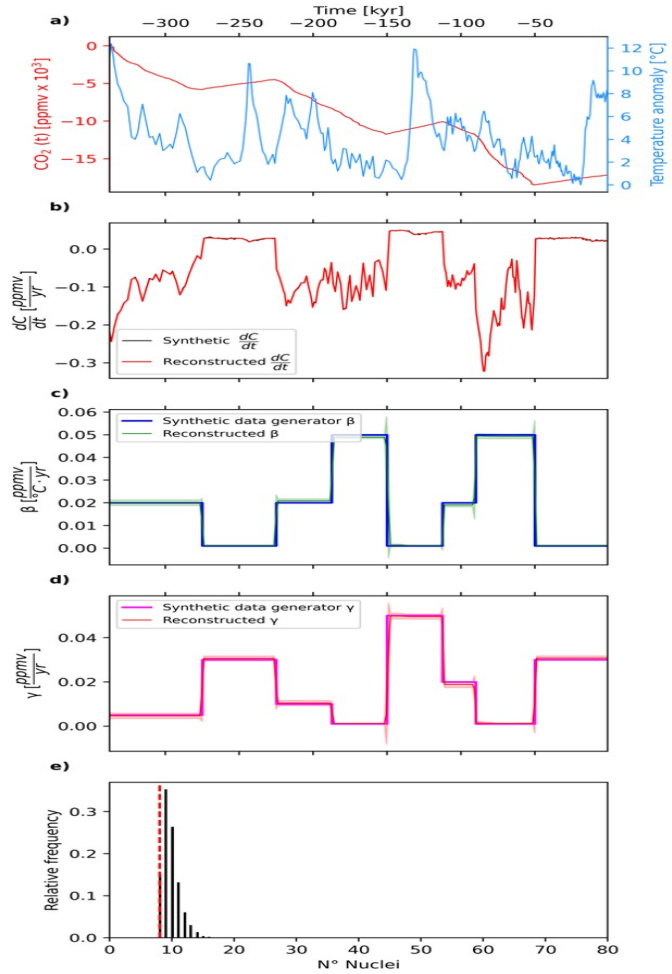

Figure 2.4: *Output from test 2: (a) CO_2 reconstruction obtained through the integration of the reconstructed (red line). (b) Comparison between generated (black line) and reconstructed (red line) CO_2. (c) Time history retrieved from the generated (blue) and reconstructed (green) values of β. (d) Time history retrieved from the generated (magenta) and reconstructed (red) values for γ. (e) Most frequent number of functions sampled for the inversion expressed as model relative frequency*

2.4.3.3 Real case study: Dome Fuji ice core data

As a real case study, we use the same T record of test 2 and the 340 kyrs long atmospheric CO_2 time history measured in air bubbles within the Dome Fuji ice core [140], [156]. We performed three experiments that show how the number, temporal distribution and uncertainty of CO_2 data can affect the inversion results. In the first experiment, $\frac{dC}{dt}$ is computed as central derivatives

and we allow the scale parameter ω to vary. In the second experiment, $\frac{dC}{dt}$ is computed as central derivatives and we fix the scale parameter ω. In the third experiment, $\frac{dC}{dt}$ is computed as a smoothed derivative and we allow the scale parameter ω to vary. Given that we do not have any prior information about γ, β, k, t, and ω, we assign the parameter space arbitrarily and use the same for all experiments (Table I). We choose positive values between minimum and maximum $\frac{dC}{dt}$ as the sampling range for γ. Regarding β, we test different ranges based on the value distribution in time during the inversion. We initially use the same range of γ and progressively reduce it until it scales with β changes. In addition, we bind the parameters γ and β to be non-negative, given that they are associated to carbon sources and sinks, respectively.

Experiment 1: central derivatives and unconstrained ω

In the first real case experiment, $\frac{dC}{dt}$ is computed using a central derivative such that $\frac{dC}{dt}_{(i)} = \frac{CO_{2(i+1)} - CO_{2(i-1)})}{t_{(i+1)} - t_{(i-1)}}$, where i indicates elements along the time series, and we allow ω to vary. We associate a standard deviation of 10^{-5} $[\frac{ppmv}{yr}]$ to the data. The algorithm retrieves large oscillations of $\frac{dC}{dt}$ due to abrupt variations of CO_2 associated to glacial-interglacial cycles (Fig. 2.5a, b). The sampling focused on times of rapid CO_2 changes, namely the deglaciation events, while a limited number of functions are needed during glaciations, implying that parameters β and γ do not vary significantly over these periods (Fig. 2.5c-e). The CO_2 source flux, γ, retrieved within a small uncertainty, is subject to periodic pulses synchronous to deglaciations. The time history of the CO_2 sink flux, βT, is dominated by the temporal variability of T. β, which represents an amplification term for sink fluxes, is associated to a wider standard deviation with respect to that of γ and increases since 270 ka. The integration of the reconstructed $\frac{dC}{dt}$, however, reproduces the original CO_2 trend only for the last and penultimate deglaciations (Fig. 2.5a).

Experiment 2: central derivatives and constrained ω

In the second real case experiment, $\frac{dC}{dt}$ is computed using central derivatives (same as experiment 1), but we impose $\omega = 0$ and associate a standard deviation of 10^{-5} $[\frac{ppmv}{yr}]$ to the data.

Following Eq. 2.5, this implies that the error on the model is only given by the standard deviation associated to $\frac{dC}{dt}$ and the sampling is not affected by ω. The algorithm retrieves all the oscillations of $\frac{dC}{dt}$ (Fig. 2.6a, b) and sampling occurs throughout the entire time series, although major peaks at times of rapid CO_2 changes, implying more significant variations of β and γ, are still observed (Fig. 2.6c-e). The CO_2 source flux, γ, is subject to small oscillations due to small $\frac{dC}{dt}$ variations during glaciations and shows major pulses during the deglaciations. The time history of the CO_2 sink flux, βT, is dominated by the temporal variability of T. Finally, the amplifying parameter β is subject to oscillations corresponding to declining and rising of CO_2, but no clear trends can be recognized. The integration of the reconstructed $\frac{dC}{dt}$ reproduces the original CO_2 time series, including both glacial and interglacial phases (Fig. 2.6a).

Experiment 3: smoothed derivative and unconstrained ω

In the third real case experiment, $\frac{dC}{dt}$ is computed as the slope of the linear regression generated by CO_2 values within a fixed 6-kyrs time interval (i.e., the highest time resolution given the CO_2 data temporal distribution) and we allow the scale parameter ω to vary and associate a standard deviation of 10^{-5} $[\frac{ppmv}{yr}]$ to the data. The algorithm can retrieve oscillations of $\frac{dC}{dt}$ (Fig. 2.7a, b). The sampling occurs throughout the time series, but shows major peaks during deglaciations, implying a significant variation of the parameters β and γ (Fig. 2.7c-e). The CO_2 source flux, γ, is subject to small oscillations during glaciations and larger pulses during deglaciations. The time history of the CO_2 sink flux, βT, is dominated by the temporal variability of T and the amplifying parameter β is subject to oscillations during the glaciations and deglaciations. The integration of the reconstructed $\frac{dC}{dt}$, however, reproduces the original CO_2 trend only for deglaciation events (Fig. 2.7a).

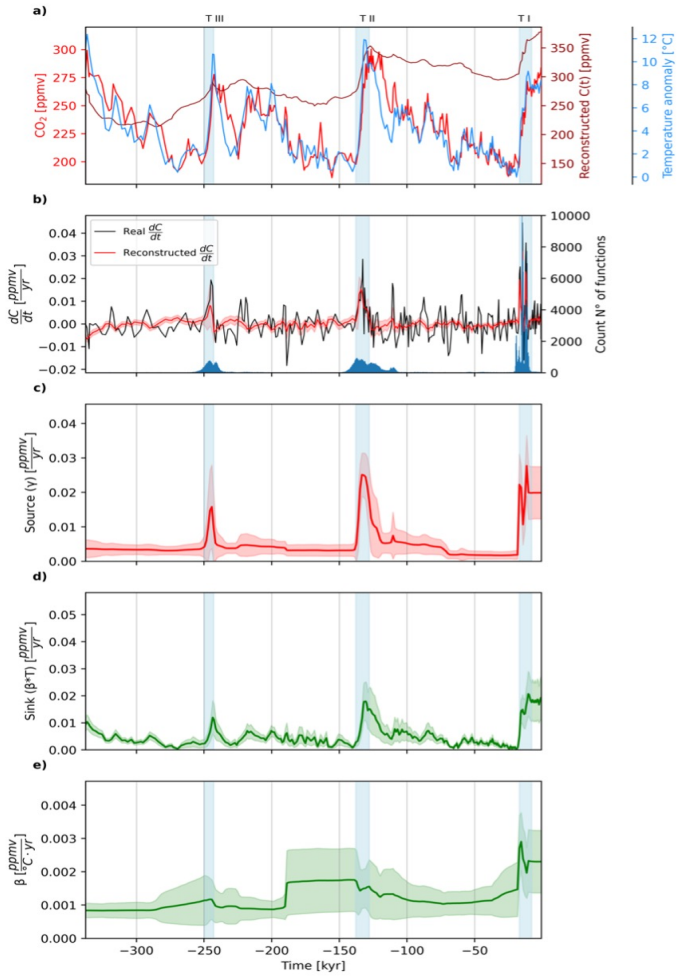

Figure 2.5: *Output from the real case study, experiment 1: (a) Climatic oscillations of CO_2 (red), the integration on the reconstructed $\frac{dC}{dt}$ (dark red) and T (dodger blue) from Fuji Dome ice core. (b) Comparison between real (black) and reconstructed $\frac{dC}{dt}$ (red) with associated standard deviation for synthetic $\frac{dC}{dt}$ (light red). Overlapped, a histogram showing the n° of functions from the inversion. (c) Retrieved time history of source carbon fluxes with associate band error (light red). (d) Retrieved time history of sink carbon fluxes with associated standard deviation (light green). (e) Retrieved time history of β with associated standard deviation (light green). In all panels, light blue shaded bands show main deglaciation events*

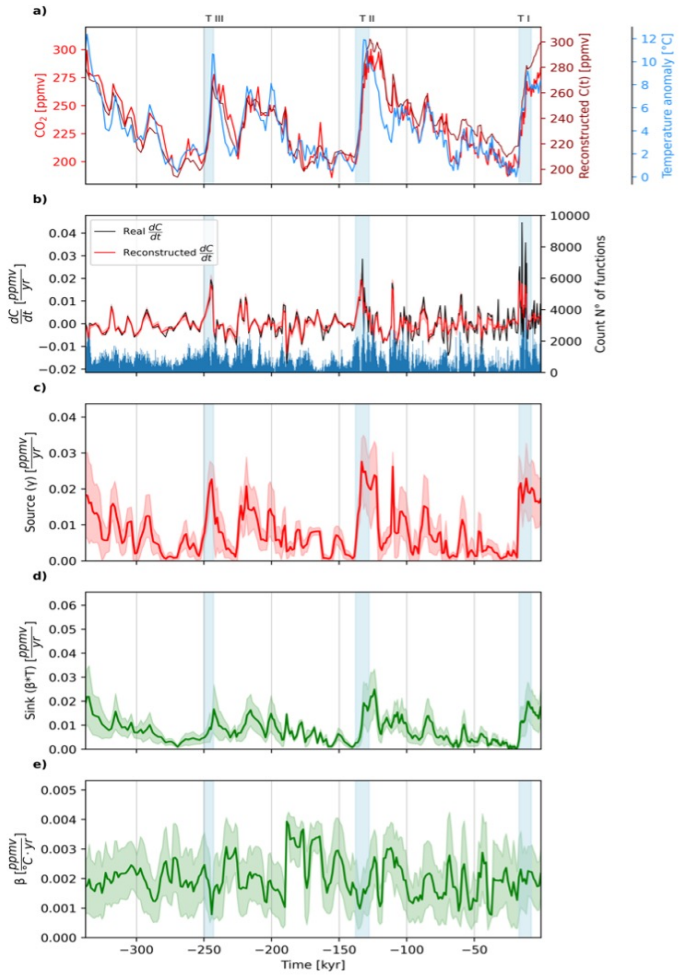

Figure 2.6: *Output from the real case study, experiment 2: (a) Climatic oscillations of CO_2 (red), the integration on the reconstructed $\frac{dC}{dt}$ (dark red) and T (dodger blue) from Fuji Dome ice core. (b) Comparison between real (black) and reconstructed $\frac{dC}{dt}$ (red) with associated standard deviation for synthetic $\frac{dC}{dt}$ (light red). Overlapped, a histogram showing the n° of functions from the inversion. (c) Retrieved time history of source carbon fluxes with associate band error (light red). (d) Retrieved time history of sink carbon fluxes with associated standard deviation (light green). (e) Retrieved time history of β with associated standard deviation (light green). In all panels, light blue shaded bands show main deglaciation events.*

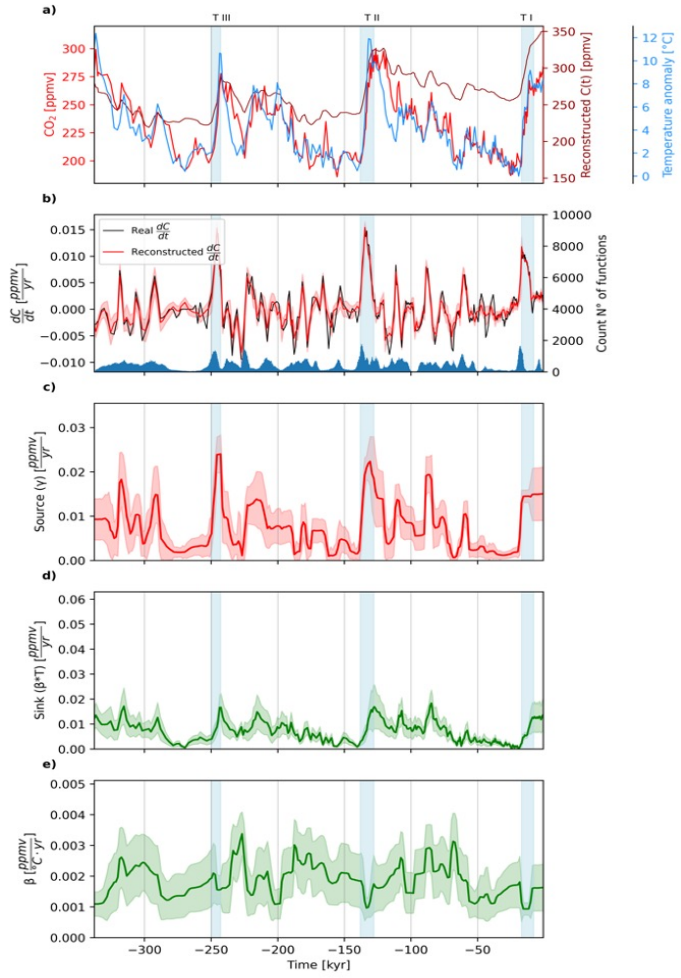

Figure 2.7: *Output from the real case study, experiment 3: (a) Climatic oscillations of CO_2 (red), the integration on the reconstructed $\frac{dC}{dt}$ (dark red) and T (dodger blue) from Fuji Dome ice core. (b) Comparison between real (black) and reconstructed $\frac{dC}{dt}$ (red) with associated standard deviation for synthetic $\frac{dC}{dt}$ (light red). Overlapped, a histogram showing the n°of functions from the inversion. (c) Retrieved time history of source carbon fluxes with associate band error (light red). (d) Retrieved time history of sink carbon fluxes with associated standard deviation (light green). (e) Retrieved time history of β with associated standard deviation (light green). In all panels, light blue shaded bands show main deglaciation events.*

2.4.4 Discussion

Rj-McMC algorithms find their primary application in seismological studies [171], [165], [172], but our results demonstrate that this technique can be successfully used to invert paleoclimate time series. Previous studies used rj-McMC algorithms for paleoclimatic reconstructions (e.g., [162], [173]), but their analysis encompasses the last millennium, and their forward model does not include a T-CO_2 dependence. [174] prove an interesting application of Bayesian inversion of a CO_2 time series at Cretaceous-Paleogene Boundary (K-Pg). However, they perform the inversion using a non-trans-dimensional Markov chain Monte Carlo (McMC) algorithm and do not investigate the temporal variability of model parameters. Here, we go beyond historical timescales, coupling available measurements of paleo-atmospheric CO_2 concentrations from Dome Fuji ice core [140], estimates of the paleo-T from δD data [156], and a simple formulation of the geological carbon cycle (Eq. 2.5) [76], [170], [175] investigating the temporal variability of model parameters γ and β. In this regard, although the model proposed in Eq. 2.5 could benefit from incorporating additional parameters to more accurately represent the short-term carbon cycling between surface reservoirs (e.g., atmosphere, ocean, land), the primary objective of this work is that of exploring new approaches to inverse modeling of paleo-climatic time series. Then, while making this task easier by reducing the number of inverted parameters, the formulation in Eq. 2.5 still provides valuable insights into CO_2 exchanges between the surface and the Solid Earth reservoirs and marks a turning point in the strategies for inverting paleo-climatic timeseries. Indeed, differently from predictions obtained via box, intermediate complexity, or global circulation forward climate modeling, the obtained data-inferred parametrization of atmospheric CO_2 source (γ) and sink (βT) fluxes (Fig. 2.5-2.7) do not rely on poorly constrained model parameters. This facilitates unbiased interpretations of the variability of atmospheric CO_2 concentrations and assessments of their underlying drivers, a primary goal for Earth, environmental, and climate scientists.

The fit between real and reconstructed $C(t)$ and $\frac{dC}{dt}$ (Fig. 2.5-2.7a, b), the time histories of atmospheric source/sink fluxes (Fig. 2.5-2.7c, d) and the amplificatory sink parameter β (Fig. 2.5-2.7e) retrieved in the three experiments show that different assumptions lead to different solutions of the inverse problem (e.g., [166]). In experiment 1, we vary the scale factor ω to limit the effect of strong assumptions on the assigned $\frac{dC}{dt}$ uncertainties [167], leading to a reduced model complexity, i.e., the number of functions. The stability of γ and β during glacial phases (Fig. 2.5c, e) depends

on the high values retrieved for the parameter ω (Fig. 2.8a, b) and indicates that the assigned standard deviation of 10^{-5} $[\frac{ppmv}{yr}]$ is not representative for $\frac{dC}{dt}$. In experiment 2, we impose $\omega = 0$, which leads to higher temporal variability of γ, βT and β, as well as a good fit between real and reconstructed $C(t)$ and $\frac{dC}{dt}$ (Fig. 2.6a-e). Since ω cannot vary, the algorithm searches for higher precision $\frac{dC}{dt}$ values, increasing the model complexity but overfitting the data. In experiment 3, the use of a different $\frac{dC}{dt}$ time history leads to lower ω and higher model complexity (Fig. 2.8c, d), a higher variability of γ, βT and β (Fig. 2.7c-e), and a better fit between the real and reconstructed $C(t)$ and γ, βT and β (Fig. 2.7a, b) compared to experiment 1.

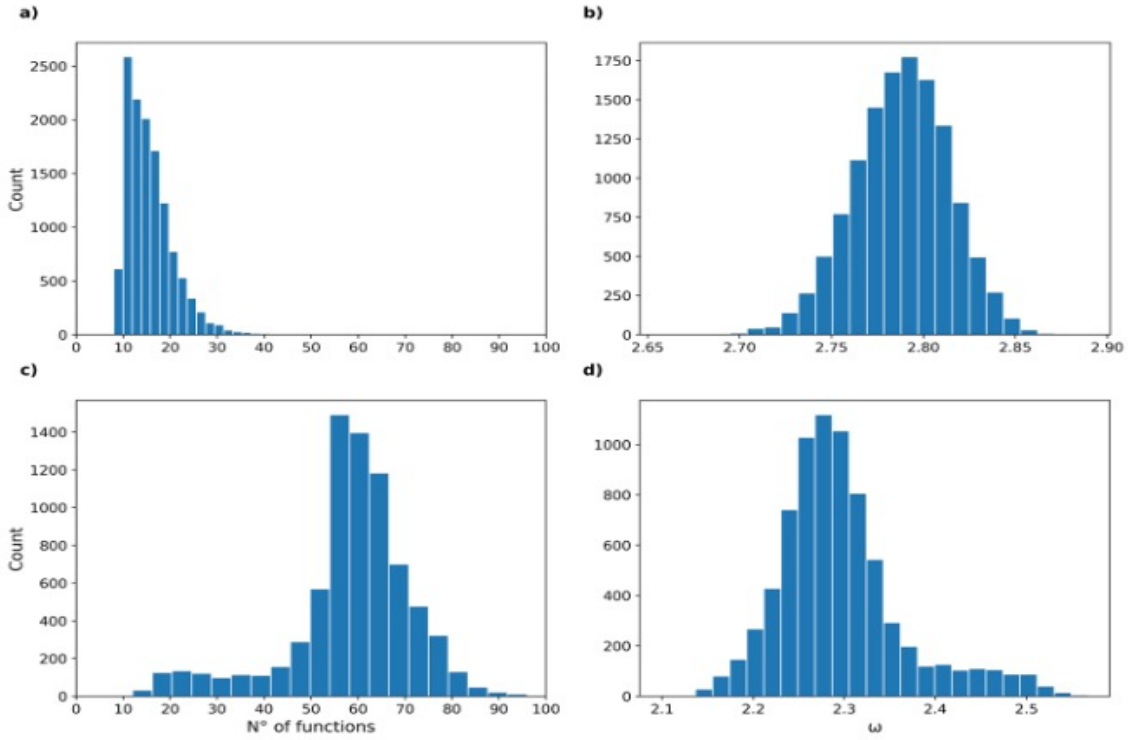

Figure 2.8: *Distribution of the n° of functions (a, c) and ω (b, d) retrieved in experiment 1 and 3, respectively.*

In this context, the use of Hierarchical Bayes within a rj-McMC algorithm, as applied in Experiment 1 and 3, provides a more robust approach to generalizing forward model parametrization, effectively mitigating the overfitting challenges commonly encountered with Deep Learning algo-

rithms [176],[177]. Additionally, rj-McMC algorithms do not require the fine-tuning of hyperparameters, thereby reducing the potential for subjective biases in the inversion process [178], [179]. Moreover, depending on the timescale of interest, the quantity, completeness, and quality of paleoclimatic data used for surface paleo-CO_2 reconstructions may be insufficient to effectively train Machine Learning models, including the most recent Physics Informed Network [180], [181]. In all three experiments, we recognize a robust pattern regarding γ, which shows marked peaks during deglaciations. The cross correlations between γ-βT and γ-T for the three experiments (Fig. 2.9a-f) further indicate consistent peaks of T and βT 2.5 kyrs after pulses of γ. The increasing β trend retrieved in experiment 1 is not confirmed by experiments 2 and 3, but the choice of ω = 0 in experiment 2 is subjective and experiment 3 inverts a strongly smoothed $\frac{dC}{dy}$.

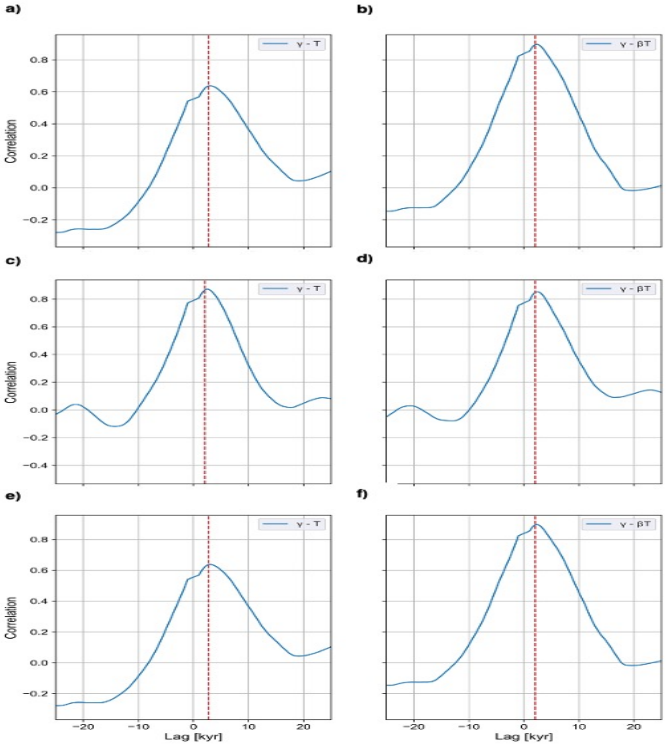

Figure 2.9: *Cross-correlations between CO_2 source flux ω and T (a, c, e) and between CO_2 source flux γ and βT (b, d, f) in experiment 1, 2 and 3, respectively. The maximum-lag correlation is about 2.5 kyrs in all experiments (dashed, red line).*

Within the context of glacial-interglacial oscillations, the precessional, obliquity, and eccentricity

orbital cycles combine to modulate solar irradiation with characteristic frequencies of 20, 40 and 100 kyrs, respectively [127]. Although Milankovitch orbital parameters lead the Pleistocene glacial-interglacial variabilities [182], [183], [184], the role of CO_2 variations due to internal climate dynamics cannot be neglected [185],[186], [187]. Our results indicate lacking variations in the atmospheric CO_2 source flux γ and the amplificatory factor of the CO_2 sink flux β during glacials (Fig. 2.5c, e), suggesting that orbitally pacing T changes can explain the observed reductions of atmospheric CO_2 concentrations [127], [130]. Conversely, multiple functions during deglaciations suggest that rising T alone cannot explain increasing atmospheric CO_2 concentrations, which are thus driven by significant variations of atmospheric CO_2 source and/or sink fluxes (in their β term) related to climate-forcing mechanisms internal to the Earth system. In particular, periodic pulses of γ at the onset of deglaciations (Fig. 2.5c), implying sharp increases of CO_2 source fluxes and abrupt falls to background values before the end of interglacials, drive the increase of atmospheric CO_2 concentrations. The observed behavior of γ, therefore, is similar to that of a capacitor that rapidly releases large amounts of CO_2 to the surface during deglaciations and slowly recharges during glacial periods. The peak of the CO_2 source flux during deglaciations, in addition, anticipates that of T by approximately 2.5 kyrs (Fig. 2.9a), in turn suggesting that CO_2 source flux pulses drive the increase in T and atmospheric CO_2 concentrations during deglaciations. Estimated surface CO_2 sink fluxes (Fig. 2.5d) are also characterized by short term variability, with prominent peaks dictated by the T increases during deglaciations that lag pulses of surface CO_2 source fluxes (Fig. 2.9b). To explain the variability of atmospheric CO_2 and the low-frequency amplification of glacial-interglacial cycles since the Mid-Pleistocene Transition (MPT) [188], [185], [189], [190], research efforts have focused on climate system components that respond to the orbital forcing such as the growth/melting of continental ice sheets and associated albedo effects and isostatic adjustment of continental lands, the carbonate system of the ocean, or ocean-atmosphere dynamics and interactions [191], [192], [193], [194]. We further note that enhanced volcanic outgassing following unloading of subaerial magmatic provinces due to melting of continental ice-sheets [42], [21], [195], [196], [48] would also be consistent with our retrieved surface CO_2 source and sink fluxes. Reduced decompression partial rock melting during glaciation due to increasing ice loads atop of active magmatic provinces enables the storage of CO_2 within magmatic plumbing systems, which is then abruptly emitted at the beginning of the deglaciation when shrinking ice-loads enhance global subaerial volcanism [197]. The time response of magmatic chambers to depressurization can vary due to different viscoelastic

magmatic properties from decadal [198], [199] to millennial [200] time scales. In our analysis, the peak of the CO_2 source flux, γ, during deglaciations occurs 4.5 kyrs after the onset of orbitally-driven T increase (Fig. 2.5a, c), consistent with the estimated response time of silicic magma chambers to surface load variations [200]. Then, the shift toward warmer and more humid climate during deglaciation enhances weathering of silicate minerals, thereby fostering the sequestration of atmospheric CO_2 [201], [202]. The fast return to background, constant atmospheric CO_2 source fluxes during interglacials and throughout glaciations (Fig. 2.5c) allows for progressively decreasing atmospheric CO_2 sink fluxes (Fig. 2.5d), explaining faster early-glacial than late-glacial atmospheric CO_2 concentrations reductions (Fig. 2.5a). A conclusive association to the underlying climate-driving mechanisms is beyond the scope and possibilities of this study. However, the surface source and sink CO_2 fluxes retrieved here, as well as future applications of the algorithm presented and integrated with more comprehensive and advanced formulations of the geological carbon cycle will provide further significant insights into the climate history and inform projections of its future trajectories.

2.4.5 Conclusion

We provide a robust Bayesian framework to infer time histories of atmospheric CO_2 source (γ) and sink (βT) fluxes from paleo-climate time series based on a simple formulation of the geological carbon cycle, marking a significant shift in the strategies for inverting paleo-climatic time series. Tests conducted on both synthetic and real data demonstrate the effectiveness of the methodology in interpreting the variability of atmospheric CO_2 concentrations during glacial-interglacial cycles. We show how prior assumptions regarding the parametrization can affect the inversion results by performing three different experiments on the same CO_2 dataset. Retrieved atmospheric CO_2 source and sink fluxes (Fig. 2.5) throughout the last three glacial-interglacial cycles, however, show robust periodic and abrupt changes that lag by a few thousands of years, suggesting the activation of and interactions between climate-driving mechanisms internal to the Earth system especially during climate warming periods. Although, the unambiguous identification of these mechanisms is still beyond possibilities, we recognize that these robust trends are consistent with the deglacial triggering of subaerial volcanism that enhances atmospheric CO_2 input fluxes during deglaciation, thereby accelerating warming trends and, in turn, increasing atmospheric CO_2 output fluxes during interglacial and early glacials. We speculate that such feedbacks may explain the

asymmetry of recent glacial-interglacial cycles, involving faster warming than cooling trends [21], [48]. Future applications of the technique presented and formulations of Eq. 2.5 that include model parameters more representative of the short-term CO_2 exchanges (e.g., atmosphere, ocean and land) can lead to further advances in this direction. However, it must be noted that a high number of model parameters may be critical in terms of computational and time resources required to reach the convergence of parameter estimation. Finally, the method can be flexibly adjusted to longer paleoclimate time series to invert on paleoclimate proxies. We warrant future use of this technique with available longer paleo-climate time series to further assess the drivers of past climate variability and improve inferences on future long term climatic response to ongoing anthropogenic forcings.

2.4.6 Aknowledgments

This work was supported by Fondazione Cariplo and Fondazione CDP (Grant n° $2022 - 1546_0 01$) and by the Italian Ministry of Education, MUR (Project Dipartimenti di Eccellenza, TECLA, Department of Earth and Environmental Sciences, University of Milano-Bicocca). The HPC cluster provided by Cineca was used to test and apply the algorithm.

2.4.7 Data availability

CO_2 and T data come from the contribution of Kawamura et al., 2003 and Uemura et al., 2018, respectively. The CO_2 time-series is available a `https://www.ncei.noaa.gov/metadata/geoportal/rest/metadata/item/noaa-icecore-6077/html`, while the original T time-series at `https://www.ncei.noaa.gov/access/paleo-search/study/23371`.

2.4.8 Code availability statement

The code used, written in Fortran77 and run on a HPC cluster, is available on github at `https://github.com/LucaCastrogiovanni/rj-split-ice-cores.git`. Nicola Piana Agostinetti wrote the code and Luca Castrogiovanni adapted it to invert on paleo-CO_2 data.

Chapter 3

Carbon fluxes throughout the Late Pleistocene

Glacial-interglacial cycles represent one of the most intriguing conundrum of recent climate history. Fast deglaciations involving CO_2 and T increases leave place to slow glacial inceptions through progressive T decrease and atmospheric CO_2 removal, generating the so-called "sawtooth trend". Originally explained as the result of full orbital forcings, over recent decades increasing works have demonstrated the active role of internal Earth's system mechanisms, involving the most diverse theories and processes. During deglaciations, Pleistocene world is liable to higher ice melting which facilitates the CO_2 release from the Southern Ocean, permafrost thawing on land, and subaerial volcanic eruptions due to unloading of previously ice covered magmatic systems. On the other hand, early glacial phases involve the drawdown of CO_2 due to fast terrestrial weathering and photosynthetic processes on land while higher nutrient supply to the ocean during late glacials further enhance the CO_2 and T drawdown. This led to the question if fast deglaciations are the result of glacial termination or interruption. After providing in Section 2.4 a comprehensive description and real case application of the developed algorithm, I present here my second study, currently under peer-review for *Nature Communications*, which aims to provide a better understanding of the late Pleistocene glacial-interglacial cycles in terms of carbon source and sink fluxes. The work, conducted through the inversion of the paleo-atmospheric $\frac{dC}{dt}$ record retrieved in the Antarctic ice core of Dome C, sheds light on the carbon flux evolution of the last ˜800 kyrs.

Reconstructed late-Pleistocene CO_2 fluxes reveal a shift in carbon cycling since the Mid-Brunhes transition

Castrogiovanni L.[1, 2], Sternai P.[1,3], Pasquero C. [1], Piana Agostinetti N.[1], Longman J. [2]

[1]Department of Earth and Environmental Sciences, University of Milano-Bicocca, Italy.

[2]Department of Geography and Environmental Science, Northumbria University, UK.

[3]GFZ, German Research Centre for Geosciences, Potsdam, Germany.

Status: Under peer-review for *Nature Communications*

Abstract

Ice cores provide constraints on past carbon cycling and associated atmospheric CO_2 and mean surface temperature variations [136], [159], revealing systematic shifts between glacial and interglacial climate states [9], [142]. However, poor quantification of surface source and sink CO_2 fluxes hinders understanding of the drivers and feedbacks behind such climate variability. Correlated atmospheric CO_2 and temperature variations over the past 800 kyr are largely due to orbital forcing, but the intensification of glacial-interglacial cycles since 430 ka, following the so-called Mid-Brunhes Transition (MBT) [67], cannot be explained by orbital parameters alone [203]. This suggests the activation of interacting mechanisms within the Earth system, the nature of which remains debated. We apply a new Bayesian inversion algorithm [122] to the Dome C (Antarctica) CO_2 and temperature record [9], [142] to generate unprecedented reconstructions of surface CO_2 source and sink fluxes. Results reveal systematic pulses of CO_2 source fluxes during glacial maxima and deglaciations, preceding peaks in CO_2 sink fluxes, with all pulses first appearing post-MBT. Wavelet coherence and cross-correlation analyses suggest that post-MBT climate variability was amplified by feedbacks linking sea-level change, ice-sheet dynamics, and volcanic CO_2 emissions [21], [28]. Our findings underscore the influence of the solid Earth on late-Pleistocene carbon cycling and climate and offer critical constraints for models of past and future climates.

3.1 Introduction

The Dome C Antarctic ice core provides the most direct and continuous record of past atmospheric CO_2 concentrations and temperature (T) variations associated with glacial-interglacial cycles over the past 800 thousand years (kyr) [9], [142], [8]. Although it is widely accepted that orbital forcings and associated feedbacks involving ice, ocean, atmosphere, and solid Earth dynamics drive the glacial-interglacial climate variability [21], [79], [57], [204], disentangling their relative contributions remains a major scientific challenge. One particularly puzzling feature in the paleoclimate record is the intensification of glacial-interglacial cycles since 430 thousand years ago (ka), marked by longer glaciations and more abrupt, higher-amplitude deglaciations compared to earlier periods (Fig.3.1a) [9], [142], [79]. This shift, commonly referred to as the Mid-Brunhes Event [205] or Transition [67] (MBT), does not find a straightforward explanation in the orbital variability and is associated with pronounced imbalances in the Earth system documented by multiple archives [203]. Benthic foraminiferal $\delta^{18}O$ in marine sediments indicate increased ice sheet loss and sea-level rise since Termination (i.e., the transition from a glacial to an interglacial phase) V (Fig.3.1b) [79], [206]. On land, loess-paleosol sequences from monsoon-dominated regions in East Asia reflect major shifts in atmospheric circulation [207]. Emerging evidence also suggests that the post-MBT climate reorganization, particularly since Marine Isotope Stage (MIS) 11, contributed to faunal turnover, accelerated mammalian diversification, and facilitated the evolutionary divergence of hominins into Neanderthals, Denisovans, and Homo sapiens in Africa [208], [209]. A multitude of mechanisms have been proposed for the MBT shift, including orbital forcing [67], buildup and collapse of the Antarctic ice-sheet [210], the shift in the Southern Hemisphere westerlies position [211], and the strengthening of the Asian monsoon system [67], [212]. However, a unifying explanation for the observed variability of CO_2 and T prior and after the MBT remains elusive. A key limitation lies in our incomplete understanding of how changes in atmospheric CO_2 and T relate to fluxes of CO_2 among Earth's reservoirs, due to a lack of robust quantitative constraints on these fluxes. Reliably quantifying such CO_2 fluxes is essential for assessing the mechanisms and feedbacks behind the MBT and, more generally, the variability of CO_2 and T throughout glacial-interglacial cycles. Further, quantification of fluxes may aid in improving projections of future climate change, particularly in light of the profound impact of human activities on the global carbon cycle. Approaches investigating the drivers of CO_2 and T changes throughout the late-Pleistocene include forward modelling

with Earth Models of Intermediate Complexity [67], box models [213], and more recent machine learning simulations [214]. However, predictions of CO_2 budgets and fluxes from forward modeling of paleoclimate proxies rely on poorly constrained parameters [215]. Regression-based models that invert data from climatic archives can estimate short-term (centennial-scale) CO_2 fluxes [97], but are ill-suited to capture the non-linear dynamics driving longer-term climate variability across multiple glacial-interglacial cycles. Recently, however, a robust algorithm operating in a Bayesian framework was developed to infer paleo surface CO_2 source and sink fluxes by linking T and atmospheric CO_2 concentration time series [122]. The technique was tested on data from the Dome Fuji ice core [140], [156], but its limited temporal coverage prevented a comprehensive assessment of the drivers of climate changes over the late Pleistocene. Here, we apply this technique (Methods) to CO_2 data from the Dome C ice core [142]4 to generate the currently longest and most reliable reconstruction of atmospheric CO_2 input and output fluxes for the late Pleistocene.

3.2 A marked shift in carbon cycling since MIS 10

To reconstruct the CO_2 fluxes, we link temporal changes of atmospheric CO_2, $\frac{dC}{dt}$, observed in the Dome C ice core [142] to global mean atmospheric T variations from the same ice core [9],[216], using the simplest formulation of the geological carbon cycle [175] as a first-order approximation:

$$\frac{dC}{dt} = \gamma - \beta T \tag{3.1}$$

where γ and β are unknown parameters representing the CO_2 source flux and the amplification term of the temperature dependent CO_2 sink flux, respectively. Eq.3.1 provides an effective framework to model the temporal evolution of atmospheric CO_2, with γ and βT encapsulating the ensemble of mechanisms contributing to CO_2 source and sink fluxes, respectively. Here, we assume that the strengthening of atmospheric processes (e.g., enhanced rainfall) induced by T increases would promote fast weathering responses, leading to a net, short-time temporal carbon decrease [175], [201], [202]. The stability (or variability) of γ and β reflects the degree of coupling (or decoupling) between $\frac{dC}{dt}$ and T. Despite its simplified representation of the geological carbon cycle, Eq.3.1 offers the crucial advantage of efficiently capturing long-term ($> 10^4$ ka) CO_2 variations, thus considering the ocean, land and atmosphere as a unique carbon reservoir at the Earth's

surface [23], [217]. Furthermore, its minimal parametrization enables efficient and reliable reconstruction of surface CO_2 flux histories (Methods). Results show a distinct shift in the patterns of γ and βT, transitioning from minimal variability before MIS 10 (i.e., 350 ka) to periodic pulses thereafter (Fig.3.1c, d). This behavior implies that prior to MIS 10, surface CO_2 flux changes were primarily and linearly driven by T variations. Afterwards, the decoupling of $\frac{dC}{dt}$ from T indicates the emergence of additional processes involving changes of surface CO_2 fluxes that are not directly mediated by T. Systematic pulses of the source term γ occur just before the onset of deglaciations and return to pre-deglaciation levels by the end of the interglacials during MIS 9, 7, 5, and 1 (Fig.3.1c). The sink term βT follows a similar pattern, peaking during the interglacials (Fig.3.1d). These findings are consistent with results from the Dome Fuji ice core [122], indicating that reconstructed patterns of CO_2 flux changes are not unique to the Dome C record (see dashed line in Fig.3.1c, d). Lead-Lag relationships between γ, βT and T were also investigated to quantitively assess lagging responses to post-MBT systematic pulses of CO_2 fluxes (Fig.3.12 in Methods). Peaks of γ anticipate peaks of βT and T by ˜3 kyrs and 7 kyrs, respectively. This suggests that end-glacial (i.e., Glacial Maxima) and deglacial source CO_2 pulses trigger negative feedbacks, which enhance sink CO_2 fluxes and stabilize climate, with cumulative timescales in the order of 100 – 101 kyrs. It is noteworthy that inversions constrained by North Atlantic [218] and tropical [219] T time series (Figs.3.10, 3.11 in Methods) confirm the shift in the carbon cycle around the MBT, although γ and βT pulses clearly arising since MIS 9 and MIS 7, respectively. While delayed γ and βT peaks in the tropics underscore the potential of using local T time series to further investigate regional paleo-climate dynamics, since our goal is to reconstruct global carbon fluxes, we focus here on inversions using global T time series [216], leaving the analysis of local T effects to future studies. We use the reconstructed histories of surface CO_2 source and sink fluxes (Fig.3.1c, d) to investigate possible mechanisms driving the glacial-interglacial climate variability and the shift in carbon cycling since MIS 10. Increased Antarctic dust accumulation rates during glacial periods [220] (Fig.3.1e) suggest intensified atmospheric circulation and enhanced global CO_2 sink via iron fertilization of the Southern Ocean [38]. However, the intensification of dust transport since MIS 12 is more pronounced during late glacial periods, which is difficult to reconcile with enhanced CO_2 source and sink fluxes during late glaciations and deglaciations since MIS 10. The thermal bipolar seesaw – referring to the difference between Greenland and Antarctic temperatures – is associated with shifts in hemispheric heat transport via the Atlantic Meridional Overturning

Circulation (AMOC) and acts on shorter timescales and smaller magnitudes during glacial periods [221]. Climate simulations attempting to reproduce post-MBT interglacial conditions by assuming a reduction in northward AMOC heat transport have been unable to capture the full magnitude of post-MBT interglacial warmth [222]. Moreover, the likely invariance of this mechanism over the past 800 ka fails to explain the observed periodic shifts in CO_2 fluxes since MIS 10 [223]. Fast retreat of the Western Antarctic Ice Sheet (WAIS) has been proposed as a feedback mechanism, interacting with the thermal bipolar seesaw to cause changes in glacial-interglacial T and CO_2 levels since the MBT [210]. However, the most significant WAIS retreat occurred prior to the MBT, during MIS 13 and MIS 15 [206], [210], which is considerably earlier than the reconstructed shifts in global CO_2 fluxes since MIS 10. The global reorganization of water masses during Termination V due to insolation feedbacks [67], involving stronger southward penetration of the North Atlantic Deep Water (NADW), led to higher CO_2 release from the Southern Ocean during post-MBT interglacials [203]. This is in agreement with persisting coupling between $\frac{dC}{dt}$ and T during MIS 11 (Fig.3.1). However, the subsequent decoupling between $\frac{dC}{dt}$ and T retrieved in our analysis (Fig.3.1c, d) suggests further processes affecting post-MBT deglaciations and interglacials. The increased abundance of the ostracod *Acetabulastoma arcticum*(Fig.3.1f), a sea-ice dwelling species that serves as a proxy for Arctic sea-ice cover and surface-ocean productivity [224], indicates more stable Northern Hemisphere ice caps shortly after the MBT. This pattern is consistent with the onset of longer and more sustained glacial periods and is likely associated with the onset of the "Arctic amplification" [224], i.e., anomalously strong T response to relatively minor CO_2 variations in the Arctic region. The close synchronicity between the onset of the Arctic amplification and the recognized shifts in carbon cycling (Fig.3.1c, d) calls for further investigations of possible causative links. To this end, we constrain common periodicities by wavelet coherence transform analysis [225] applied to the time series of *Acetabulastoma arcticum* abundance and γ as the leading term in the reconstructed surface CO_2 fluxes. A shared periodicity between these records (Fig.3.2a, b) emerges after MIS 11. While the shared 100 ka periodicity between these datasets highlights a clear orbital pacing of post-MBT cycles, its earlier emergence in γ records (˜400 ka) compared to the *Acetabulastoma arcticum* record (˜300 ka) suggests that Arctic amplification is a downstream response to post-MBT CO_2 flux changes, likely mediated by evolving Arctic sea-ice dynamics.

3.3 Volcanic emissions conditioning surface CO_2 source fluxes?

Recent studies have documented a peak in explosive volcanic activity along the Pacific Ring of Fire during the transition from glacial MIS 10 to interglacial MIS 9 (Ref.[44]) and steadily increasing tephra deposition since MIS 10 (Ref.[226]). This is likely representative of a broader rise in volcanic activity the timing of which is consistent with that of the decoupling between $\frac{dC}{dt}$ and T retrieved in our analysis (Fig.3.1c, d), suggesting a possible link between ice-sheet dynamics and volcanism. Feedbacks between climate changes and volcanic activity during Pleistocene glacial-interglacial cycles have been extensively debated [42], [227], [228], [229]. Both field observations and modeling studies suggest that surface mass redistribution driven by sea-level fluctuations and the advance/retreat of continental ice sheets modulates magma production and transport in both submarine and subaerial volcanic provinces [197],[230]. Specifically, the growth of ice sheets and associated sea level fall facilitate submarine volcanism along Mid-Oceanic Ridges (MORs) [28], while ice-cap reduction on land enhances subaerial volcanism from magmatic terrains subject to deglaciation [21]. If the observed increase in tephra deposition since MIS 9 (Refs. [44], [226], [43] reflects a broader intensification of global volcanism beyond explosive events, the concurrent rise in γ – representing reconstructed surface CO_2 source fluxes - during post-MBT glacial maxima supports the hypothesis of enhanced mantle decompression melting and magmatic CO_2 emissions from MORs during low sea level stands. The sea-level minimum at the end of MIS 12 represents the most pronounced drop of the past 800 kyrs (Ref.[206], Fig.3.1b), suggesting a possible role of MORs in driving the observed shift in CO_2 fluxes since the MBT. One possible scenario involves intensified mantle decompression melting beneath MORs during the extreme sea-level lowstand of MIS 12 (Fig.3.3a), with associated CO_2 emissions delayed by the abrupt sea-level rise during Termination V (Fig.3.3b) and instead occurring during the subsequent sea-level fall at MIS 10 (Fig.3.3c). However, while models indicate that sea-level drops $\geq$ 100m can enhance MOR magmatism [231], a full glacial-interglacial cycle delay in associated CO_2 release remains contentious [232]. An alternative explanation considers the role of high sea levels during longer, higher-amplitude interglacials since MIS 11 in promoting faulting at MORs [233],[234], which may temporarily suppress decompression melting [231] (Fig.3.3d, e). Such faulting would then facilitate the rise of magmas generated by enhanced partial decompression mantle melting during sea level low-stands since MIS 10 [235], [236], thereby enabling significant magmatic CO_2 emissions to surface reservoirs (Fig.3.3f), as sup-

ported by our reconstructed CO_2 flux time series (Fig.3.1c, d). Additionally, emerging evidence highlights that CO_2 emissions from subaerial volcanic systems in formerly glaciated regions are also modulated by the glacial history, with the deglacial removal of ice caps and eroded rocks fostering both the magma production and its transfer through the crust or lithosphere [197], [196]. Thus, it is plausible that post-MBT pulses in surface CO_2 source fluxes also reflect intensified subaerial volcanic emissions during late glacial stages, when the growth rate of continental ice sheets slows, and across terminations.

We provide a novel approach to investigate paleoclimate trends and present reconstructions of the surface CO_2 source and sink fluxes spanning the last 800 kyrs. A robust feature emerging from these unprecedented time series is a fundamental shift in the dynamics of the carbon cycle across the MBT: prior to the MBT, atmospheric CO_2 variability was primarily governed by T changes as imposed by the orbital forcing, whereas post-MBT glacial-interglacial cycles exhibit a stronger influence from internal Earth system feedbacks. Based on the relative timing and characteristic timescales of most plausible underlying processes, we propose that post-MBT feedbacks are largely driven by sea-level fluctuations and the growth and retreat of continental ice sheets, which modulate volcanic CO_2 emissions. This interpretation suggests that volcanic degassing has played a central role in amplifying the magnitude and asymmetry of climate oscillations during the late Pleistocene glacial-interglacial cycles, as previously proposed by independent studies [21], [48]. If correct, this finding underscores the urgency of curbing anthropogenic CO_2 emissions, which exceed natural volcanic outputs by orders of magnitude [187], to preserve the integrity of Earth's natural climate variability. Irrespective of the specific mechanisms involved, the surface CO_2 flux reconstructions presented here offer an unprecedented perspective on long-term carbon cycle dynamics and provide critical constraints for improving our understanding and modeling of past climate changes as well as predictions of present and future climate evolution.

3.4 Figures

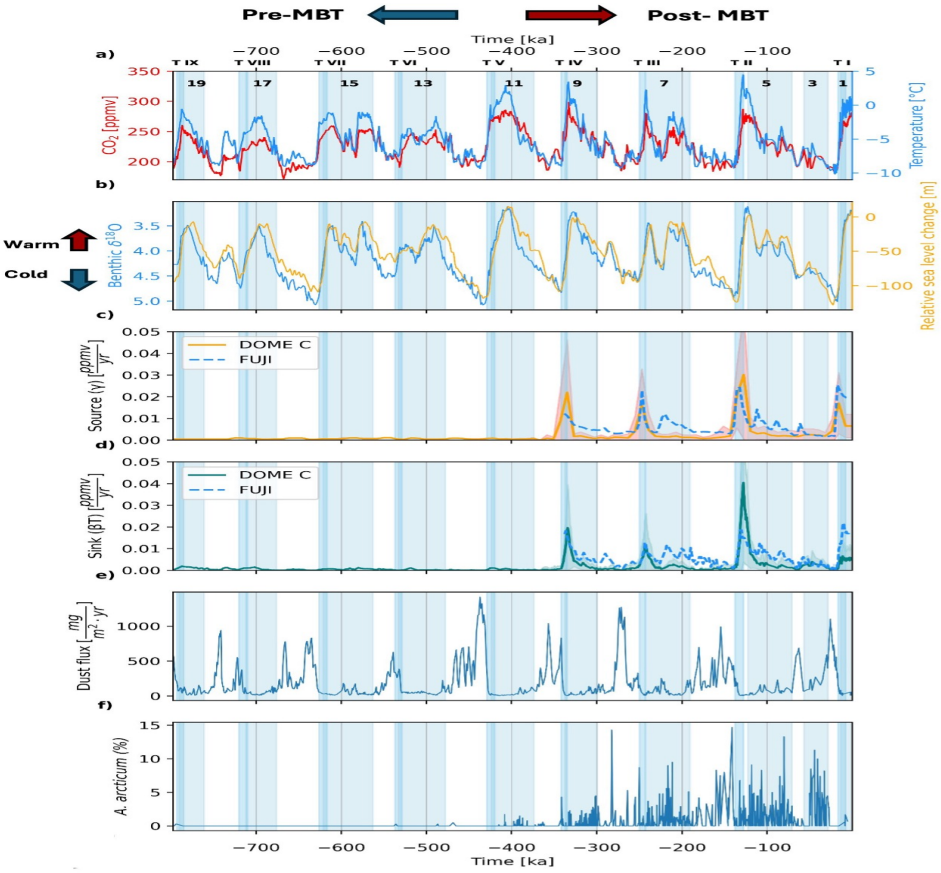

Figure 3.1: *Data compilation and inversion results. (a) Atmospheric CO_2 (red) and T anomaly (blue) oscillations over the past 800 kyrs from the ice core of Dome C. (b) Benthic record (blue) and global relative sea level change (orange) reconstructions, respectively. Benthic y-axis was reversed for visualization purpose. (c) γ flux time history retrieved in the ice core of Dome C (orange, solid line) and Dome Fuji (blue, dashed line). (d) βT flux time history retrieved in the ice core of Dome C (green, solid line) and Dome Fuji (blue, dashed line). (e) Dust flux retrieved in the ice core of Dome C. (f) Percentage abundance of the species Acetabulastoma arcticum in the Arctic region.*

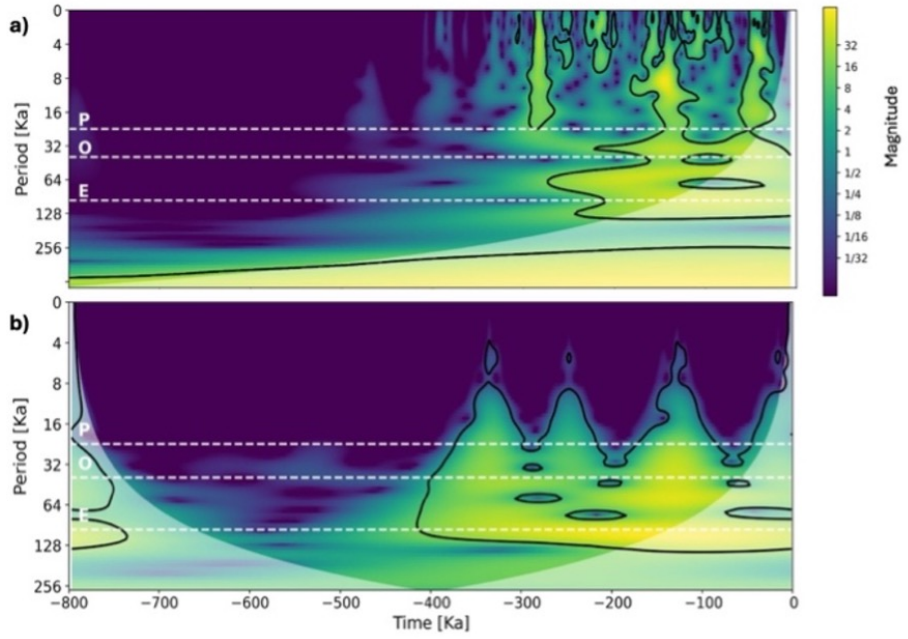

Figure 3.2: *Wavelet coherence transform analysis. Significative changes in periodicity of the percentage abundance of Acetabulastoma arcticum record and γ are tested in (a) and (b), respectively. Dashed horizontal lines and respective E, O, and P labels are the eccentricity, obliquity, and precession orbital cycles. Black contours enclose regions with $> 95\%$ confidence while white shaded areas indicate the cone of influence.Data compilation and inversion results.*

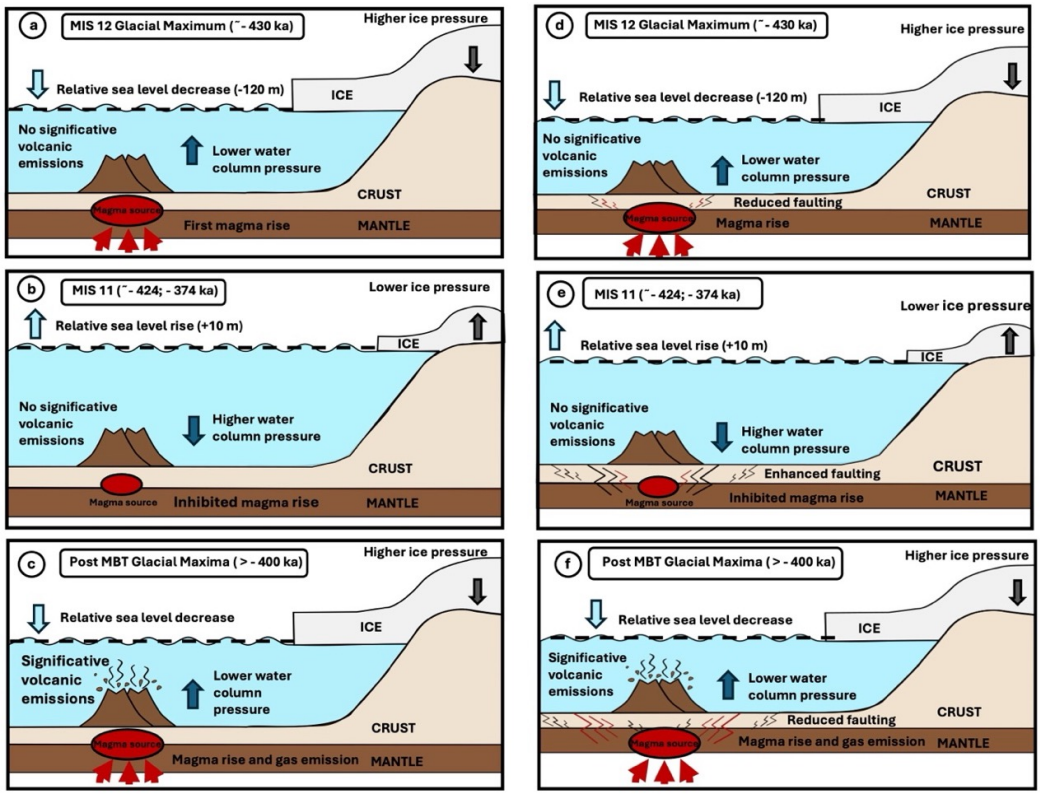

Figure 3.3: *Schematic representation of interpretative scenarios. (a-c) First scenario: diagrams describing how sea-level excursions may trigger MORs degassing since post-MBT glacial-interglacial cycles. (a) The highest sea level drop (-120 m compared to present sea level) occurred during MIS 12 Glacial Maximum ~430 ka, leading to the first submarine magma rise. Lag due to slow magma ascent prevents significative emissions at this stage. (b) The long interglacial of MIS 11 inhibits volcanic emissions due to the high pressure exerted by the water column. (c) Magma – and therefore CO_2 – degasses during MIS 10 Glacial Maximum. (d-f) Second scenario: diagrams describing how enhanced faulting in a context of high sea-level stand may facilitate MORs degassing since the MBT. (d) Reduced faulting along MORs flanks during MIS 12 and pre-MBT cycles limits magma rise during low sea-level stands. (e) Faulting enhancement caused by the long interglacial and higher sea-level rise of MIS 11. At this stage, water column pressure inhibits magma ascent. (f) Preexisting faulting facilitates magma ascent since the MIS 10.*

3.5 Methods

3.5.1 Data

Our study is based on the inversion of the central, temporal derivative of CO_2 computed from the Dome C ice core record:

$$\frac{dC}{dt}_{(i)} = \frac{CO_{2(i+1)} - CO_{2(i-1)})}{t_{(i+1)} - t_{(i-1)}} \tag{3.2}$$

with i being the i-th data point of the CO_2 record. For the analysis, we choose to use the original Dome C compilation [142], rather than the revised version [8], because the uneven time distribution of data-points during the last glacial-interglacial cycle in the latter reference biases the $\frac{dC}{dt}$ calculation (Fig.3.4a, b). Given the lack of information on the data uncertainty, we impose a constant uncertainty of 10^{-5} $\frac{ppmv}{yr}$ on the $\frac{dC}{dt}$ dataset, which we consider reasonable as it approximates one percent of typical $\frac{dC}{dt}$ values. With regards to the T time history, the record results from the analysis on δD of the same ice core [9]. The T time series is not inverted during the run but used to solve the forward model of Eq.3.1 from the main text. Additionally, we normalize T by subtracting its minimum value from all entries to ensures non-negative values and avoid misleading interpretations of the resulting γ and βT time histories.

3.5.2 Rj-McMC algorithm

3.5.2.1 Algorithm implementation

We use a recently developed reversible-jump Markov chain Monte Carlo (rj-McMC) algorithm [122] to retrieve the time histories of unknown parameters γ and β in Eq.3.1 of the main text. The algorithm, which operates in a Bayesian framework, retrieves the most probable solutions for γ and β by collecting model samples from a posterior probability distribution (PPD), the combination of the prior assumptions about the observed $\frac{dC}{dt}$ time series and the likelihood computed between the generated and observed signal of $\frac{dC}{dt}$, further assessing for parameter uncertainties. Since γ and β likely follow a multimodal distribution, it is preferable to use statistical rather than analytical

methods to solve the PPD [116]. We collect models in 50 independent Markov chains and follow the Metropolis-Hastings sampling method [114] to generate a model ensemble proportional to the PPD. We introduce a reversible-jump component [110] to allow the algorithm to directly infer the number of temporal changes of γ and β from the data, thereby reducing the degree of subjectiveness. Finally, we extend the rj-McMC algorithm to the Hierarchical Bayes' [167]8 approach by introducing a model parameter, ω, which scales the noise within the $\frac{dC}{dt}$ time series, allowing to assess whether the most suitable data uncertainty. The algorithm estimates the data error, $\sigma(m)$, during the likelihood computation as follows:

$$\sigma(m) = \sigma_0 10^{\omega} \tag{3.3}$$

where m is the current model and σ_0 is the original $\frac{dC}{dt}$ uncertainty. Finally, every model sampled along the chain consists of an array containing the following model parameters:

$$m = (k, t, \gamma, \beta, \omega) \tag{3.4}$$

where k is the number of temporal γ and β changes, t is the temporal mid-point of k, γ and β are the source and amplificatory sink flux terms, respectively, and ω is the scaling noise parameter. While we report here the general features of the algorithm, more details and a model representation can be found in Ref. [122].

3.5.2.2 Prior information

Rj-McMC algorithms have the advantage of avoiding the fine-tuning of model parameters thereby minimizing bias derived from subjective choices [122],[166]. Yet, prior information and different assumptions critically affect the rj-McMC sampling during an inversion process, leading to different parametrization solutions. In the main analysis, we use a uniform prior probability distribution for parameter exploration to abstain from the choice of preferred values, making the random selection of model parameters from Eq.3.4 as objective as possible. Moreover, we constrain the parameter space into a reasonable interval to allow a faster convergence to the solution (Table I). With regards to model parameters γ and β, we bind them to be positive to avoid misleading interpretation of the resulting flux histories. We consider a range for γ which spans the double of the maximum oscillation of $\frac{dC}{dt}$ and reduce of one order of magnitude β to scale it with T time series. In addition,

the used rj-McMC algorithm can data-infer the model dimensionality (i.e., number of γ and βT changes) and model uncertainty ω (Eq.3.3), warranting the objective reconstruction of γ and βT time histories. To corroborate the result discussed in our analysis, we here present three useful tests.

Model Parameter	**Min**	**Max**
t [yr]	-797,099.0	0.0
γ $[\frac{ppmv}{yr}]$	0.0	0.008
β $[\frac{ppmv}{yr\,°C}]$	0.0	0.0008
k	1	100
ω	-1.0	3.0

Table I: *Range values for uniform sampling of t, γ, β, k and ω used for the inversion. k and ω are dimensionless quantities.*

$\frac{dC}{dt}$ *inversion for the period 800 - 400 ka.*

In the main analysis, we find a reduced variability of the γ and βT CO_2 fluxes from ˜800 to ˜400 ka compared to post-MBT glacial-interglacial cycles, suggesting stronger $\frac{dC}{dt}$ - T coupling. To corroborate this result, we present two inversions considering the period 800 – 400 ka alone. Net of other prior conditions, in the first test we invert the $\frac{dC}{dt}$ time series using a simple McMC algorithm (i.e., we constrain the model dimensionality to 1 while allowing for changes of γ and β, whose values apply over the entire time series), while in the second test, we enable for a classical rj-McMC parametrization as done for the main analysis (i.e., we allow for multiple γ and β value changes in the time series). Results from the first test (Fig.3.5a-c) retrieve a single γ value and reduced βT variability comparable in magnitude to that found in the 800 – 0 ka inversion described in the main text. Likely, the second test (Fig.3.6a-c) marks a similar magnitude trend, with higher γ and βT variability arising between ˜600 - 500 ka. However, peaks are one order of magnitude lower than ones presented in the main text, confirming the reduced γ and βT variability over the period. Furthermore, higher dimensionality found in the main 800 – 0 ka inversion (Fig.3.7a) compared to the reduced one from the second 400 - 0 ka test (Fig.3.7b) further confirms the trend

of strong $\frac{dC}{dt}$ - T coupling before 400 ka.

$\frac{dC}{dt}$ inversion constraining the model parameter ω.

The main advantage of implementing a hierarchical Bayes' in a rj-McMC algorithm is the possibility to test for the reliability of the data uncertainty provided by the observed data record [167]. In our analysis, the variation of model parameter ω during the inversion scales the $\frac{dC}{dt}$ uncertainty, affecting the model dimensionality through the reduction (increase) in γ and β changes whether the uncertainty is high (low). Thus, scaling the $\frac{dC}{dt}$ uncertainty enables to retrieve the most significant times at which $\frac{dC}{dt}$ – T decoupling occurs, avoiding the overfit of parametrized fluxes. Here, we provide the CO_2 reconstruction using the resulting γ and βT fluxes from our analysis, in which we enabled the $\frac{dC}{dt}$ uncertainty scaling (Fig.3.8), and compare it to the results from a test conducted constraining ω=0 (Fig.3.9). The CO_2 reconstruction from the analysis described in the main text (Fig.3.8a-c) fails in perfectly reproducing the entire CO_2 record due to reduced γ and βT variability (Fig.3.8d) following high model uncertainty (Fig.3.8e). On the contrary, constraining ω=0 leads the algorithm to search for higher precision $\frac{dC}{dt}$ values, perfectly fitting the CO_2 time series (Fig.3.9a-c) by largely incrementing the amount of γ and βT changes (Fig.3.9d, e), but overfitting the $\frac{dC}{dt}$ record and limiting the generalization of the flux results. Hence, the scaling of the data uncertainty enables to retrieve the underlying features of the carbon cycling, making the main text analysis more generalizable.

$\frac{dC}{dt}$ inversion using different Sea Surface Temperature (SST)

In the forward model definition (Eq.3.1 from the main text), the T trend (Ref.[9]) is not treated as a datum to be inverted but it serves as a supporting information, assumed to be known with infinite precision and globally representative of atmospheric $\frac{dC}{dt}$ changes. Consequently, the selection of different T trends can influence the analysis. To evaluate this, we perform two separates $\frac{dC}{dt}$ inversions using two distinct T time series: one derived from sea surface temperatures (SST) based on alkenone analyses of marine sediments from the North Atlantic (Ref.[218], Fig.3.10a), and another using a stack of SST records from tropical regions (Ref.[219], Fig.3.11a). Both inversions

reveal a reduced flux variability during pre-MBT glacial-interglacial cycles, with γ and βT pulses arising since ˜350 ka (Fig.3.10b, c) and ˜250 ka (Fig.3.11b, c) in the North Atlantic and the tropics, respectively. The later starting of carbon pulses at the tropics suggests a delayed latitudinal trend from high to low latitude in the global carbon cycle, potentially linked to the stronger influence of ice-volcanic interaction at poles. However, while using regional T trends can unveil local features of $\frac{dC}{dt}$ – T coupling/decoupling, the atmospheric T trend used in the main analysis is considered a global representation of T [216], allowing a global reconstruction of the flux trends.

3.5.2.3 Computation time

The code, written in Fortran77, runs on a High-Performance Computer cluster exploiting an Omni-Path Cluster architecture and Intel® Xeon Phi^{TM} processors. The analysis presented in the main text consisted of 50 independent Markov chains of 10^6 models each. The first half of the sampled models for every chain was discarded as part of a burn-in phase. The time required to complete the inversion was ˜4 hours.

3.5.3 Cross-correlation analysis

We tested for cross-correlations between the reconstructed surface CO_2 source flux (γ), T, and the reconstructed surface CO_2 sink flux (βT) time histories to assess lead-lag relationships (Fig.3.12a, b). To this aim, we used Python (version 3.12.1) adopting the Numpy.correlate function from the Numpy library. In the analysis, γ represents the sliding signal while βT and T the overlapped signals.

3.5.4 Code availability

The rj-McMC code used for the analysis, including the input $\frac{dC}{dt}$ and T time series, and produced output fluxes are available at the following GitHub repository `https://github.com/LucaCastrogiovanni/rj-split-ice-cores.git`.

3.5.5 Aknowledgments

We are grateful to the Italian Ministry of Education, MUR, for providing support for this work also through the Project Dipartimenti di Eccellenza, TECLA, Department of Earth and Environmental

Sciences, University of Milano-Bicocca. This work was also funded through the ERC MATRICs project (101167761) and PS was further supported by the Experienced Researcher Fellowship of the Alexander von Humboldt Foundation.

3.6 Figures methods

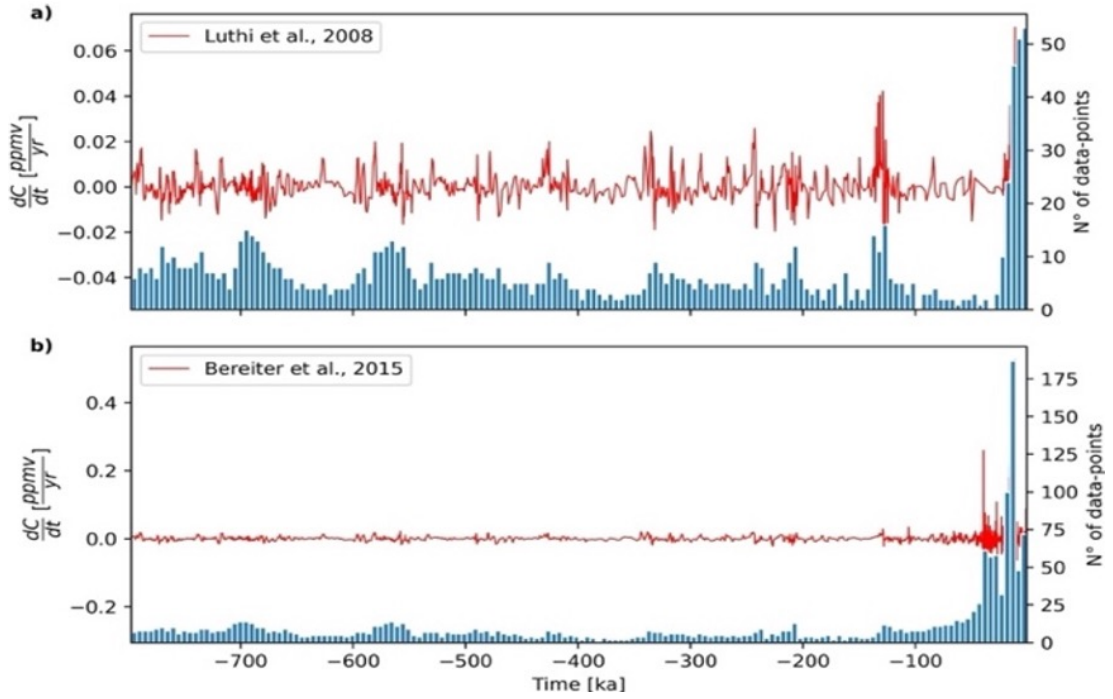

Figure 3.4: *Central derivatives (red lines) used for the inversion and number of data-points every 5 kyrs from Ref.[142] (a) and Ref[8] (b)*

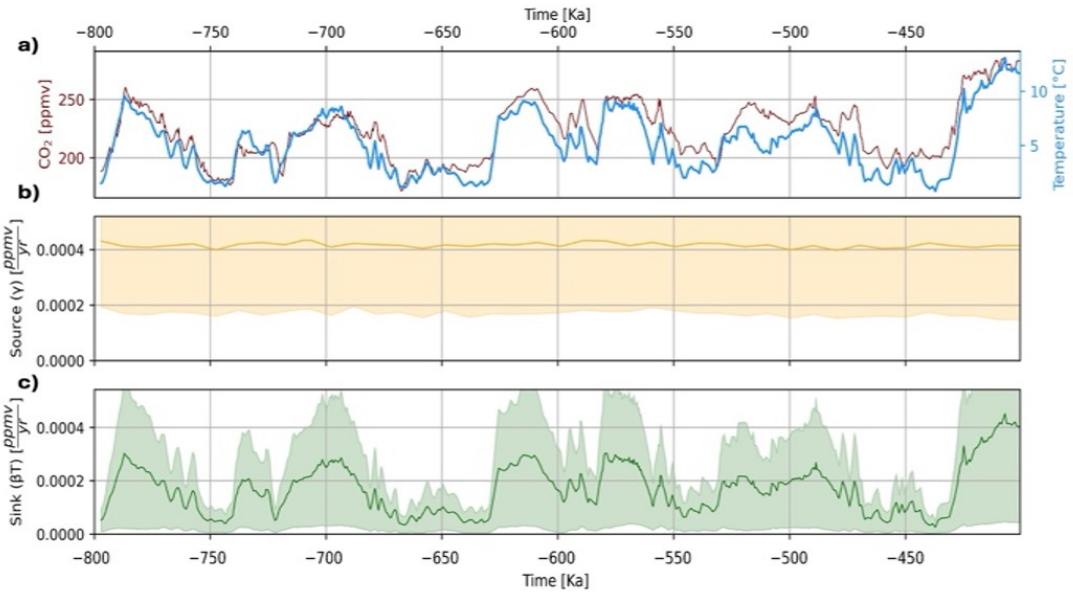

.

Figure 3.5: *Results from the first test as a simple McMC inversion. (a) 800-400 ka subset including the atmospheric CO_2 and T reconstructions from Refs.[142], [9] shown for reference with flux results. (b) γ source flux time history. (c) βT sink flux time history. The reduced variability and magnitude align with results from the main text over this period.*

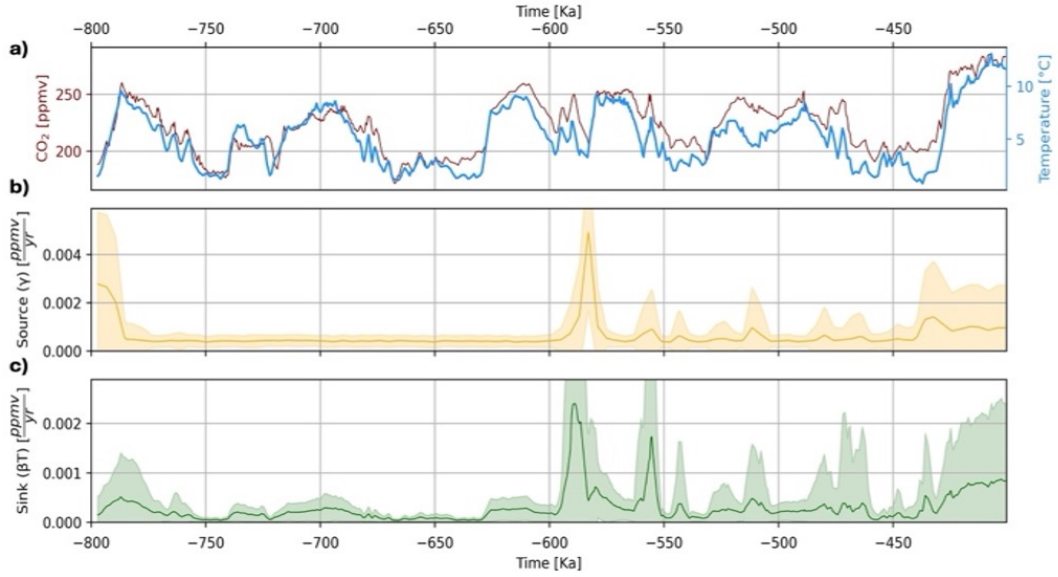

.

Figure 3.6: *Results from the second test as a rj-McMC inversion. (a) 800-400 ka subset including the atmospheric CO_2 and T reconstructions from Refs.[142], [9] shown for reference with flux results. (b) γ source flux time history. (c) βT sink flux time history. The higher variability compared to the first test arises from the use of a rj-McMC, where the small γ and βT magnitudes align with reduced pre-400 ka flux variability in the main text.*

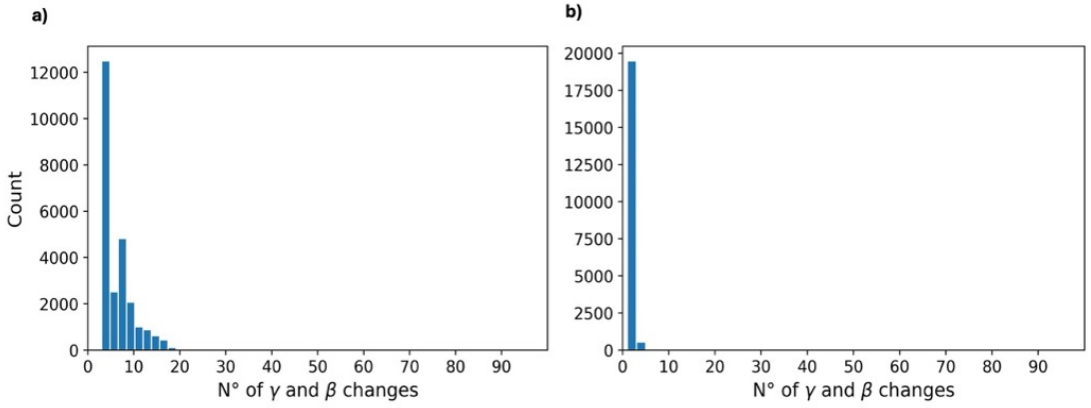

.

Figure 3.7: *Distribution for the number of γ and βT changes from the main analysis (a) and the inversion from the second test (b). Although results from the second test express pre-400 ka variability, the number of γ and βT changes is lower (i.e., ˜1), confirming the reduce flux variability pre-400 ka.*

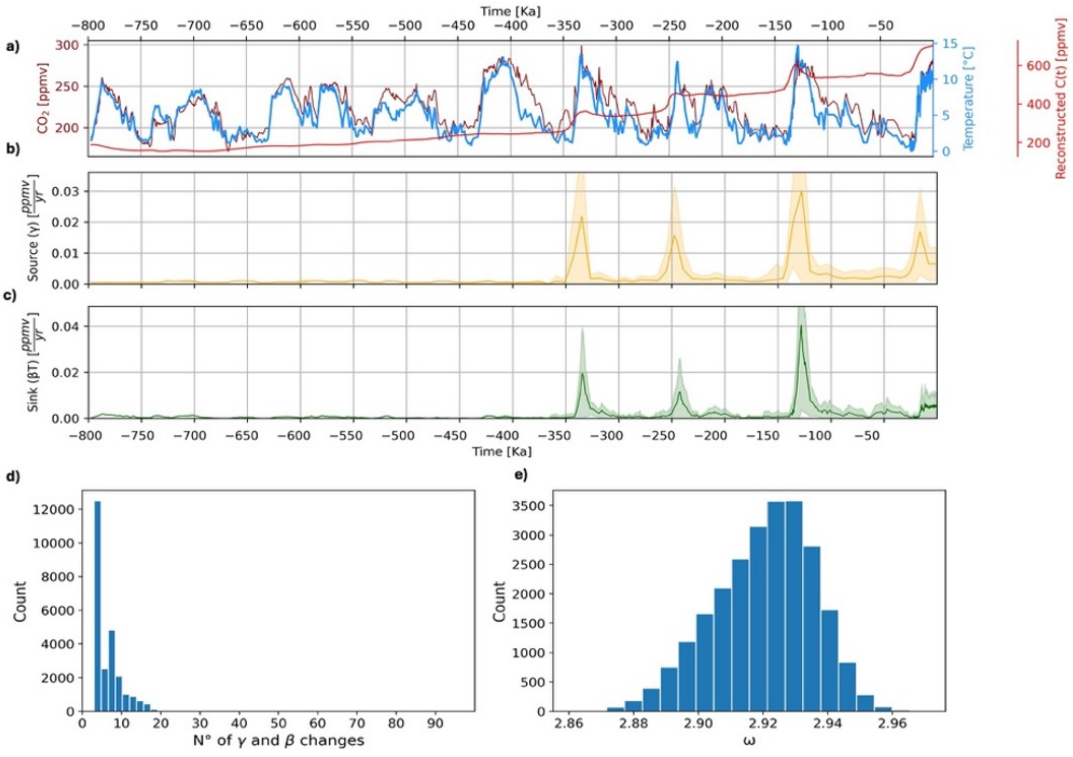

Figure 3.8: *Results from the main text inversion as a comparable reference with results from test in Fig.3.8. (a) CO_2, T, and reconstructed C(t) curve using the retrieved γ and βT fluxes. (b-c) Retrieved γ and βT flux time series. (d) Distribution for the number of γ and βT changes. (e) The distribution of the uncertainty scaling parameter ω. The high uncertainty on inverted data leads to high value of ω and reduced variability of fluxes.*

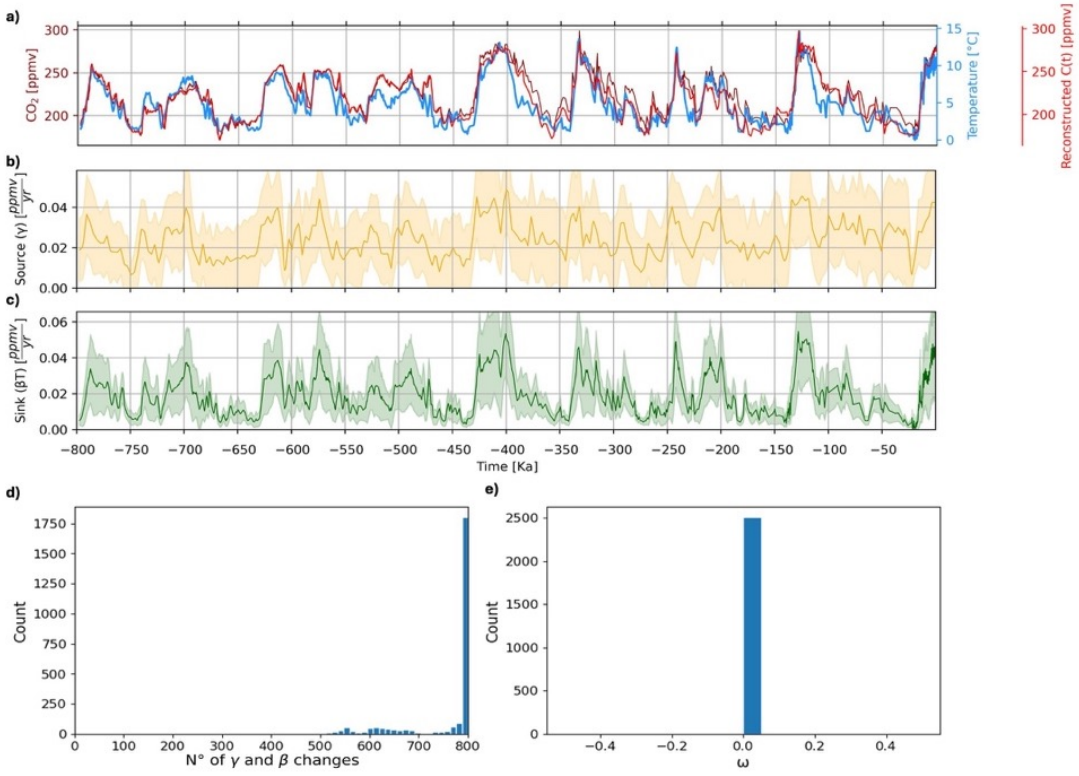

Figure 3.9: *Results from the inversion when setting* $\omega = 0$. *(a)* CO_2, *T, and reconstructed C(t) curve using the retrieved* γ *and* βT *fluxes. (b-c) Retrieved* γ *and* βT *fluxes time histories. (d) Distribution for the number of* γ *and* βT*changes. (e) The distribution of the uncertainty scaling parameter* ω. *The use of no scaling factor* ω *leads to a large increment in the number of*γ *and* βT *changes, preventing to assess significant carbon cycle flux changes.*

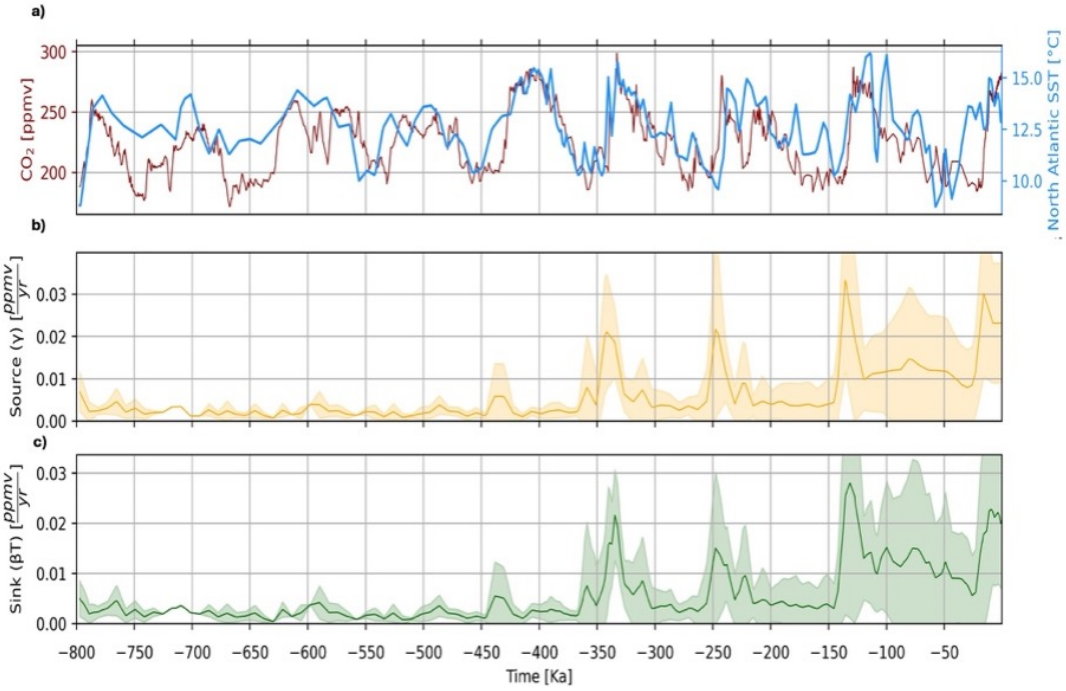

Figure 3.10: *Flux histories reconstruction using the global CO_2 record and the alkenone SST reconstruction in the North Atlantic from Refs.[142], and [218], respectively. (a) Global CO_2 and local North Atlantic SST record. (b) Source flux time history reconstruction. (c) Sink flux time histor*

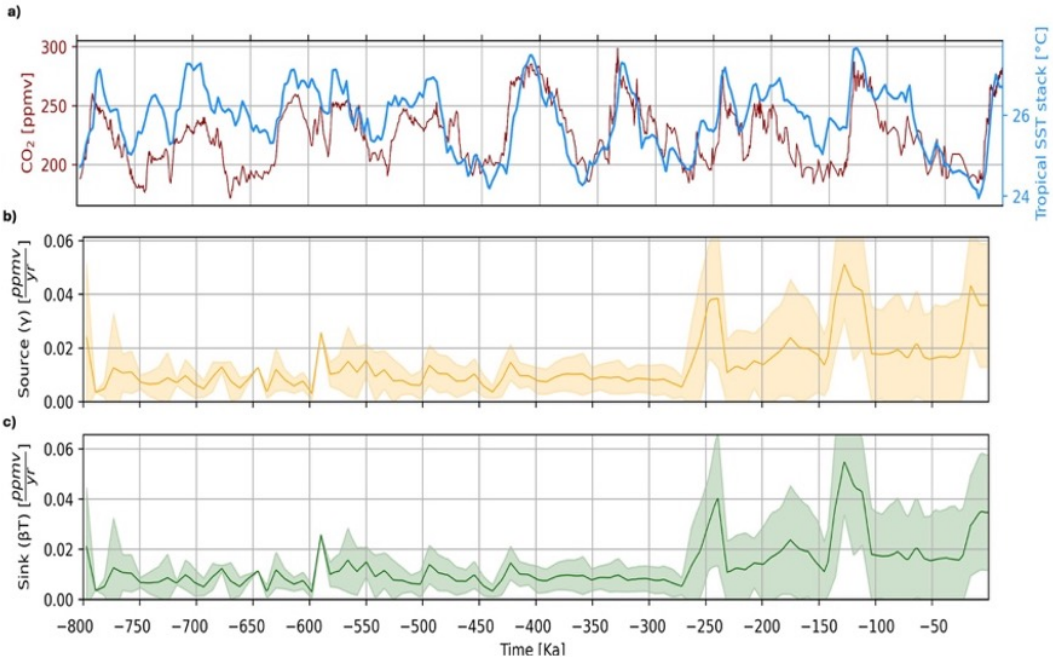

Figure 3.11: *Flux histories reconstruction using the global CO_2 record and the stacked alkenone SST reconstruction at the tropics from Refs. [142], and [219] , respectively. (a) Global CO_2 and tropical stack SST record. (b) Source flux time history reconstruction. (c) Sink flux time history.*

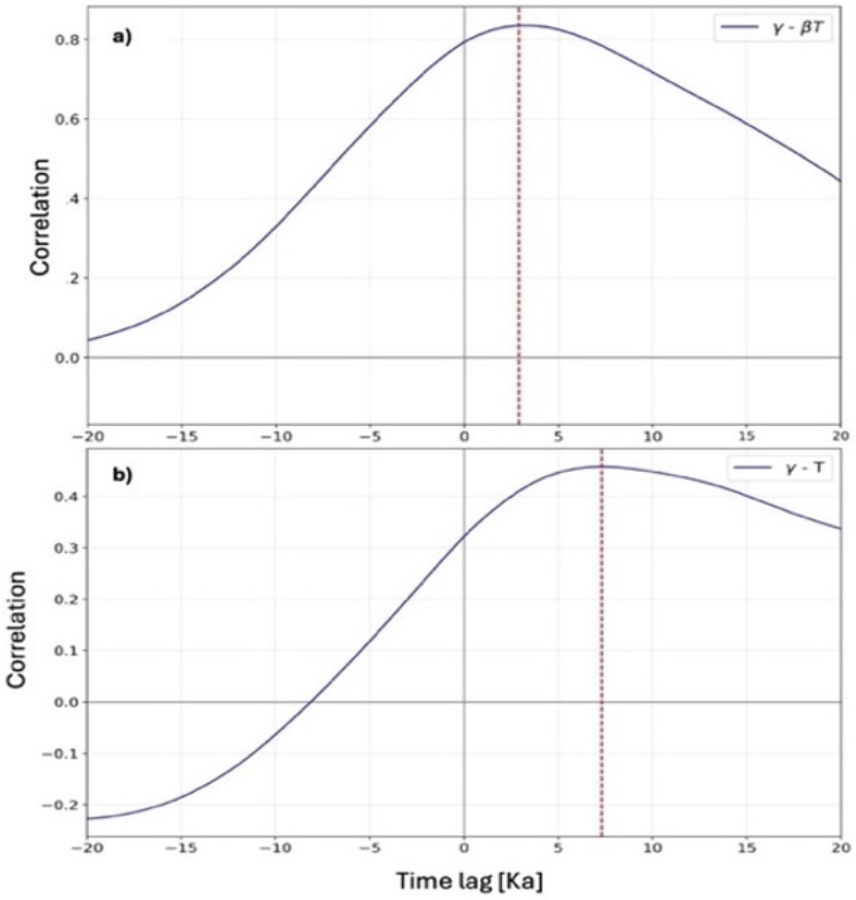

.

Figure 3.12: *Cross-correlation analysis of γ against βT (a) and T (b). Maximum lag correlation is found with a lag of ˜3 ka and ˜7 ka.*

Chapter 4

Carbon fluxes throughout the Cenozoic

The Cenozoic climate provides evidence of different climate states from present day conditions, offering important hints of how Earth's system may respond to anthropogenic climate warming in the future. The long-term cooling detected from proxies since ˜50 Ma plausibly set the conditions for the onset of an Antarctic ice cap [86], permanently driving Earth into a different climate state. In contrast, superimposed warmth events and periods such as the PETM, EECO, MECO, and MMCO likely contributed to faunal turnover, the evolution and spreading of modern mammalian species, including primates [237], [238], [239]. Some of these periods, such as the PETM and MMCO, have been occasionally suggested as past analogs of present day climate change, given the rapidity of CO_2 and T change [240] and similar projected CO_2 concentrations [241]. Nevertheless, understanding Cenozoic climate and its implication for present day climate change relies on the quantification of carbon fluxes, on which we lack conclusive estimates. In this Chapter, I present a third case study, which involves the inversion of a multi-proxy CO_2 record to reconstruct continuous source and sink flux time histories over the past 66 Ma. The study, which is now in preparation, suggests a strong influence of the Antarctic ice cap in modulating the CO_2 - T coupling, with higher carbon flux variability before 34 Ma likely related to geodynamic processes. The presented work will provide to the scientific community a reliable, data-inferred carbon flux curve to be used as a boundary condition in future modelling works.

Input and output fluxes of surface CO_2 throughout the Cenozoic

Castrogiovanni L.[1, 2], Sternai P.[1,3], Pasquero C. [1], Piana Agostinetti N.[1], Longman J. [2], Vaes B.[1], Ostorero L. [1]

[1]Department of Earth and Environmental Sciences, University of Milano-Bicocca, Italy.

[2]Department of Geography and Environmental Science, Northumbria University, UK.

[3]GFZ, German Research Centre for Geosciences, Potsdam, Germany.

Status: In preparation

Abstract

The Cenozoic era covers the last ˜66 Myrs of Earth's history. Proxy records demonstrate that, after a first warming phase lasting ˜15 Myrs, CO_2 and temperature steadily decrease since ˜50 Ma, leading the most recent transition from a greenhouse to icehouse climate state after the onset of the Antarctic ice cap ˜34 Ma. Superimposed to overall climate degradation, warm peaks and optima punctuate the trend interrupt the CO_2 and temperature decline. So far, proxy records have allowed the constrain of the absolute budget of CO_2 but they struggle to provide insights in terms of source and sink CO_2 fluxes. In this study, we use a novel Bayesian algorithm to quantify CO_2 flux changes in the Cenozoic through the parametrization of a simple formulation of the geological carbon cycle. Results reveal higher source and sink flux variability before 34 Ma compared to more recent times. We suggest that geodynamic processes mostly acting during the lower Cenozoic, such as the closure of the Neo-Tethys, may have sustained CO_2 emissions during the period. We further suggest that the overall decrease in CO_2 fluxes detected since ˜35 Ma facilitates the onset of an Antarctic ice cap, resulting in following enhanced albedo feedbacks since then.

4.1 Introduction

Understanding how the Earth system responds to changes in the amount of surface CO_2 is critical to improve predictions of future climate and adjust policy strategies accordingly. Geological proxies provide indirect records of past surface CO_2 changes throughout the Cenozoic era - the last 66

Myrs - and offer the opportunity to assess climate trends under slow and fast evolving conditions [242],[243]. They show a long-term unsteady surface CO_2 and T decline since around 50 Ma [244], [48], [169] (Fig. 4.1a), indicating imbalances in the geological carbon cycle - the slow exchange of carbon between deep and surface reservoirs mediated by geological processes [20]. This trend, involving the transition from a green-house to an ice-house state with the onset of perennial ice-caps on Antarctica ˜34 Ma [86] and Northern Hemisphere glaciations ˜2.6 Ma [60], is often ascribed to two end-member mechanisms related to the India-Asia collision, without established agreement: on the one hand, the drawdown of surface CO_2 due to the intensification of silicate weathering following the uplift and erosion of the Himalayan-Tibetan orogen [169], [154], on the other hand, the waning in volcanic degassing from Neo-Tethyan arcs due to the progression of continental collision [48], [94]. Superimposed on the long term Cenozoic cooling, shorter periods of increasing CO_2 and T, notably the abrupt Paleocene-Eocene Thermal Maximum (PETM) ˜56 Ma [245], the Early Eocene Climatic Optimum (EECO) between ˜54 – 49 Ma [246], [126], the Middle Eocene Climatic Optimum (MECO) ˜40 Ma [247], and the Middle Miocene Climatic Optimum (MMCO) ˜15 Ma [248], characterize the Cenozoic climate [249]. Despite their distinct climatic, biological, and geological signature, causes for these aberrations [10] remain debated, with explanations commonly involving specific orbital configurations [89], [88], gas hydrates release [90], rapid CO_2 degassing from Large Igneous Provinces (LIPs) [47], or volcanic flare-ups from the Neotethyan arc [91].

We thus lack of a comprehensive explanation for Cenozoic climate trends, and one of the limits is the poor quantification of CO_2 fluxes across Earth's reservoirs which could pinpoint dominant carbon cycling mechanisms and assess relationships between CO_2 concentrations and T changes as reconstructed from paleo-climate proxy records. Classic, straightforward approach is the estimation of CO_2 sources and sinks by mean of paleo plate modelling tools [250], where solid Earth CO_2 flux information are a function of seafloor spreading, volcanic arcs evolution, and the amount of subducted sediments across convergent margins (refer to [251] for an exhaustive review and discussion on the topic). These tools provide however a first-order interpretation to surface CO_2 sources and sinks, excluding a plethora of mechanisms involved in the carbon cycle, for instance related to land and ocean reservoirs. Box and spatially-informed numerical models (e.g., GEOCARB [95], [252], COPSE [253] or GEOCLIM [96]) includes more complex Earth system interactions, providing predictions of long-term (i.e. times > 10^4 years) CO_2 trends based on prescribed physical laws, which can be compared to the proxy record in order to derive information on climate-driving

mechanisms [6]. However, despite improved match between predictions and proxy data by recently coupled box and spatially informed models [6], forward models rely on subjectively chosen physical relationships, input parameters and boundary conditions, which limits the reliability of modeling outcomes. A third class type of modelling is, instead, the inverse approach, enabling optimal parametrizations of carbon cycling and mass balance equations directly from proxy data [100]. However, previous works neglected links between CO_2 and T [100], [174], or attempted to assess climate sensitivity from palaeo-CO_2 proxies [249], rather than CO_2 fluxes across Earth's reservoirs. A novel Bayesian algorithm that links paleo-CO_2 and paleo-T data was recently developed [122] to estimate paleo-CO_2 fluxes and assess timing of statistically significant coupling/decoupling between CO_2 and T changes. Successfully tested on ice core data to reproduce late Pleistocene glacial-interglacial cycles CO_2 fluxes, we here extend the methodology to the paleo-climate proxy record of the last 66 Ma, retrieving unprecedented estimates of Cenozoic input and output fluxes of surface CO_2.

4.2 Data and Methods

4.2.1 Data

Studies that aim to reconstruct paleo-CO_2 levels beyond ˜800 ka require the use of proxies (e.g., boron isotopes, stomata density, paleosols, liverwort) which indirectly inform about past climate conditions. Dealing with this, the use of a single type of proxy considerably limits the interpretation of past climate, usually requiring a more robust, multi-proxy approach [254], [255]. In this work, we reconstruct the time histories of input and output CO_2 fluxes by inverting the central, temporal derivative of CO_2 (i.e., $\frac{dC}{dt}$), computed from the multi-proxy, 500-kyr smoothed CO_2 record from [249] (scatter and solid, dark red line in Fig. 4.1 a) as follows:

$$\frac{dC}{dt}_{(i)} = \frac{CO_{2(i+1)} - CO_{2(i-1)}}{t_{(i+1)} - t_{(i-1)}} \tag{4.1}$$

with i being the i-th data point of the CO_2 record. Likewise, analysis of the oxygen isotope ratio $\delta^{18}O$ in marine carbonate sediments is widely used to reconstruct Cenozoic climate, providing information about past deep sea T and global ice volume changes [256]. In this study, we use

as a supporting information the continuous, global mean surface T record provided by [257], who corrects for the deep sea T retrieved in the original record from [258].

Prior to performing the inversion, we preprocess the data by linearly interpolating the $\frac{dC}{dt}$ record into the T time series to ensure that both series have the same time step. Although the opposite interpolation of T into $\frac{dC}{dt}$ data would be preferable, as it keeps the inversion dataset unprocessed, it leads to the over-smoothing of T during key Cenozoic events such as the PETM or the Northern Hemisphere icesheet formation, potentially biasing the analysis. Given the large amount of data-points (˜24,000) of the two time series, also, we decide to downsample both the T and the interpolated $\frac{dC}{dt}$ curves at 125 kyrs intervals. We consider this a reasonable time step to both preserve the original trend and magnitude while reducing the amount of data-points, enabling a faster, yet robust, inversion analysis. Finally, lacking of information about $\frac{dC}{dt}$ standard deviation, we subjectively assign a constant standard deviation of 10^{-5} (i.e., ˜$\frac{1}{10}$ of the original $\frac{dC}{dt}$ signal), suitable to represent the large uncertainty involved during the period.

4.2.2 Methods

The tight relation between CO_2 and T trends prevents the clear assessment of dominant mechanisms driving Cenozoic climate. In this study, we couple a novel inversion algorithm [122] with a simple formulation of the geological carbon cycle [76] to link $\frac{dC}{dt}$ to T changes as follows:

$$\frac{dC}{dt} = \gamma - \beta T \tag{4.2}$$

where γ and β are unknown parameters which modulate the source CO_2 flux and the amplification term of the CO_2 sink flux, respectively. We assume T to drive the long-term CO_2 removal through intensification of silicate weathering triggered by enhanced atmospheric circulation and associated rainfall in response to rising T. The input (γ) and output (βT) terms from Eq. 4.2 encapsulate all the mechanisms contributing to the CO_2 rise and sink. However, the relatively fast exchange of carbon (i.e., $< 10^4$ years) among land, ocean, atmosphere and ice allows us to treat the surface as a unique reservoir on a multimillion-year time scale, thereby ascribing the Cenozoic $\frac{dC}{dt}$ variations mainly to deep-surface carbon exchange mechanisms [217], [23].

The algorithm, which is based on a reversible-jump Markov chain Monte Carlo (rj-McMC) implementation [110], reconstructs continuous time histories of the unknown parameters γ and

β. Given its Bayesian nature, the reconstruction is achieved by sampling a posterior probability distribution (PPD), defined by the product between a prior probability distribution and a likelihood function. The former represents the prior knowledge about Cenozoic CO_2 fluxes, such as the forward model definition or assumed range values of γ and β, while the latter is the difference between the model generated (i.e., synthetic) and the observed $\frac{dC}{dt}$ record. Despite the simple formulation of Eq. 4.2, the PPD cannot be solved analytically and requires the use of statistical approaches, such as the model sampling [160]. One of the most used technique is the Metropolis-Hastings sampler [114], which ensures an effective model selection leading to a final solution proportional to the PPD [161]. To avoid any bias in the analysis, we also assume unknown the number of γ and β changes over the time series, directly inferring it from data adding a reversible-jump component [110]. Finally, to further an inversion as objective as possible, we add a model parameter ω, to allow the scaling of the $\frac{dC}{dt}$ uncertainty during the likelihood calculation. This assesses a better understanding of data quality used for the inversion. More details about the algorithm recipe and workflow can be found in [122].

4.2.3 Prior information

A key feature when using rj-McMC strategies and, more in general, Bayesian algorithms is the choice of prior information. Here, we use a uniform prior distribution for sampling of model parameters to allow an unbiased sampling. Priors ranges used for different model parameters are reported in Table I. We constrain γ assuming a maximum value equal to the double of the maximum amplitude of the $\frac{dC}{dt}$ signal and we scale β to be ~ $\frac{1}{10}\gamma$ given the contribution of T time series. As a lower boundary, we bind both model parameters to be non negative to avoid any misleading interpretation of the source and sink fluxes.

4.2.4 Computation time

In this work, we collect models in 90 independent Markov chains ran in series, each consisting of $2\text{x}10^6$ models and a burn-in phase of $5\text{x}10^5$ models discarded at the beginning of the chains. The inversion, performed on a personal computer, required ~8 hours.

Model Parameter	**Min**	**Max**
t [Myr]	-67.1	0.0
γ $[\frac{ppmv}{yr}]$	0.0	0.002
β $[\frac{ppmv}{yr\,°C}]$	0.0	0.0002
k	1	100
ω	-1.0	3.0

Table I: *Range values for uniform sampling of t, γ, β, k and ω used for the inversion. k and ω are dimensionless quantities.*

4.3 Results

The analysis returns a good fit between the observed and reconstructed $\frac{dC}{dt}$ (black and red solid lines from Fig. 4.1b), underscoring a lower (higher) $\frac{dC}{dt}$ variability at times where $\frac{dC}{dt}$ couples (decouples) T changes (histogram from Fig. 4.1b, which defines the frequency in time of γ and β changes). Input and output flux reconstructions mirror the results from Fig4.1b, revealing a twofold trend (Fig. 4.1c, d): higher γ and βT variability before 34 Ma suggests a strong CO_2-T decoupling during the early Cenozoic (i.e., pre-34 Ma), therefore requiring additional processes besides T changes to affect the $\frac{dC}{dt}$ trend. In contrast, reduced γ and βT changes since 34 Ma detect a stronger CO_2-T linkage, with $\frac{dC}{dt}$ being more sensitive to T variations, with two exceptions ˜18 and ˜14 Ma involving the appearance of short source and sink pulses. The lack of a lead-lag relationships between γ and βT can ascribe either to a quasi-instantaneous sink response to CO_2 flux increases or smooth temporal resolution, filtering lags lower than million years.

In addition, we plot the net carbon flux – defined as the difference between γ and βT – in units of Mega tons (Mtons) of carbon emitted per year (Fig. 4.1e). Not unexpectedly, the early Cenozoic shows larger variability compared to the late Cenozoic (i.e., post-34 Ma), detecting a net, positive rate of CO_2 emissions ˜66 Ma, ˜56 Ma, ˜54 -51 Ma, and ˜40 Ma. Noteworthy, our retrieved flux magnitudes are overall far below the estimated present day (pre-industrial) emission rates [250]. This likely results from the use of a 500-kyr smoothed curve [249] to reconstruct the CO_2 fluxes,

which underestimates the $\frac{dC}{dt}$ signal due to the reduced amplitude. Nonetheless, the use of a 500-kyr smoothed curve does not affect the reliability of flux trends, enabling a robust reconstruction of CO_2-T coupling or decoupling throughout the investigated period.

4.4 Discussion

These periods are synchronous to the sustained volcanic activity during the Deccan trap formation [259], the PETM [260], to a large part of the EECO [246], and MECO [247].

Cenozoic climate marks the most recent shift from a warm-house to an ice-house climate state, with permanent Antarctic glaciation established at least since the Eocene-Oligocene Transition (EOT) ˜34 Ma [86], [29]. The classical explanation attributes the onset of a stable icecap to thermal isolation of the continent following the progressive opening of the Drake's passage and deepening of the Tasmanian gateway, which separate Antarctica from South America and Australia, respectively [31], [87]. However, model simulations [261] and uncertainties on glaciation timing [262], [263] have increasingly pointed to additional contributing processes, including orbitally induced feedbacks [264], changes in the albedo due to vegetation shifts [265], and declining in CO_2 emissions [48], [266], [267], [268]. Based on our flux results, reduced CO_2 emissions since ˜50 Ma (Fig. 4.1c) compared to the previous warm periods (e.g., the PETM and EECO) suggests a causative link between the late Eocene CO_2 decline and a cooling trend, possibly setting the conditions for a glaciated Antarctica. Moreover, the strong decoupling between $\frac{dC}{dt}$ and T before 34 Ma (Fig. 4.1c, d), requires the contribution of further, unrelated T mechanisms to $\frac{dC}{dt}$ variations, potentially ascribed to the changing geodynamic context of the early Cenozoic. One prominent example is the evolution of the Neo-Tethyan margin. Along the Indian-Eurasian sector, the subduction of large amounts of Indian pelagic carbonates beneath Eurasia has been proposed to sustain high CO_2 levels and global T during the early Cenozoic [48], [269], [270].

Intriguingly, we find a striking correspondence between the key stages of the Neo-Tethyan margin evolution and distinct CO_2 emission regimes, indicating a geodynamic control on long-term climate fluxes (refer to Fig.3 of [48]). High CO_2 emissions coincide with enhanced volcanic activity along the Southern margin of Eurasia during the Paleogene up to the early Eocene (˜65 – 50 Ma) [271], where the lack of data in the Paleocene likely leads temporary low fluxes between ˜63-56 Ma. As the subduction proceeds, we find lower CO_2 emissions between 50 – 40 Ma, with slow, increasing

trend detected since ˜45 - 40 Ma [91], [272], potentially associated with the Arabian-Eurasian collision. Finally, the complete arc extinction ˜35 Ma leads to a sharp drop in CO_2 emissions [48], stabilizing the CO_2 fluxes thereafter. Moreover, the positive net budget of CO_2 emissions at ˜66 Ma, ˜56 Ma, ˜54 -51 Ma, and ˜40 Ma is synchronous to the sustained volcanic activity during the Deccan trap formation [259], the PETM [260], to a large part of the EECO [246], and MECO [247], respectively, further corroborate this view. However, while our results underscore a peculiar synchronicity between magmatism associated with the Neo-Tethyan margin evolution and our reconstructed flux trends, we cannot exclude the contribution of other major geodynamic events to explain the temporal CO_2 variability before 34 Ma. Huge amounts of basalts emitted during a fast-spreading phase of the North-Atlantic Ocean Ridge ˜56 Ma likely contributes to the EECO [272], defined in our results by sustained CO_2 emissions until 50 Ma, when an abrupt spike of CO_2 sink seems to interrupt the emission trend. The ophiolite emplacement on Cuba and Hispaniola between ˜50 – 40 Ma [273] and the magmatic cessation in the Basin and Range during the late Eocene [274] may also affect the gradual Cenozoic CO_2 decline. The onset of an intraoceanic subduction margin involving the Aleutian, Kuril and Izu-Bonin Marianas trenches ˜50 Ma is comparable in length to the Neo-Tethys margin [275] and could follow a similar degassing trend, even though intraoceanic margins provide small amounts of carbonate subducted – and thereby limited CO_2 emissions. Hence, it is plausible that a combination of geodynamic processes and resulting feedback mechanisms, rather than a single event, set the conditions for the gradual reduction in CO_2 emissions, leading to the Antarctic ice cap glaciation.

From a radiative energy standpoint, Earth's Energy Imbalance (EEI) calculations – defined as the difference between the Absorbed Solar Radiation (ABS) and the Outgoing Longwave Radiation (OLR) (Section 1.2) – widely support the hypothesis of a decline in the partial pressure of CO_2 (pCO_2) as a precondition for perennial glaciations [276], [32]. A reduction in pCO_2 increases the amount of OLR, with consequent amplification of the Earth's cooling. $\frac{dC}{dt}$ – T coupling since ˜34 Ma (Fig. 4.1c, d) further corroborates the idea that imbalances in the radiative budget may have affected climate dynamics since the Oligocene (i.e., ˜34 – 23 Ma), resulting in non-linear responses to orbital forcings [258]. Besides icecaps, the increased reflectivity of continents in sparse vegetation and glaciated regions, such as high elevation plateaus, have the potential to further reduce T [276]. The emblematic case of the Tibetan Plateau – the highest and widest on Earth – which first heights above 3.5 km in the Eastern sector date at least ˜35 Myr [277] is in line with an increase

in reflectivity at the tropics, critical latitude for the global radiative budget. However, lack of consensus on the reliability of paleo-elevation studies [278], complex deformations and the presence of wide-spread vegetation in the area do not allow for an assessed contribution of the Tibetan Plateau to the increased albedo during the Oligocene [50]. Unfortunately, the unbiased recognition of processes associated with long-term CO_2 drawdown during the Oligocene is a non-trivial task, given the coarser in time and mostly regional data (prevalently from the Southern Hemisphere) compared to the Eocene and Miocene (i.e., 23.0 – 5.3 Ma) periods [249]. Our results show a slight, stable CO_2 removal during this period (Fig. 4.1e), suggesting long-term CO_2 sequestration processes mediated by T. A hint may come from the biological realm, where marine sediments in the Southern Hemisphere show a turnover from warm- toward cool- and eutrophic-waters species since the EOT [279]. The presence of these species suggests higher nutrient supply to the oceans, potentially triggered by the intensification of the hydrological cycle and the overall increase in the riverine flux [280]. The net result would be the increase in the primary productivity mediated by photosynthetic organisms and consequent higher rates of carbonate burial at the sea bottom, process facilitated also by the post-EOT deepening of the Carbonate Compensation Depth (CCD). This is further supported by high $\delta^{13}C$ in proximity of the EOT [258]. Stronger atmospheric circulation, jointly to changes in the Asian topography through the Oligocene and Miocene have been also proposed to drive the long-term CO_2 removal via silicate weathering intensification [77]. Differently from the overall post 34 Ma trend, the CO_2 flux variability between ˜18-14 Ma suggests unrelated T mechanisms. This period, encompassing the MMCO, has been linked to strong CO_2 degassing due to the emplacement of the Columbia River Basalt Group which would cause the climate warmth [281], while following increase in ocean alkalinity due to large emplacement of evaporites across the Eastern Europe are thought to restore pre-MMCO CO_2 conditions [282] (Fig. 4.1e). Our analysis corroborates this view is by reconstructing a net, positive $\frac{dC}{dt}$ budget at ˜18 and ˜16 Ma, whereas depicting stronger CO_2 removal rates between ˜16 - 14 Ma (Fig. 4.1e). Finally, our analysis detects stable fluxes starting at the end of the MMCO ˜14 Ma, with a sharp decrease in both source and sinks since ˜8 Ma (Fig. 4.1c, d). While keeping a quasi-stable equilibrium between sources and sinks over the period (Fig. 4.1e), we cannot relate any significant, geological change to explain the reduction of both fluxes at this time.

4.5 Conclusions

Future research in deciphering climate change depends on our ability to constrain carbon fluxes in the recent and deep past to unveil underlying climate trends. In this contribution, we use a simple formulation of the geological carbon cycle to retrieve unprecedented estimates of Cenozoic surface CO_2 source and sink fluxes and timing of statistically significant CO_2 - T coupling/decoupling, directly inferred from available CO_2 proxy data. Higher variability of γ and βT before 34 Ma and the synchronicity between the decrease in CO_2 emissions and the evolution of the Neo-Tethyan margin suggest a geodynamic control on the early Cenozoic climate. Reduction in CO_2 emissions and following feedback mechanisms eventually set the conditions for a glaciated Antarctica, marking the shift from a greenhouse to an icehouse climate state. We attribute the lower variability of γ and βT and the stable CO_2 sequestration trend since 34 Ma to a T-CO_2 coupling arising from surface, T-mediated processes, involving changes in the radiative budget, and the intensification of silicate weathering. Besides the long-term cooling, abrupt events such as the PETM, EECO, and MMCO have been repeatedly considered analogues of present-day climate change [283]. Future applications of this novel algorithm shorter in time events, jointly to the increasing availability of proxy data, will provide a more precise estimation of the CO_2 flux magnitudes and their impact in a context of fast greenhouse gas emissions.

4.6 Figures

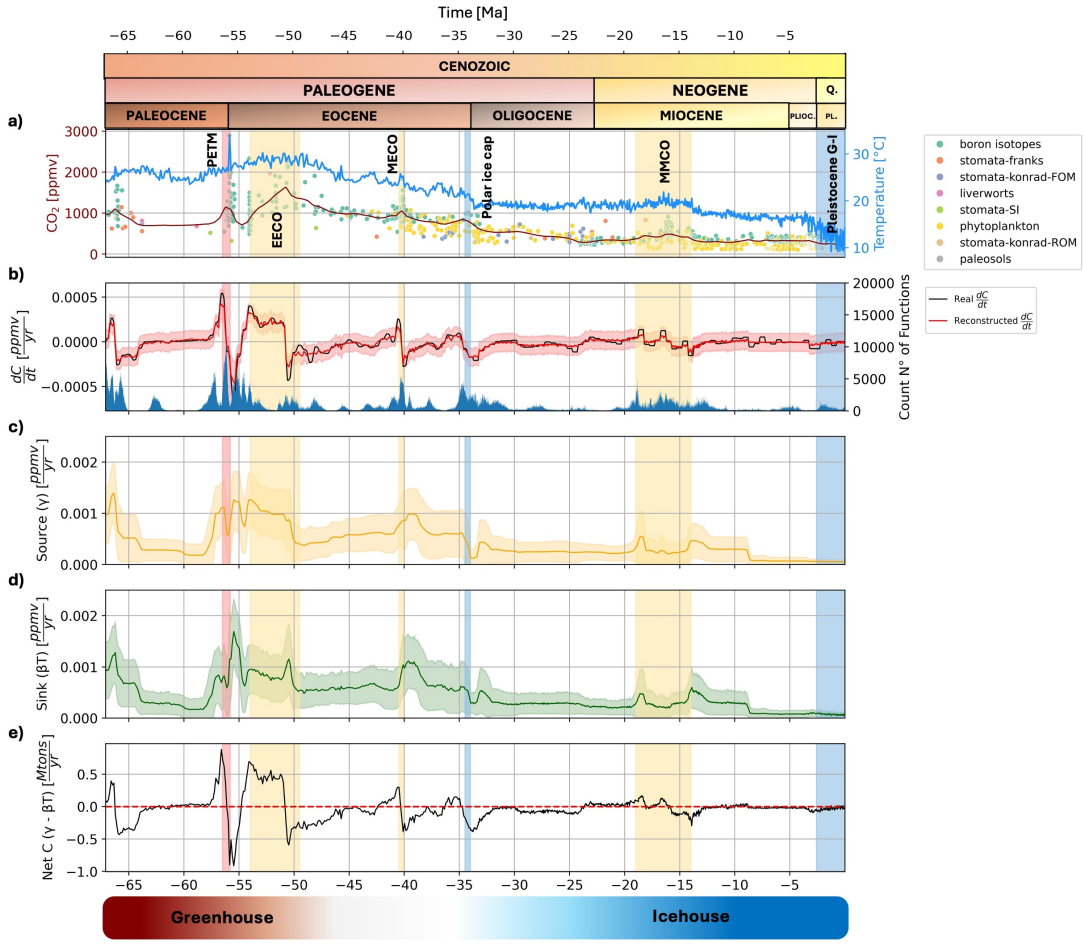

Figure 4.1: *Data compilation and inversion results. (a) Surface CO_2 trend represented by the 500-kyr smoothed curve (dark red) and multi-proxy record (scatterplot) from [249]. The overall CO_2 decreasing trend couples the Global Mean Surface Temperature (dodger blue) from [257]. (b) Central* $\frac{dC}{dt}$ *derivative (black) computed from the 500-kyrs smoothed CO_2 curve used for the inversion and its fit with the synthetic* $\frac{dC}{dt}$ *curve (red) retrieved during the inversion. The red band shows the uncertainty of the reconstructed synthetic* $\frac{dC}{dt}$ *curve. (c) γ flux time history retrieved. (d) βT flux time history retrieved. (e) Net budget between source and sink fluxes converted in* $\frac{MtonsC}{yr}$.

Chapter 5

Conclusions

Human-driven climate change raises questions about future scenarios and effective strategies to mitigate its impact on both human and ecological communities. Given this, proxy contained in paleoclimate archives have been increasingly used to reconstruct past climate conditions, offering the unique chance to learn from the past. The understanding of how climate evolves under highly-perturbing conditions is thus pivotal to inform future trajectories and adjust climate policies accordingly.

In Chapter 1 I outlined how the Earth System, formally including the atmosphere, hydrosphere, cryosphere, biosphere, and geosphere is constantly subject to mutual interactions, enhanced in turn by climate forcings. These forcings arise from radiative unbalances driven by changes in solar incident radiation, surface albedo and greenhouse gas concentrations. In this work, I focused on the impact that changes in the surface carbon dioxide (CO_2) can have on climate by considering its coupled relation with temperature (T) trends throughout the geological past. Surface CO_2 exchanges occur on timescales from days to tens of thousands of years, while interactions with the deep Earth involve much longer timescales, governed by geological processes such as volcanic emissions and silicate weathering. CO_2 and T trends draw different trajectories depending on the time scale considered. In this work, I considered two time periods: the late Pleistocene, characterized by the alternation of long, cool glacial and short, warm interglacial periods, and the Cenozoic era, encompassing the last ˜66 Myrs, during which both CO_2 and T show a stable declining trend.

However, though proxy-derived reconstructions of paleo-CO_2 trends provide absolute estimates,

they tell little about underlying temporal changes, that is the temporal evolution of CO_2 sources and sinks. In Chapter 2, I discussed how past attempts to model paleo-CO_2 fluxes relied on the use of subjectively chosen inputs for numerical models and ignored the strong relation between T and such fluxes. This contribution fills the gap in the subject by providing a novel way to think at the CO_2 flux quantification problem. For this purpose, I implemented an inversion algorithm based on a reversible-jump Markov chain Monte Carlo technique (rj-McMC) and coupled it with a simple definition of the geological carbon cycle to data-infer timing of past source and sink flux changes. In Section 2.4, I described the methodology and validated it through different synthetic tests. I then applied the algorithm to real-world data by inverting the temporal derivative of atmospheric CO_2 ($\frac{dC}{dt}$) derived from the Antarctic Dome Fuji record, covering the last ˜340 kyrs. The results reveal a clear decoupling between $\frac{dC}{dt}$ - T during deglaciations, suggesting that CO_2 changes were not directly driven by T trends. On the contrary, strong coupling during glacial periods reveals a primary role of orbital parameters to glacial inceptions.

In Chapter 3, I presented my second work which extends the analysis back to the last ˜800 kyrs by inverting the temporal derivative of atmospheric CO_2 of the longest available ice core record of Dome C. Remarkably, we find a strong agreement between the inversions on Dome C and Fuji ice cores for the most recent glacial-interglacial cycles. Also, we detect a shift in the flux regime prior to ˜400 ka, during which CO_2 fluxes stabilize coupling T trends. This suggests a stronger influence of orbital parameters in carbon cycling for older glacial-interglacial cycles. The shift, further supported by supplementary tests, points out to disruptions inherited since the onset of the the Mid-Brunhes Transition (MBT) ˜430 ka. In the study, we investigate causative mechanisms of this shift using both qualitative and quantitative approaches, such as lead-lag functions and wavelet coherence analysis. Far to provide a conclusive response, we hypothesize two scenarios involving enhanced solid Earth degassing along Mid Ocean Ridges (MORs), likely triggered by wider sea-level excursions since ˜400 ka.

In Chapter 4, I introduced my last, ongoing work, focused on the inversion of the Cenozoic $\frac{dC}{dt}$ signal derived from a recent, multi-proxy CO_2 compilation. Results suggest higher flux variability before ˜34 Ma, which we interpret as due to sustained volcanic CO_2 emissions in the context of Neo-Tethys closure. The extinction of the arc reduces the amount of CO_2 injected into the atmosphere, thus providing the conditions for the onset of an Antarctic ice cap. Since the polar ice cap is established, we find stronger $\frac{dC}{dt}$ - T coupling which we ascribe to intensified albedo feedbacks

occurring since ˜34 Ma. The warm phase of the Middle Miocene Climatic Optimum (MMCO) and its aftermath represents an exception to this coupling, potentially linked to the emplacement of Columbia River Basalt Group in North America. However, given the preliminary interpretation of this work, further tests and analysis, including the comparison with previous works are needed.

In conclusion, while this PhD project addresses several key aspects of paleo-CO_2 flux reconstruction, it also opens a number of important questions. For example: What are the limitations of the current inversion algorithm in terms of time? Could incorporating a more complex forward model improve its resolution and understanding of different contributing mechanisms to source and sink CO_2 flux changes? How could the investigations be extended to different proxy records? During the project, I began to explore some of these questions through new collaborations. However, due to their preliminary nature, these efforts could not be included in the present thesis. Finally, the hope is that this work lays the foundation for future research and inspires a multi-disciplinary approach to assess the contribution of geological processes into the Earth's Climate System.

Chapter 6

Appendix

During the PhD, I was involved as a co-author in works not specifically related to the project. At the moment, some of these remain unpublished but others, as the one I decided to include in this appendix, represent part of the effort I put along these three years. The work presented in the following section, currently in peer-review for *Global and Planetary Change*, extends the analysis far beyond the Cenozoic, encompassing the last ˜540 Myrs of Earth's history. This Eon is called Phanerozoic, and begins with the first large spreading of living organisms. During this time, geological processes related to supercontinent assembly cycles are the dominant mechanisms through which climate conditions evolve. In this contribution, we make use of statistical tools to link global long-term surface temperatures with different geodynamics occurring along plate boundaries, thus exploring climate variations of this Eon.

Geodynamic pacemaker of Phanerozoic climate: A Multivariate Analysis of Plate Boundary Processes and Global Temperature Variations

Andrea Di Giulio[1], Pietro Sternai[2,3], Roberto Sacchi[1], Luca Castrogiovanni[2]

[1]Department of Earth and Environmental Sciences, University of Pavia, Via Ferrata 1, 27100 Pavia, Italy.

[2]Department of Earth and Environmental Sciences, University of Milano-Bicocca, Italy.

[3]GFZ, German Research Centre for Geosciences, Potsdam, Germany.

Status: peer-review for *Global and Planetary Change*

Abstract

Global long-term surface temperature variations throughout the Phanerozoic are related to changes in concentrations of carbon compounds in the atmosphere, but the deeper the time, the more uncertain becomes the information about carbon budgets and fluxes preserved in geological archives. Although some temporal correlations between climate changes and individual geodynamic processes have been recognized, a comprehensive understanding of the relationships between long-term changes in Global Average Temperature and the ensemble of geodynamic climate-forcing mechanisms throughout the Phanerozoic Eon is elusive. Here, building upon literature data, we perform a simple cross-correlation multivariate analyses to investigate relationships between Phanerozoic Global Average Temperature and different geodynamics occurring along plate boundaries. Our analysis suggests that Earth's climate operates as a multi-driver system, with no single dominant mechanism identifiable throughout the Phanerozoic. In addition, cooling and heating geodynamic processes require different timescales to fully exert their effects on global temperature. These outcomes highlight the necessity of integrative approaches that consider multiple processes to explain the paleoclimate evolution of the Earth. Within this broader framework, the cycles of supercontinent assembly and breakup are key in modulating the relative development of cooling and heating plate margins over geologic timescales, effectively serving as the primary pacemaker of Global Average Temperature variations.

6.1 Introduction

The oxygen isotope record of marine sediments and other paleo-climate indicators (e.g., paleo-soils, coal, reefs, ice-rafting sediments) document long-term changes in Earth's Global Average Temperature (GAT) (Fig.6.1; e.g., [284] and references therein). These global temperature trends affect the planet habitability and evolution of life and are commonly ascribed to a limited number of geological processes acting mostly at plate boundaries (e.g., magmatic degassing along volcanic arcs, spreading ridges and riftings, erosion and weathering of silicate minerals along suture zones) (e.g., [252]; [285]; [286]; [287]; [40]; [229]). These processes and plate boundary types have often been considered individually and their effects on global climate were evaluated based on the changes in the surface concentration of CO_2 they are expected to produce (e.g., [46]; [288]; [289]; [268]; [290]; [291]; [93]; [287]; [48]). However, consensus about the dominant driver(s) of long-term temperature change is lacking to date. Because a complex balance between several climate-impacting geodynamic processes is likely to determine long-term global temperature changes (e.g., [292]; [293]; [294]) (Fig.6.1), an integrative approach seems necessary. Here, we first provide a concise and non-exhaustive overview of current knowledge of the Phanerozoic atmospheric GAT, its potential geodynamic drivers and related debated questions. We do not intend to provide a complete review, but simply a general background for our analyses. We then evaluate cross-correlations between GAT trends throughout the Phanerozoic (based on [284]) and available time series of global geodynamics at plate margins based on kinematic reconstructions ([295]; [93]; [287];[296]; [297]. The rationale of this approach is that a correlation or anticorrelation between GAT and different types of plate margin dynamics may support (or not) the role of each geodynamic process in driving global temperature changes (as heater or cooler). We also analyse and discuss the lag time of significant cross-correlations and assess the possible role played by the supercontinent cycles [298], [299] in controlling the balance between cooler and heater plate margins throughout the Phanerozoic.

6.2 Geodynamic drivers of phanerozoic global temperature: a short overview

6.2.1 Global Temperature trends: models and proxies

Long-term trends of GAT depend on the concentration of greenhouse gasses (GHG) in the atmosphere, particularly carbon dioxide and subordinately methane [300], [292], [301], [302], [249], [11]). Several biogeochemical Earth system box models have been designed to quantify the long-term carbon cycle (e.g., [303] , [304] [95],[5], [252], [300]; [305]) and provide model-based reconstructions of paleoclimate also for time intervals when data are either unavailable or uncertain [306], [307], [308],[309], [310], [311], [253], [312], [6]. GEOCARBSULF [304], [5] and COPSE [253] and their subsequent versions (GEOCARBSULF.rev and COPSE.rev, Fig.6.1A-B; [313]) are amongst the most commonly used. However, changes in temperature or surface pCO_2 from these models are often difficult to reconcile with results retrieved from paleoclimate proxies. For instance, Mesozoic atmospheric CO_2 reconstructions from GEOCARBSULF models generally underpredict the proxy-based global temperature record, and neither model captures the apparent Paleogene maximum in pCO_2. This marked mismatch between modelled pCO_2 and GAT is particularly concerning for Cenozoic when geological archives are better preserved (e.g., [10], [314], [301], [308], [310], [313], [122]).

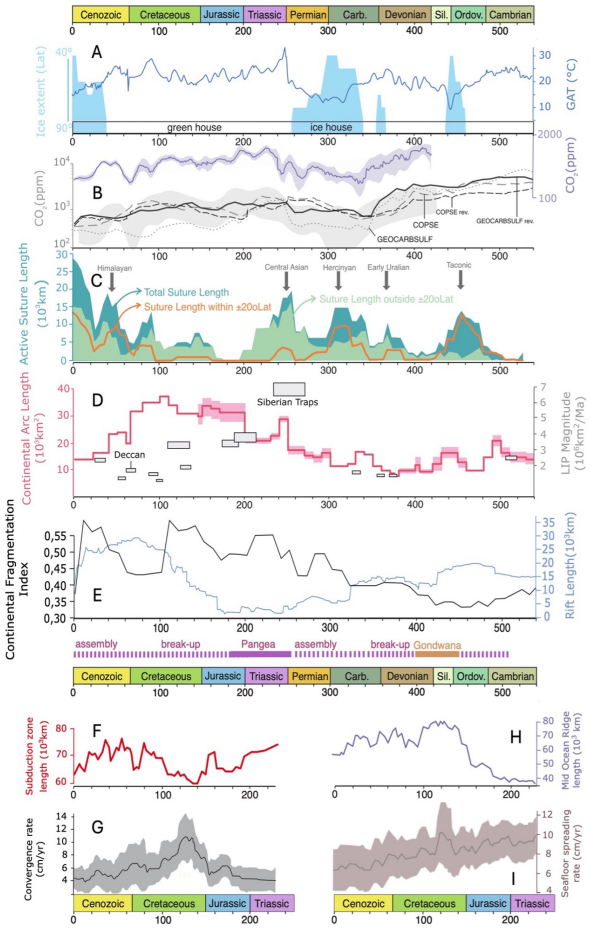

Figure 6.1: *Available Global Average Temperature (GAT) estimate and CO_2 concentration predicted by both GEOCARBSULF and COPSE alongside time histories of possible geodynamic drivers (resampled every 5 My, for cross-comparison). Datasets are reported in the Supplementary Material SM1). A) Global Average Temperature (GAT) estimate from [284]. Latitudinal extent of continental ice sheet, excluding Alpine glaciers, from [315] and [316]. B) Estimates of atmospheric CO_2 content from long-term carbon cycle modelling; Atmospheric pCO_2 (with error windows shaded) from [310], COPSE [253], and GEOCARBSULF [308], COPSErev. and GEOCARBSULFrev. after [305]; the light grey area shows the CO_2 estimates and average error bar [305]. C) Active suture length (total and within the high weathering zone) from [287] and active suture length outside the high weathering zone recalculated in the present work according to data in[287]. D) Continental Arc Length [295] and Large Igneous Provinces (LIPs) (box size representing the relative volume of emission) [284]. E) Rifting Length [296], Continental fragmentation index [299] and phases of continental assembly and break-up [298]. Seafloor spreading rate and mid oceanic ridge length from* **??**. *F-G) Length of Subduction zones and Convergence rate [297]. H-I) Length of spreading ridges and sea-floor spreading rate [297]*

6.2.2 Oceanic ridges and spreading rate

Degassing along oceanic spreading ridges is considered as a major source of GHG from the mantle to the ocean-atmosphere system (e.g., [95], [252], [317]). Attempts to quantify this contribution to surface temperature changes are based on estimates of both the global average spreading rate and the total length of spreading ridges through time for the last 220 Ma [318], [319], [93], [305], [297], [320], [321]). This approach assumes larger GHG outfluxes associated with faster-spreading rates ([322], [290] and references therein) (Fig.6.1H-I). [318] and [323] assume a roughly constant half-spreading rate of 2.6 cm/yr for the last 150 Ma, whereas [93] account for a long-term decline of seafloor half-spreading rates from 4 cm/yr to 2.5 cm/yr, during the same time window. Regarding ridge length,[93] propose an increase from 40'000 km to 80'000 km during Jurassic due to the breakup of the supercontinent Pangea, followed by a decrease to 60'000-70'000 km until the present-day. Total ridge length estimates during Pangea formation and fragmentation suggest a progressive decline from about 60'000 to about 40'000 km ([317] and references therein). Before the Triassic, data supporting ridge length reconstructions are highly speculative and several scenarios can be inferred [321]. On a global scale, longer and faster-spreading mid-ocean ridges during the (early) Cretaceous [324] match high surface temperatures recorded by GAT, whereas declining length and spreading rate during the Cenozoic are consistent with progressive climate cooling (Fig.6.1A). However, although mid-ocean ridges were shorter and slower during the Triassic and Jurassic, the GAT was comparable to - or even higher than – that of the Cretaceous, and both the strong increase in ridge length at the Jurassic-Cretaceous transition and the peak in the sea-floor spreading rate during the Middle Miocene do not have a recognizable counterpart in the GAT curve.

6.2.3 Continental magmatic arcs and subduction zones

Continental magmatic arcs are thought to release higher volumes of GHG into the atmosphere compared to oceanic ridges or arcs developed along intraoceanic subduction zones (e.g., [325]). C-enrichment may be related to the recycling of subducted carbon as well as interaction between upwelling magmas and upper plate crustal rocks [326], [327], [288], [328], [329], [268], [48].[268] used frequency histograms of detrital zircon $\frac{U}{Pb}$ ages to estimate continental volcanic arc effect on climate over the last 2.4 billion years. The authors interpret the correlation between higher frequency of detrital zircon $\frac{U}{Pb}$ ages and CO_2 emissions during greenhouse periods as an indica-

tion of the dominant driving role of continental-arc volcanism in long-term temperature changes, but the reliability of this approach is a matter of debate (e.g., [330]). [295] combined kinematic reconstructions and present-day surface area of felsic to intermediate plutonic rocks, considered to be the roots of ancient continental volcanic arcs, to support that magmatism along subduction zones plays a primary role in driving long-term temperature changes based on correlating estimated arc size/activity and greenhouse/icehouse conditions (Fig.6.1D). However, CO_2 model-proxy mismatches remain [329]. An overall decrease of the GAT from the early Triassic to the middle Cretaceous is at odds with a progressive increase in global continental arc length. Furthermore, it can be observed that the Ordovician glaciation occurred during a period of relatively high length of continental arcs. The information about the length of subduction zones becomes more robust since the Triassic [93] (Fig.6.1F). A slowly decreasing subduction zone length is observed throughout the Triassic and Jurassic, with a minimum during the early Cretaceous followed by an increase in the late Cretaceous and early Cenozoic and a new decrease during the late Cenozoic. This overall trend fits the gross features of the GAT curve during Mesozoic-Cenozoic.

6.2.4 Suture zone length

Special emphasis has been given to the role of mountain building along collisional margins in driving long-term cooling trends (e.g., [78], [289], [287], [331], [48]). Concurrent climate-driving processes along collisional margins are the waning of CO_2 emissions from continental magmatic arcs, and atmospheric CO_2 drawdown by exposure of silicate minerals to chemical weathering during mountain uplift and erosion. According to Macdonald et al. (2019), an increase in the global length of active suture zones within the tropical zone (±20° latitude, where most chemical weathering occurs nowadays), commonly precedes the beginning of glaciations by 10 Ma, which is suggested to be the lag time for the Earth climate system to switch from a greenhouse to an icehouse state. Conversely, greenhouse periods occur when global active sutures length is lower and/or mostly outside the tropical zone, like during the Triassic and the Cretaceous Central Asian and Laramide orogenic cycles (Fig.6.1C). However, identifying the extent of tropical zone in deep time is difficult (e.g., compare [287] with [329]) and similar lengths of suture zones within the 20° latitude belt in the latest Devonian, Triassic and Late Cretaceous correspond to icehouse conditions in the Paleozoic, but greenhouse conditions in the Mesozoic (Fig.6.1A and C).

6.2.5 Continental Rifts Length

The contribution of continental rifting to atmospheric CO_2 concentrations via volcanic degassing is difficult to assess. Emissions from rift magmatism are poorly constrained even in the present-day, and are supposedly highly variable in space and time due to, for instance, variable amounts of decompression melting and amounts of carbon within subcontinental mantle [332], [302], [333]. It is even harder to assess the evolution of surface CO_2 sink due to erosion and weathering of silicate minerals exposed along rift shoulders [334], [335]. Despite this high uncertainty, relationships between rift magmatism and climate trend have been proposed in the Cenozoic (e.g.,[336]) and an overall fit between rift length (Fig.6.1E) and CO_2 content in the atmosphere reconstructed through GEOCARBSULF modelling (Fig.6.1B) has been suggested for the last 200 Ma [290], possibly indicating a link between phases of supercontinent break-up and high global temperatures due to increasing rift lengths (e.g., [333]) (Fig.6.1E).

6.2.6 Large Igneous Provinces

Large Igneous Provinces (LIPs) involve emplacement in short time (< 5 Myrs) of large volumes of mafic magmatic products (frequently $> 10^6\ km^3$; Fig.6.1D) coming from mantle plumes (see [291] and [337] for a review). The role of LIPs as climate drivers during the Phanerozoic and Precambrian is debated and commonly thought to be related to two opposite effects: GHG emission via direct degassing and warming of C-rich cover rocks (evaporites, carbonates, coal) during LIPs emplacement, and silicate weathering of exposed mafic igneous rocks and associated atmospheric CO_2 removal soon after emplacement. The first effect depends mainly on the geochemistry of magmas and the type of volcanic activity [291], while the latter is proportional to climatic conditions, latitude, erosion rates, and areal extent of the volcanic products emplaced [96], [338]. Given the relatively short duration of these events, their effect on global temperatures on $> 10^7$ year timescales is questionable (e.g., [268], [290], [339]). This is confirmed by the Phanerozoic stratigraphic records, where LIPs do not seem to correlate with global warming nor cooling and several LIPs developed in the high weathering climate belt at low latitude ($\pm 20° - 30°$ latitude) during greenhouse periods (Kharindij, Central Atlantic and Deccan LPIs), without evident cooling effects. With our approach based on the cross correlation of continuous time series we cannot investigate the possible effect of LIPs on global temperature trends. However, LIPs remain possible triggers mostly of short-lived

anomalous climatic aberrations like hyperthermal events [340], [341], which are out of the goals of this paper.

6.3 Methods

We analysed the cross-correlation between the time series of GAT by [284], and the potential geodynamic drivers listed above (Fig.6.1). We do not consider neither short-term cyclicity of solar activity, nor possible effect of long-term solar cycles on Earth dynamics (e.g. [342], [343]), as we aimed to test the possible role of geodynamic processes on global T variations. Given these premises, we followed the procedure schematically summarized in Fig.**??** 2. We compiled available time series for major geodynamic processes occurring at plate margins and potentially affecting global climate (Table**??** 1), resampling each time series at a 5 Ma interval, and normalising curves between 0-1 values to make them readily comparable between one another. Cross-correlations only consider lags that assume leading (i.e., predicting) effects of geodynamic drivers on the GAT. The background assumption in our analysis is that the considered time series can capture the most significant trends and variations of the analysed parameters over the time span considered within the limit of 5 Ma time bins used. Based on the range of retrieved correlation coefficients, we arbitrarily chose ± 0.15 as the threshold between significant and not significant correlation. We also included in our analysis the time series of the Continental Fragmentation Index proposed by [299] in order to investigate if continents assembly and fragmentation (i.e., the Supercontinent Cycle) modulates the evolution of climate-driving plate margins. Results in terms of cross-correlation coefficients (CCF) are summarized in Table**??** 1. All the statistical analyses were performed in R (ver. 3.6, R Core Team 2022) and correlations were obtained using the CCF function available in the base package.

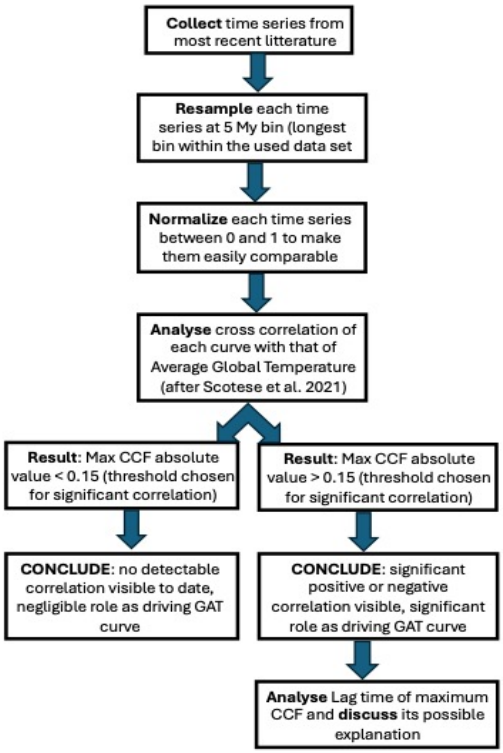

.

Figure 6.2: *Flow chart summarizing the analytical approach used for detecting cross correlations between Global Average Temperature curve (GAT after [284]) and different geodynamic climate drivers.*

6.4 Results

6.4.1 Cross-Correlation Functions between GAT and convergent plate margins dynamics

Subduction related arc-trench systems and convergence rate

We find a clear positive correlation between GAT and both continental arc and subduction zone length (Fig.6.3A and B). Positive correlations with GAT results for lags 0-3 (i.e., within 15 My)

	Driver	CCF at lag 0	Max CCF	Higher CCF lag time	Time interval	Reference
Convergent settings	Continental arc length	0.359	0.389	2 (10 My)	Phanerozoic	Cao et al., 2017 ([295])
	Subduction zones length	0.291	0.304	2 (10 My)	Late Triassic–present day	Müller et al., 2019 ([297])
	Average Convergence Rate	-0.013	-0.191	4 (20 My)	Late Triassic–present day	Müller et al., 2019 ([297])
	Total Active suture length	-0.251	-0.251	0 (5 My)	Phanerozoic	Macdonald et al., 2019 ([287])
	Active suture length within 20° lat	-0.535	-0.535	0 (5 My)	Phanerozoic	Macdonald et al., 2019 ([287])
	Active suture length out of 20° lat	0.101	0.126	1 (5 My)	Phanerozoic	Macdonald et al., 2021 ([287])
Divergent settings	Ocean ridge length	-0.146	-0.250	5 (20 My)	Late Triassic–present day	Müller & Dutkiewicz, 2018 ([93])
	Average Spreading Rate	0.300	0.300	0 (5 My)	Late Triassic–present day	Müller & Dutkiewicz, 2018 ([93])
	Rifting length	0.127	0.127	0 (5 My)	Phanerozoic	Merdith et al., 2019 ([296])
	Continental fragmentation index	0.072	0.257	5 (25 My)	Phanerozoic	Zaffos et al., 2017 ([299])

Table I: *Synthesis of the results of cross-correlation analysis between GAT curve (after [284]) and considered geodynamic processes. On the right, the references for the considered time series are reported. Highest CCF lag time column reports the lag time in terms of 5 My bins corresponding to the maximum obtained correlation coefficient within a 25 My time span.*

with a maximum value at Lag 2 (0.38 for continental arc length and 0.30 for subduction zone length; Table I). This strongly supports the idea that volcanic arcs along convergent plate margins play a primary role in promoting the increase of atmospheric GHG, but the lag time before maximum correlation coefficient suggests that arcs produced delayed climatic effects. Conversely, the curve of global average convergence rate correlates very weakly with the GAT (0.19 at lag 4; Table I and Fig.6.3C) suggesting that it plays a minor role in controlling the amount of GHG emission along volcanic arcs in subduction zones.

Suture zones

The length of suture zones along collisional plate margins are anticorrelated with GAT at lag 0. Anticorrelation is moderate (e.g., -0.25; Fig.6.3D) if all suture zones are considered, but it increases when only suture zones within ±20° paleolatitude are considered (-0.53) and becomes insignificant when suture zones outside ±20° paleolatitude are considered (-0.10 and -0.12 at lag 0; Fig.6.3E-F). This result confirms that silicate weathering along collisional belts plays a primary role as atmospheric carbon sink (e.g., [287]).

6.4.2 Cross Correlation Functions between GAT and divergent plate margins dynamics

Oceanic ridges and spreading rate

Overall, ocean ridge length does not correlate with GAT, with only a relatively weak and delayed negative correlation occurring at lag 4 (-0.25; Fig.6.3G and Table I1). By contrast, a significant positive correlation is observed between GAT and average spreading rate (0.30; Fig.6.3H) at lag 0. This suggests that the amount of GHG emitted from oceanic spreading ridges depends on the spreading rate, rather than on ridge length.

Rifts and Continental Fragmentation Index

Rift length and GAT show limited correlation throughout the Phanerozoic, with the highest cross-correlation of 0.12 at Lag 0 (Fig.6.3I, TableI). The global scale development of different types of plate margins is intrinsically linked to the cycles of aggregation and fragmentation of continental masses (i.e., the supercontinent cycles), which was proposed to have a role in driving long term GAT (e.g., [298], [299], [344], [345] , [346]). Our analysis finds positive correlation of around 0.25 between the fragmentation index and the GAT starting from lag 5 (i.e., around 25 My; Fig.6.3J and Table

I). This result suggests that continental rifting must evolve into drifting throughout continental fragmentation to drive global climatic effects, and that collision zones must reach a threshold length before having an impact on global temperature during phases of continental aggregation.

.

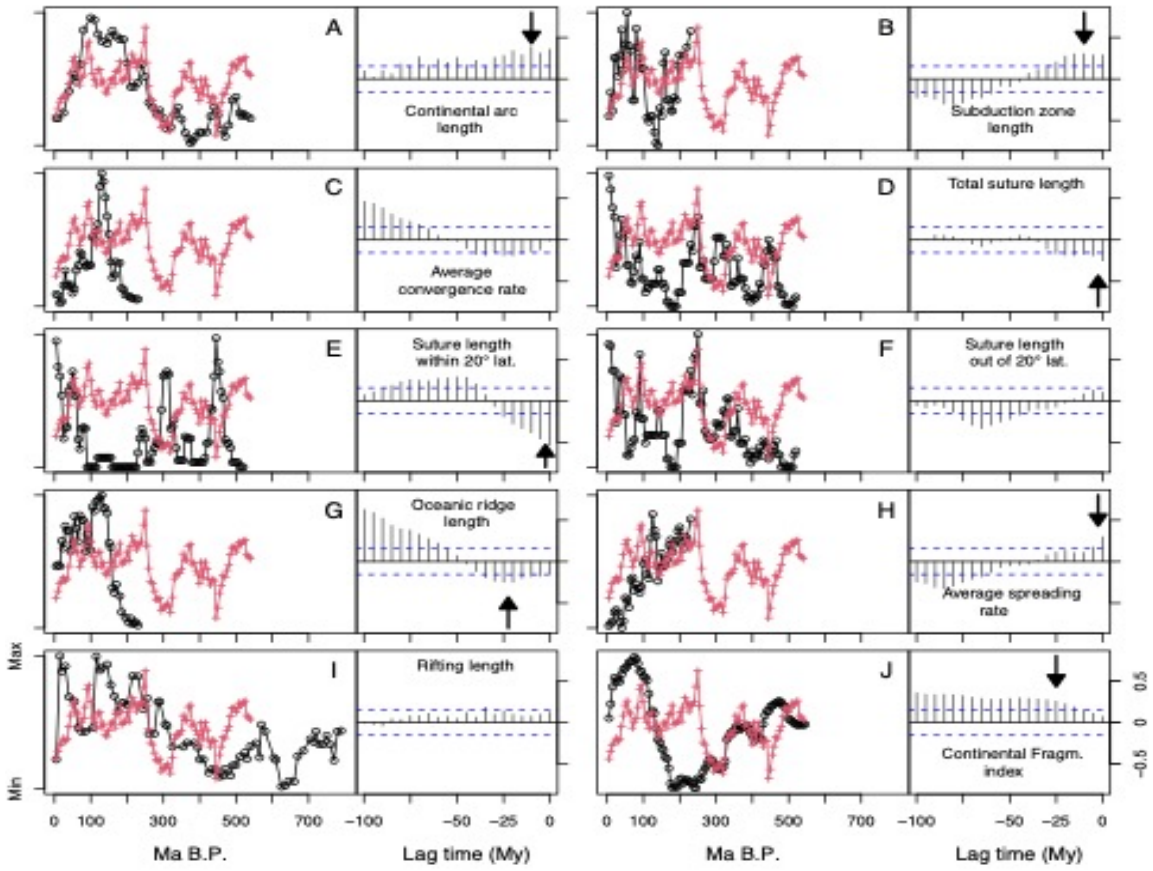

Figure 6.3: *Diagrams showing time curves and the cross-correlation factor (CCF) between Global Average Temperature (GAT, after [284]) and analysed geodynamic drivers. For each driver, the normalized curves are shown on the left and the cross-correlation values on the right; arrows refer to best CCF within a 5 Lag (25 My) time span (values reported in Tab.I and datasets reported in the Supplementary Material SM1); blue dashed lines refer to the 0,15 absolute value of CCF taken as threshold for significant correlation. Time series: A) Continental Arc length after [295]; B) subduction zones length after [93]; C) Convergence rate after [297]; D) Total suture length after [287]; E) length of sutures within 20° latitude high weathering belt after [287]; F) length of sutures out of the 20° latitude high weathering belt present work based on data from [287]; G) Spreading ridge length after [93]; H) Seafloor spreading rate [287]; I) Rifting length after [296]; J) Continental fragmentation Index after [299].*

6.5 Discussion

Our analysis suggests that GAT variations cannot be ascribed to a single driver but result from an ever-changing interplay between heating (GHG source) and cooling (GHG sinks) plate margins releasing, acting across timescales (Table I1, Fig.6.4). Different GAT trends during periods characterized by similar climate drivers indicate that the climate system responds differently depending on the overall boundary conditions (i.e., the ensemble state of all climate-impacting mechanisms). Within this broad picture, the Paleozoic geologic record is the most uncertain, with the most unsteady climate, marked by two major icehouse periods (Late Ordovician and Permo-Carboniferous ice ages) and a minor Silurian-Devonian glaciation interleaved by warm intervals ([284] and references therein). Three major orogenic events (Taconic, Early Uralian, and Hercynian orogeneses) and biological revolutions (e.g., the rise and evolution of vascular plants on the continents) occurred during this time [347], [348]. The unsteadiness of climate is possibly due to the concomitant fast-evolving biosphere and the assemblage of the Gondwana supercontinent near the South Pole [349]. It must be noted that our investigation focuses solely on the possible effect of geodynamic processes on global temperature, without accounting for the potential contribution of the biosphere.

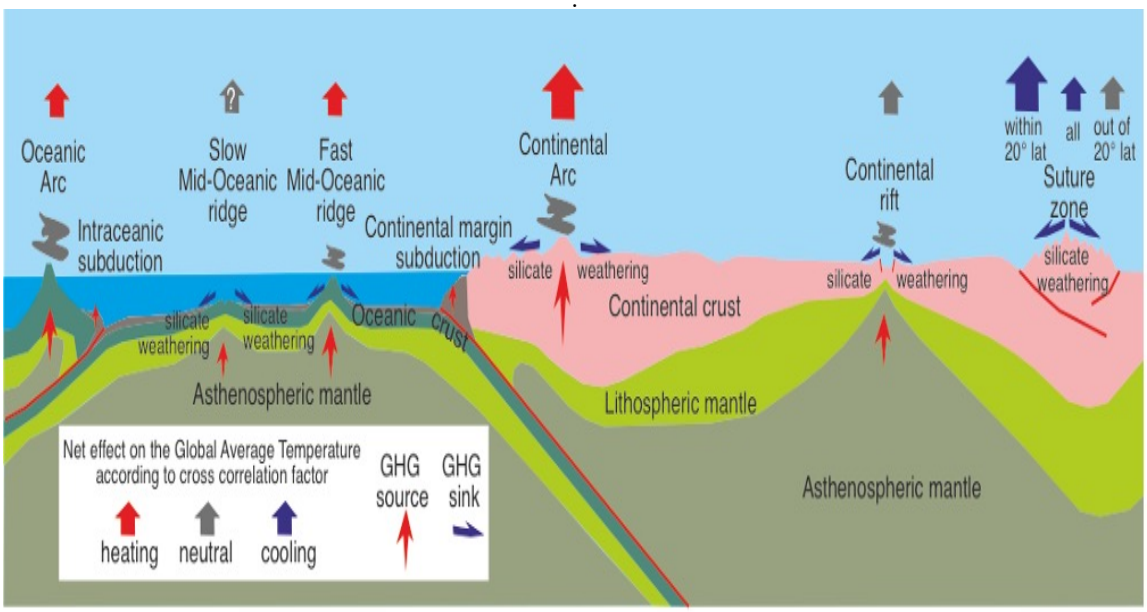

Figure 6.4: *Cartoon (not to scale) showing the effect on Global Average Temperature (GAT) of different geodynamic settings according to the statistical cross correlation analysis. Inspired to the figure of [293]. Colour of arrows indicates the type of correlation (red positive, i.e. heating effect; blue negative, i.e. cooling effect; grey not significant correlation, i.e. undetectable effect), dimension of arrows is proportional to the obtained CCF value of each analysed driver with the Global Average Temperature curve during Phanerozoic proposed by [284].*

Our approach does not account for the impact of geologically short-term events, such as the emplacement of Large Igneous Provinces (LIPs), on global temperature trends. For example, paleogeographic reconstructions [284] (Fig.6.5) place Pangea near its maximum extent at the end of the Permian (252 Ma), when the Siberian Traps erupted. At that time, Gondwana spanned the South Pole while Siberia lay at high latitudes. As a result, this LIP was emplaced in a cold, high-latitude setting, where reduced silicate weathering likely followed its emplacement. In contrast, the Deccan Traps (66 Ma) erupted on the rapidly northward-drifting Indian plate, which was then located in tropical latitudes under greenhouse conditions. In this case, enhanced silicate weathering probably amplified the climatic disruption associated with the end-Cretaceous. Earlier, during the Permo-Carboniferous Ice Age (360–285 Ma), Gondwana lay across the South Pole and was covered by continental ice sheets extending over southern Africa, South America, Antarctica, India, and Australia, while equatorial Laurasia supported extensive coal swamps. Going further back, the Silurian–Devonian glaciation did not produce a full Snowball Earth, but Gondwana was situated at

high southern latitudes, whereas Laurentia and Baltica remained in equatorial, reef-bearing belts. Despite the large uncertainties, the observed correlations between icehouse periods and the extent of suture belts, as well as between continental arc length and greenhouse intervals, suggest that geodynamics exerted a primary control on global climate evolution during the Paleozoic. Since the Late Triassic, the geological record has become more complete and robust, including data on oceanic ridge lengths and their average spreading rate, as well as the average convergence rate along subduction zones. Additionally, the biosphere became more stable. The positive correlation of both continental arc length and subduction zone length with GAT at lags 0-3 (i.e., within 15 My), with the maximum value at lag 2 (Table I), coincides with the expected time required by a subduction zone and its volcanic arc to fully develop (e.g., [350]). The correlation between continental arcs and GAT (0.38) higher than between subduction length and GAT (0.30) suggests that intra-oceanic arcs contribute less to carbon emissions into the atmosphere. The average convergence rate does not correlate significantly with GAT, suggesting that convergence rate does not exert a primary control on degassing from volcanic arcs related to subduction zones and continental arcs.

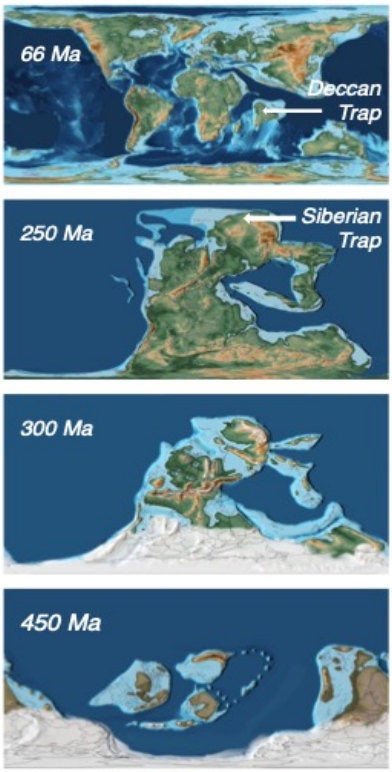

.

Figure 6.5: *Paleogeographic reconstructions after [284] for some turning points of the global temperature curve (see text for further details and discussion).*

Suture belts developed along collisional margins emerge from our analysis as the most efficient geodynamic coolers of global temperature when collisions occur within the inter-tropical high weathering zone; this is consistent with previous findings by [287]. The fact that the maximum anticorrelation is observed already at lag 0 supports the idea that CO_2 sequestration via subaerial silicate weathering of volcanic rocks along exposed arcs develops rapidly, within a time span of less than 5 My. Nevertheless, future research should take into account changes in the latitudinal extent of the high weathering tropical zone, as significant shifts can be reasonably expected during icehouse and greenhouse periods. The correlation between the length of oceanic spreading ridges and GAT is not significant, but there is a strong positive correlation between global average spreading

rate and GAT. The lack of positive correlation with ridge length suggests that greenhouse gases emitted along oceanic ridges may not reach the ocean-atmosphere system; this could be possibly due to massive oceanic rock carbonation [351]. Conversely, the positive correlation between GAT and the average spreading rate may indicate that fast-spreading ridges, generally associated with strong positive mantle thermal anomalies, enhance to atmospheric CO_2 concentrations through a combination of increased degassing and reduced water column buffering due to higher ridge relief. However, their effects on global sea-level and, thus, on climate remain largely elusive [352], and the relative contribution of fast- versus slow-spreading ridges to the GAT should be assessed in the future. Results regarding continental rifting are surprising in that their length does not correlate significantly with GAT. The discrepancy with the conclusion by e.g., [333] may be due to the intrinsic transient nature of rifts systems, which may transition to drifting and oceanic spreading ridges over a relatively short geological time (around 10-20 Ma, e.g., [353]). Also, concomitant silicate weathering of volcanic rocks along rifting volcanic margins, especially if they develop in the high weathering zone, may buffer correlations with the GAT. Linking latitude of continental rifts to our analysis (similarly to what Macdonald et al., 2019, did for suture belts) could further constrain such possible buffering effect of silicate weathering along rifting zones.

Finally, the significant cross-correlation between GAT and the continental fragmentation index, reaching its maximum value at lag 4, i.e., after 20 Ma, suggests that continent fragmentation and aggregation cycles act as the background pacemaker of global temperature. 15-20 Ma is also the time required for heating margins to fully develop - e.g., for subduction zones to fully develop volcanic arcs and for rifting to evolve into oceanic spreading ridges - during supercontinent fragmentation. By contrast, during supercontinent assembly, the cooling effect of suture zones is faster, occurring within the 5 Ma bin used in our analysis. Since the exhumation of silicate-bearing minerals within metamorphic core complexes, whose weathering enhances atmospheric CO_2 drawdown, likely takes up to a few tens of Ma, we speculate that the dominant cooling mechanism of continental suture zones is the waning of CO_2 emissions from pre-collisional volcanic arcs.

6.6 Conclusions

We investigate the potential role of major geodynamic processes along plate margins in driving long-term temperature changes on Earth. This is achieved by systematically comparing their trends with

the Global Average Temperature (GAT) curve throughout the entire Phanerozoic or since the Triassic, depending on data availability. Our analysis suggests that: (1) cooling and heating geodynamic processes require different timescales to fully exert their effects on global temperature, and Earth's climate operates as a multi-driver system without a single dominant mechanism. These results highlight the necessity of integrative approaches that consider multiple processes to explain the paleoclimate evolution of the Earth. (2) The most effective type of plate margin in promoting climate warming ("heating margins") are continental volcanic arcs. To a lesser extent, oceanic spreading ridges also contribute to warming, with average global spreading rate, rather than total length, driving the positive correlation with GAT. In contrast, the contribution of rifting zones appears to be negligible at least with the 5 Ma time bin used in this study. (3) Collisional suture belts located in the high-weathering equatorial zone play a significant role in sequestering greenhouse gases and cooling the atmosphere ("cooling margins"). While this result confirms what previously recognized by [287], supercontinent assembly and breakup cycles play a fundamental role in regulating the balance between cooling and heating plate margins over geologic timescales, ultimately acting as the primary driver of Global Average Temperature fluctuations. Further research is needed to fully understand the relationships between global climate trends and geodynamic processes, and better constraints regarding surface carbon capture and sourcing processes along slow- and fast-spreading ridges and the role played by continental riftings also accounting for their latitude are particularly needed.

6.7 Acknowledgments

Chiara Amadori and Sebastian Castelltort are kindly acknowledged for their contribution to data collection (CA) and discussions (CA and SC) during a very preliminary stage of this research. For this research, ADG has been supported by Italian "Progetto Nazionale di Ricerca in Antartide" (PNRA), project "The response of the sedimentary system through Permian to Jurassic abrupt climatic and provenance changes in Northern Victoria Land" (CUP $B53C19015810001$). PS thanks for support the Fondazione Cariplo and Fondazione CDP (grant $n°.2022-1546\_001$), the Alexander von Humboldt Foundation (research project CEMENT), the project Dipartimenti di Eccellenza 2023–2027, TECLA, funded by the Italian Ministry of Education, Universities and Research (MUR), and the ERC project MATRICs (project number: 101167761). The Editors of this Special Issue

are acknowledged for invited us to present this contribution.

Bibliography

1. Lee, H. *et al. Climate change 2023: synthesis report. Contribution of working groups I, II and III to the sixth assessment report of the intergovernmental panel on climate change* (2023).
2. Longman, R. J. *et al.* Compilation of climate data from heterogeneous networks across the Hawaiian Islands. *Scientific data* **5,** 1–17 (2018).
3. Cubasch, U. *et al.* in *Climate Change 2001: The scientific basis. Contribution of WG1 to the Third Assessment Report of the IPCC (TAR)* 525–582 (Cambridge University Press, 2001).
4. Schmalensee, R., Stoker, T. M. & Judson, R. A. World carbon dioxide emissions: 1950–2050. *Review of Economics and Statistics* **80,** 15–27 (1998).
5. Berner, R. A. GEOCARBSULF: a combined model for Phanerozoic atmospheric O2 and CO2. *Geochimica et Cosmochimica Acta* **70,** 5653–5664 (2006).
6. Mills, B. J., Donnadieu, Y. & Goddéris, Y. Spatial continuous integration of Phanerozoic global biogeochemistry and climate. *Gondwana Research* **100,** 73–86 (2021).
7. Fairbridge, R. W. & Gornitz, V. in *Encyclopedia of Paleoclimatology and Ancient Environments* 428–438 (Springer, 2009).
8. Bereiter, B. *et al.* Revision of the EPICA Dome C CO2 record from 800 to 600 kyr before present. *Geophysical Research Letters* **42,** 542–549 (2015).
9. Jouzel, J. *et al.* Orbital and millennial Antarctic climate variability over the past 800,000 years. *science* **317,** 793–796 (2007).
10. Zachos, J., Pagani, M., Sloan, L., Thomas, E. & Billups, K. Trends, rhythms, and aberrations in global climate 65 Ma to present. *science* **292,** 686–693 (2001).

11. Judd, E. J. *et al.* A 485-million-year history of Earth's surface temperature. *Science* **385,** eadk3705 (2024).

12. IPCC. in *Climate Change 2023: Synthesis Report. Contribution of Working Groups I, II and III to the Sixth Assessment Report of the Intergovernmental Panel on Climate Change* (eds Team, C. W., Lee, H. & Romero, J.) Edited by Reisinger, A., D. Cammarano, A. Fischlin, J.S. Fuglestvedt, G. Hansen, Y. Jung, C. Ludden, V. Masson-Delmotte, R. Matthews, J.B.K. Mintenbeck, D.J. Orendain, A. Pirani, E. Poloczanska, and J. Romero, 119–130 (IPCC, Geneva, Switzerland, 2023).

13. Lenton, T. *Earth system science: a very short introduction* (Oxford University Press, 2016).

14. Fan, J. *et al.* Statistical physics approaches to the complex Earth system. *Physics reports* **896,** 1–84 (2021).

15. Schmittner, A., Brook, E. J. & Ahn, J. Impact of the ocean's overturning circulation on atmospheric CO2 (2007).

16. Martínez-García, A. *et al.* Iron fertilization of the Subantarctic Ocean during the last ice age. *Science* **343,** 1347–1350 (2014).

17. Jiang, H.-B. *et al.* Natural ocean iron fertilization and climate variability over geological periods. *Global Change Biology* **29,** 6856–6866 (2023).

18. Takahashi, T. *et al.* Climatological mean and decadal change in surface ocean pCO2, and net sea–air CO2 flux over the global oceans. *Deep Sea Research Part II: Topical Studies in Oceanography* **56,** 554–577 (2009).

19. Ford, D. J. *et al.* Enhanced ocean CO2 uptake due to near-surface temperature gradients. *Nature Geoscience* **17,** 1135–1140 (2024).

20. Berner, R. A. *et al.* A new look at the long-term carbon cycle. *Gsa Today* **9,** 1–6 (1999).

21. Huybers, P. & Langmuir, C. Feedback between deglaciation, volcanism, and atmospheric CO2. *Earth and Planetary Science Letters* **286,** 479–491 (2009).

22. Luterbacher, J. & Pfister, C. The year without a summer. *Nature Geoscience* **8,** 246–248 (2015).

23. DeVries, T. The ocean carbon cycle. *Annual Review of Environment and Resources* **47,** 317–341 (2022).

24. Broecker, W. S. The great ocean conveyor. *Global warming: physics and facts* **247,** 129–161 (1992).

25. Menviel, L. & Spence, P. Southern Ocean circulation's impact on atmospheric CO2 concentration. *Frontiers in Marine Science* **10,** 1328534 (2024).

26. De La Rocha, C. L. & Passow, U. The biological pump. *Treatise on Geochemistry, Second Edition, vol. 8* **8,** 93–122 (2014).

27. Bickert, T. in *Encyclopedia of paleoclimatology and ancient environments* 136–138 (Springer, 2009).

28. Crowley, J. W., Katz, R. F., Huybers, P., Langmuir, C. H. & Park, S.-H. Glacial cycles drive variations in the production of oceanic crust. *Science* **347,** 1237–1240 (2015).

29. Lear, C. H., Elderfield, H. & Wilson, P. A. Cenozoic deep-sea temperatures and global ice volumes from Mg/Ca in benthic foraminiferal calcite. *science* **287,** 269–272 (2000).

30. Crowell, J. C. & Frakes, L. A. Phanerozoic glaciation and the causes of ice ages. *American Journal of Science* **268,** 193–224 (1970).

31. Toggweiler, J. & Bjornsson, H. Drake Passage and palaeoclimate. *Journal of Quaternary Science: Published for the Quaternary Research Association* **15,** 319–328 (2000).

32. Ikeda, T. & Tajika, E. A study of the energy balance climate model with CO2-dependent outgoing radiation: Implication for the glaciation during the Cenozoic. *Geophysical Research Letters* **26,** 349–352 (1999).

33. Bennett, M. M. & Glasser, N. F. *Glacial geology: ice sheets and landforms* (John Wiley & Sons, 2011).

34. Jiang, D., Tian, Z., Lang, X., Kageyama, M. & Ramstein, G. The concept of global monsoon applied to the last glacial maximum: A multi-model analysis. *Quaternary Science Reviews* **126,** 126–139 (2015).

35. Tzedakis, P. Vegetation change through glacial—interglacial cycles: a long pollen sequence perspective. *Philosophical Transactions of the Royal Society of London. Series B: Biological Sciences* **345,** 403–432 (1994).

36. Dusenge, M. E., Duarte, A. G. & Way, D. A. Plant carbon metabolism and climate change: elevated CO 2 and temperature impacts on photosynthesis, photorespiration and respiration. *New Phytologist* **221,** 32–49 (2019).

37. Zhang, X. *et al.* Review of Land Surface Albedo: Variance Characteristics, Climate Effect and Management Strategy. *Remote Sensing* **14.** ISSN: 2072-4292. `https://www.mdpi.com/2072-4292/14/6/1382` (2022).

38. Martin, J. H. Glacial-interglacial CO2 change: The iron hypothesis. *Paleoceanography* **5,** 1–13 (1990).

39. Cowling, S., Jones, C. & Cox, P. Consequences of the evolution of C4 photosynthesis for surface energy and water exchange. *Journal of Geophysical Research: Biogeosciences* **112** (2007).

40. Cloetingh, S. *et al.* Coupled surface to deep Earth processes: Perspectives from TOPO-EUROPE with an emphasis on climate-and energy-related societal challenges. *Global and Planetary Change* **226,** 104140 (2023).

41. McCormick, M. P., Thomason, L. W. & Trepte, C. R. Atmospheric effects of the Mt Pinatubo eruption. *Nature* **373,** 399–404 (1995).

42. Hall, K. Rapid deglaciation as an initiator of volcanic activity: an hypothesis. *Earth Surface Processes and Landforms* **7,** 45–51 (1982).

43. Kutterolf, S., Schindlbeck, J. C., Jegen, M., Freundt, A. & Straub, S. M. Milankovitch frequencies in tephra records at volcanic arcs: The relation of kyr-scale cyclic variations in volcanism to global climate changes. *Quaternary Science Reviews* **204,** 1–16 (2019).

44. Schindlbeck, J. C. *et al.* One Million Years tephra record at IODP S ites U 1436 and U 1437: I nsights into explosive volcanism from the J apan and I zu arcs. *Island Arc* **27,** e12244 (2018).

45. Slater, L., Jull, M., McKenzie, D. & Gronvöld, K. Deglaciation effects on mantle melting under Iceland: results from the northern volcanic zone. *Earth and Planetary Science Letters* **164,** 151–164 (1998).

46. Ganino, C. & Arndt, N. T. Climate changes caused by degassing of sediments during the emplacement of large igneous provinces. *Geology* **37,** 323–326 (2009).

47. Jones, S. M., Hoggett, M., Greene, S. E. & Dunkley Jones, T. Large Igneous Province thermogenic greenhouse gas flux could have initiated Paleocene-Eocene Thermal Maximum climate change. *Nature Communications* **10,** 5547 (2019).

48. Sternai, P. *et al.* Magmatic forcing of Cenozoic climate? *Journal of Geophysical Research: Solid Earth* **125,** e2018JB016460 (2020).

49. Lodolo, E. & Tassone, A. A. Gateways and climate: the Drake Passage opening (2010).

50. Spicer, R. A., Farnsworth, A. & Su, T. Cenozoic topography, monsoons and biodiversity conservation within the Tibetan Region: An evolving story. *Plant Diversity* **42,** 229–254 (2020).

51. Mitchell, J., Manabe, S., Meleshko, V. & Tokioka, T. Equilibrium climate change and its implications for the future. *Climate change: The IPCC scientific assessment* **131,** 172 (1990).

52. Matthews, J. R. *et al.* Annex VII-Glossary 3. *Notes* **29,** 30 (2021).

53. in. *Cloud-Resolving Modeling of Convective Processes* 157–183 (Springer Netherlands, Dordrecht, 2008). ISBN: 978-1-4020-8276-4. https://doi.org/10.1007/978-1-4020-8276-4_11.

54. Lenton, T. M. *et al.* A method to identify positive tipping points to accelerate low-carbon transitions and actions to trigger them. *Sustainability Science,* 1–20 (2025).

55. Satoh, M. in *Atmospheric Circulation Dynamics and General Circulation Models* 353–369 (Springer, 2013).

56. Ribas, I. The Sun and stars as the primary energy input in planetary atmospheres. *Proceedings of the International Astronomical Union* **5,** 3–18 (2009).

57. Hays, J. D., Imbrie, J. & Shackleton, N. J. Variations in the Earth's Orbit: Pacemaker of the Ice Ages: For 500,000 years, major climatic changes have followed variations in obliquity and precession. *science* **194,** 1121–1132 (1976).

58. Imbrie, J. A theoretical framework for the Pleistocene ice ages: William Smith Lecture. *Journal of the Geological Society* **142,** 417–432 (1985).

59. Wunsch, C. Quantitative estimate of the Milankovitch-forced contribution to observed Quaternary climate change. *Quaternary Science Reviews* **23,** 1001–1012 (2004).

60. Raymo, M. The initiation of Northern Hemisphere glaciation. *Annual Review Of Earth And Planetary Sciences, Volume 22, pp. 353-383.* **22,** 353–383 (1994).

61. Hogg, A. M. Glacial cycles and carbon dioxide: A conceptual model. *Geophysical research letters* **35** (2008).

62. Stephens, G. L. *et al.* The albedo of Earth. *Reviews of geophysics* **53,** 141–163 (2015).

63. Donohoe, A. & Battisti, D. S. Atmospheric and surface contributions to planetary albedo. *Journal of Climate* **24,** 4402–4418 (2011).

64. Alessandri, A., Catalano, F., De Felice, M., Van den Hurk, B. & Balsamo, G. Varying snow and vegetation signatures of surface-albedo feedback on the Northern Hemisphere land warming. *Environmental Research Letters* **16,** 034023 (2021).

65. Webb, E., Loranty, M. & Lichstein, J. Surface water, vegetation, and fire as drivers of the terrestrial Arctic-boreal albedo feedback. *Environmental Research Letters* **16,** 084046 (2021).

66. Jackson, R. D. & Idso, S. B. Surface albedo and desertification. *Science* **189,** 1012–1013 (1975).

67. Yin, Q. Insolation-induced mid-Brunhes transition in Southern Ocean ventilation and deep-ocean temperature. *Nature* **494,** 222–225 (2013).

68. McGehee, R. & Lehman, C. A paleoclimate model of ice-albedo feedback forced by variations in Earth's orbit. *SIAM Journal on Applied Dynamical Systems* **11,** 684–707 (2012).

69. Schrag, D. P., Berner, R. A., Hoffman, P. F. & Halverson, G. P. On the initiation of a snowball Earth. *Geochemistry, Geophysics, Geosystems* **3,** 1–21 (2002).

70. Budyko, M. I. The effect of solar radiation variations on the climate of the Earth. *tellus* **21,** 611–619 (1969).

71. Arrhenius, S. XXXI. On the influence of carbonic acid in the air upon the temperature of the ground. *The London, Edinburgh, and Dublin Philosophical Magazine and Journal of Science* **41,** 237–276 (1896).

72. Tschumi, T., Joos, F., Gehlen, M. & Heinze, C. Deep ocean ventilation, carbon isotopes, marine sedimentation and the deglacial CO 2 rise. *Climate of the Past* **7,** 771–800 (2011).

73. Ai, X. E. *et al.* Southern Ocean upwelling, Earth's obliquity, and glacial-interglacial atmospheric CO2 change. *Science* **370,** 1348–1352 (2020).

74. Moosdorf, N., Renforth, P. & Hartmann, J. Carbon dioxide efficiency of terrestrial enhanced weathering. *Environmental science & technology* **48,** 4809–4816 (2014).

75. Sundquist, E. T. Geological perspectives on carbon dioxide and the carbon cycle. *The carbon cycle and atmospheric CO2: Natural variations Archean to present* **32,** 55–59 (1985).

76. Berner, R. A. & Lasaga, A. C. Modeling the geochemical carbon cycle. *Scientific American* **260,** 74–81 (1989).

77. Penman, D. E., Rugenstein, J. K. C., Ibarra, D. E. & Winnick, M. J. Silicate weathering as a feedback and forcing in Earth's climate and carbon cycle. *Earth-Science Reviews* **209,** 103298 (2020).

78. Raymo, M. E. & Ruddiman, W. F. Tectonic forcing of late Cenozoic climate. *nature* **359,** 117–122 (1992).

79. Lisiecki, L. E. & Raymo, M. E. A Pliocene-Pleistocene stack of 57 globally distributed benthic δ18O records. *Paleoceanography* **20** (2005).

80. Herbert, T. D. The mid-Pleistocene climate transition. *Annual Review of Earth and Planetary Sciences* **51,** 389–418 (2023).

81. Skinner, L. C., Fallon, S., Waelbroeck, C., Michel, E. & Barker, S. Ventilation of the deep Southern Ocean and deglacial CO2 rise. *Science* **328,** 1147–1151 (2010).

82. Toggweiler, J. R., Russell, J. L. & Carson, S. R. Midlatitude westerlies, atmospheric CO2, and climate change during the ice ages. *Paleoceanography* **21** (2006).

83. Schädel, C. *et al.* Circumpolar assessment of permafrost C quality and its vulnerability over time using long-term incubation data. *Global change biology* **20,** 641–652 (2014).

84. Joos, F., Gerber, S., Prentice, I., Otto-Bliesner, B. L. & Valdes, P. J. Transient simulations of Holocene atmospheric carbon dioxide and terrestrial carbon since the Last Glacial Maximum. *Global biogeochemical cycles* **18** (2004).

85. Brovkin, V., Ganopolski, A., Archer, D. & Rahmstorf, S. Lowering of glacial atmospheric CO2 in response to changes in oceanic circulation and marine biogeochemistry. *Paleoceanography* **22** (2007).

86. DeConto, R. M. & Pollard, D. Rapid Cenozoic glaciation of Antarctica induced by declining atmospheric CO2. *nature* **421,** 245–249 (2003).

87. Stickley, C. E. *et al.* Timing and nature of the deepening of the Tasmanian Gateway. *Paleoceanography* **19** (2004).

88. Giorgioni, M. *et al.* Carbon cycle instability and orbital forcing during the Middle Eocene Climatic Optimum. *Scientific Reports* **9,** 9357 (2019).

89. Zeebe, R. E. What caused the long duration of the Paleocene-Eocene Thermal Maximum? *Paleoceanography* **28,** 440–452 (2013).

90. Frieling, J. *et al.* Thermogenic methane release as a cause for the long duration of the PETM. *Proceedings of the National Academy of Sciences* **113,** 12059–12064 (2016).

91. Van Der Boon, A. *et al.* Exploring a link between the Middle Eocene Climatic Optimum and Neotethys continental arc flare-up. *Climate of the Past Discussions* **2020,** 1–15 (2020).

92. Wong, K. *et al.* Deep carbon cycling over the past 200 million years: a review of fluxes in different tectonic settings. *Frontiers in Earth Science* **7,** 263 (2019).

93. Müller, R. D. & Dutkiewicz, A. Oceanic crustal carbon cycle drives 26-million-year atmospheric carbon dioxide periodicities. *Science Advances* **4,** eaaq0500 (2018).

94. Lefebvre, V., Donnadieu, Y., Goddéris, Y., Fluteau, F. & Hubert-Théou, L. Was the Antarctic glaciation delayed by a high degassing rate during the early Cenozoic? *Earth and Planetary Science Letters* **371,** 203–211 (2013).

95. Berner, R. A. GEOCARB II: A revised model of atmospheric CO [sub 2] over phanerozoic time. *American Journal of Science;(United States)* **294** (1994).

96. Goddéris, Y., Donnadieu, Y., Le Hir, G., Lefebvre, V. & Nardin, E. The role of palaeogeography in the Phanerozoic history of atmospheric CO2 and climate. *Earth-Science Reviews* **128,** 122–138 (2014).

97. Ichii, K. *et al.* New data-driven estimation of terrestrial CO2 fluxes in Asia using a standardized database of eddy covariance measurements, remote sensing data, and support vector regression. *Journal of Geophysical Research: Biogeosciences* **122,** 767–795 (2017).

98. Mueller, K. L., Yadav, V., Curtis, P. S., Vogel, C. & Michalak, A. M. Attributing the variability of eddy-covariance CO2 flux measurements across temporal scales using geostatistical regression for a mixed northern hardwood forest. *Global Biogeochemical Cycles* **24** (2010).

99. Chalk, T. B. *et al.* Causes of ice age intensification across the Mid-Pleistocene Transition. *Proceedings of the National Academy of Sciences* **114,** 13114–13119 (2017).

100. Li, G., Ji, J., Chen, J. & Kemp, D. B. Evolution of the Cenozoic carbon cycle: The roles of tectonics and CO2 fertilization. *Global Biogeochemical Cycles* **23** (2009).

101. Malinverno, A. Parsimonious Bayesian Markov chain Monte Carlo inversion in a nonlinear geophysical problem. *Geophysical Journal International* **151,** 675–688 (2002).

102. Agostinetti, N. P. & Malinverno, A. Receiver function inversion by trans-dimensional Monte Carlo sampling. *Geophysical Journal International* **181,** 858–872 (2010).

103. Zhdanov, M. S. *Inverse theory and applications in geophysics* (Elsevier, 2015).

104. Hadamard, J. Sur les problèmes aux dérivées partielles et leur signification physique. *Princeton university bulletin,* 49–52 (1902).

105. Hjelt, S.-E. *Pragmatic inversion of geophysical data* (Springer, 1992).

106. Backus, G. & Gilbert, F. Uniqueness in the inversion of inaccurate gross earth data. *Philosophical Transactions of the Royal Society of London. Series A, Mathematical and Physical Sciences* **266,** 123–192 (1970).

107. Mueller, J. L. & Siltanen, S. *Linear and nonlinear inverse problems with practical applications* (SIAM, 2012).

108. Shan, Y., Gong, F., Li, Z. & Lin, G. A grid-search inversion method looking for the best classification of polyphase fault/slip data. *Tectonophysics* **433,** 53–64 (2007).

109. Mosegaard, K. & Tarantola, A. in *International Geophysics* 237–265 (Elsevier, 2002).

110. Green, P. J. Reversible jump Markov chain Monte Carlo computation and Bayesian model determination. *Biometrika* **82,** 711–732 (1995).

111. Sambridge, M. & Mosegaard, K. Monte Carlo methods in geophysical inverse problems. *Reviews of Geophysics* **40,** 3–1 (2002).

112. Gill, P. E., Murray, W. & Wright, M. H. *Practical optimization* (SIAM, 2019).

113. Bellman, R., Kalaba, R. E., *et al. Dynamic programming and modern control theory* (Citeseer, 1965).

114. Metropolis, N., Rosenbluth, A. W., Rosenbluth, M. N., Teller, A. H. & Teller, E. Equation of state calculations by fast computing machines. *The journal of chemical physics* **21,** 1087–1092 (1953).

115. Tierney, L. & Mira, A. Some adaptive Monte Carlo methods for Bayesian inference. *Statistics in medicine* **18,** 2507–2515 (1999).

116. Mosegaard, K. & Tarantola, A. Monte Carlo sampling of solutions to inverse problems. *Journal of Geophysical Research: Solid Earth* **100,** 12431–12447 (1995).

117. Smith, A. F. & Roberts, G. O. Bayesian computation via the Gibbs sampler and related Markov chain Monte Carlo methods. *Journal of the Royal Statistical Society: Series B (Methodological)* **55,** 3–23 (1993).

118. Zondervan, J. R. *et al.* Rock organic carbon oxidation CO2 release offsets silicate weathering sink. *Nature* **623,** 329–333 (2023).

119. Torres, M. A., West, A. J. & Li, G. Sulphide oxidation and carbonate dissolution as a source of CO2 over geological timescales. *nature* **507,** 346–349 (2014).

120. Rogger, J. *et al.* Biogeographic climate sensitivity controls Earth system response to large igneous province carbon degassing. *Science* **385,** 661–666 (2024).

121. Maffre, P., Swanson-Hysell, N. L. & Goddéris, Y. Limited carbon cycle response to increased sulfide weathering due to oxygen feedback. *Geophysical Research Letters* **48,** e2021GL094589 (2021).

122. Castrogiovanni, L., Sternai, P., Agostinetti, N. P. & Pasquero, C. A reversible-jump Markov chain Monte Carlo algorithm to estimate paleo surface CO2 fluxes linking temperature to atmospheric CO2 concentration time series. *Computers & Geosciences* **196,** 105838 (2025).

123. Kerr, R. A. A North Atlantic climate pacemaker for the centuries. *Science* **288,** 1984–1985 (2000).

124. Pagani, M., Zachos, J. C., Freeman, K. H., Tipple, B. & Bohaty, S. Marked decline in atmospheric carbon dioxide concentrations during the Paleogene. *science* **309,** 600–603 (2005).

125. Parker, D. *et al.* Decadal to multidecadal variability and the climate change background. *Journal of Geophysical Research: Atmospheres* **112** (2007).

126. Zachos, J. C., Dickens, G. R. & Zeebe, R. E. An early Cenozoic perspective on greenhouse warming and carbon-cycle dynamics. *nature* **451,** 279–283 (2008).

127. Berger, A. Milankovitch theory and climate. *Reviews of geophysics* **26,** 624–657 (1988).

128. Berger, A., Loutre, M.-F. & Tricot, C. Insolation and Earth's orbital periods. *Journal of Geophysical Research: Atmospheres* **98,** 10341–10362 (1993).

129. Weertman, J. Milankovitch solar radiation variations and ice age ice sheet sizes. *Nature* **261,** 17–20 (1976).

130. Berger, A. Astronomical theory of paleoclimates and the last glacial-interglacial cycle. *Quaternary Science Reviews* **11,** 571–581 (1992).

131. Middelburg, J. J., Soetaert, K. & Hagens, M. Ocean alkalinity, buffering and biogeochemical processes. *Reviews of Geophysics* **58,** e2019RG000681 (2020).

132. Aiuppa, A. *et al.* Volcanic CO2 seep geochemistry and use in understanding ocean acidification. *Biogeochemistry* **152,** 93–115 (2021).

133. Kohfeld, K. E. & Ridgwell, A. Glacial-interglacial variability in atmospheric CO2. *Surface ocean-lower atmosphere processes* **187,** 251–286 (2009).

134. Williams, R. G., Katavouta, A. & Goodwin, P. Carbon-cycle feedbacks operating in the climate system. *Current Climate Change Reports* **5,** 282–295 (2019).

135. Neftel, A., Oeschger, H., Schwander, J., Stauffer, B. & Zumbrunn, R. Ice core sample measurements give atmospheric CO2 content during the past 40,000 yr. *Nature* **295,** 220–223 (1982).

136. Delmas, R. J. Environmental information from ice cores. *Reviews of Geophysics* **30,** 1–21 (1992).

137. Basak, C. *et al.* Breakup of last glacial deep stratification in the South Pacific. *Science* **359,** 900–904 (2018).

138. Galbraith, E. D. & Skinner, L. C. The biological pump during the Last Glacial Maximum. *Annual Review of Marine Science* **12,** 559–586 (2020).

139. Ganopolski, A. & Brovkin, V. Simulation of climate, ice sheets and CO 2 evolution during the last four glacial cycles with an Earth system model of intermediate complexity. *Climate of the Past* **13,** 1695–1716 (2017).

140. Kawamura, K. *et al.* Atmospheric CO2 variations over the last three glacial'interglacial climatic cycles deduced from the Dome Fuji deep ice core, Antarctica using a wet extraction technique. *Tellus B: Chemical and Physical Meteorology* **55,** 126–137 (2003).

141. Masson-Delmotte, V. *et al.* Past temperature reconstructions from deep ice cores: relevance for future climate change. *Climate of the Past* **2,** 145–165 (2006).

142. Lüthi, D. *et al.* High-resolution carbon dioxide concentration record 650,000–800,000 years before present. *nature* **453,** 379–382 (2008).

143. Uemura, R. *et al.* Ranges of moisture-source temperature estimated from Antarctic ice cores stable isotope records over glacial–interglacial cycles. *Climate of the Past* **8,** 1109–1125 (2012).

144. Ludwig, W., Amiotte-Suchet, P., Munhoven, G. & Probst, J.-L. Atmospheric CO2 consumption by continental erosion: present-day controls and implications for the last glacial maximum. *Global and planetary change* **16,** 107–120 (1998).

145. Gloor, M. *et al.* A first estimate of present and preindustrial air-sea CO2 flux patterns based on ocean interior carbon measurements and models. *Geophysical Research Letters* **30,** 10–1 (2003).

146. Rial, J. A. *et al.* Nonlinearities, feedbacks and critical thresholds within the Earth's climate system. *Climatic change* **65,** 11–38 (2004).

147. Schneider, S. H. Abrupt non-linear climate change, irreversibility and surprise. *Global Environmental Change* **14,** 245–258 (2004).

148. Hartley, M. E., Maclennan, J., Edmonds, M. & Thordarson, T. Reconstructing the deep CO2 degassing behaviour of large basaltic fissure eruptions. *Earth and Planetary Science Letters* **393,** 120–131 (2014).

149. Frery, E. *et al.* Geochemical transect through a travertine mount: A detailed record of CO2-enriched fluid leakage from Late Pleistocene to present-day–Little Grand Wash fault (Utah, USA). *Quaternary International* **437,** 98–106 (2017).

150. Mancini, A. *et al.* Evaluating the geogenic CO2 flux from geothermal areas by analysing quaternary travertine masses. New data from western central Italy and review of previous CO2 flux data. *Quaternary Science Reviews* **215,** 132–143 (2019).

151. Zurek, J., Moune, S., Williams-Jones, G., Vigouroux, N. & Gauthier, P.-J. Melt inclusion evidence for long term steady-state volcanism at Las Sierras-Masaya volcano, Nicaragua. *Journal of Volcanology and Geothermal Research* **378,** 16–28 (2019).

152. Caves, J. K., Jost, A. B., Lau, K. V. & Maher, K. Cenozoic carbon cycle imbalances and a variable weathering feedback. *Earth and Planetary Science Letters* **450,** 152–163 (2016).

153. Soulet, G. *et al.* Temperature control on CO2 emissions from the weathering of sedimentary rocks. *Nature Geoscience* **14,** 665–671 (2021).

154. Bufe, A., Rugenstein, J. K. & Hovius, N. CO2 drawdown from weathering is maximized at moderate erosion rates. *Science* **383,** 1075–1080 (2024).

155. Olson, J. *et al.* The natural carbon cycle. *Atmospheric carbon dioxide and the global carbon cycle* **239,** 175–214 (1985).

156. Uemura, R. *et al.* Asynchrony between Antarctic temperature and CO2 associated with obliquity over the past 720,000 years. *Nature communications* **9,** 961 (2018).

157. Berner, W., Oeschger, H. & Stauffer, B. Information on the CO2 cycle from ice core studies. *Radiocarbon* **22,** 227–235 (1980).

158. Craig, H. Standard for reporting concentrations of deuterium and oxygen-18 in natural waters. *Science* **133,** 1833–1834 (1961).

159. Dansgaard, W. Stable isotopes in precipitation. *tellus* **16,** 436–468 (1964).

160. Mandolesi, E., Ogaya, X., Campanyà, J. & Agostinetti, N. P. A reversible-jump Markov chain Monte Carlo algorithm for 1D inversion of magnetotelluric data. *Computers & Geosciences* **113,** 94–105 (2018).

161. Gallagher, K., Charvin, K., Nielsen, S., Sambridge, M. & Stephenson, J. Markov chain Monte Carlo (MCMC) sampling methods to determine optimal models, model resolution and model choice for Earth Science problems. *Marine and Petroleum Geology* **26,** 525–535 (2009).

162. Hopcroft, P. O., Gallagher, K., Pain, C. C. & Fang, F. Three-dimensional simulation and inversion of borehole temperatures for reconstructing past climate in complex settings. *Journal of Geophysical Research: Earth Surface* **114** (2009).

163. Piana Agostinetti, N., Giacomuzzi, G. & Malinverno, A. Local three-dimensional earthquake tomography by trans-dimensional Monte Carlo sampling. *Geophysical Journal International* **201,** 1598–1617 (2015).

164. Piana Agostinetti, N. & Bodin, T. Flexible coupling in joint inversions: A Bayesian structure decoupling algorithm. *Journal of Geophysical Research: Solid Earth* **123,** 8798–8826 (2018).

165. Poggiali, G., Chiaraluce, L., Di Stefano, R. & Piana Agostinetti, N. Change-point analysis of VP/VS ratio time-series using a trans-dimensional McMC algorithm: applied to the Alto Tiberina Near Fault Observatory seismic network (Northern Apennines, Italy). *Geophysical Journal International* **217,** 1217–1231 (2019).

166. Malinverno, A. & Parker, R. L. Two ways to quantify uncertainty in geophysical inverse problems. *Geophysics* **71,** W15–W27 (2006).

167. Malinverno, A. & Briggs, V. A. Expanded uncertainty quantification in inverse problems: Hierarchical Bayes and empirical Bayes. *Geophysics* **69,** 1005–1016 (2004).

168. Walker, J. C., Hays, P. & Kasting, J. F. A negative feedback mechanism for the long-term stabilization of Earth's surface temperature. *Journal of Geophysical Research: Oceans* **86,** 9776–9782 (1981).

169. Raymo, M. E., Ruddiman, W. F. & Froelich, P. N. Influence of late Cenozoic mountain building on ocean geochemical cycles. *Geology* **16,** 649–653 (1988).

170. Berner, R. A. & Caldeira, K. The need for mass balance and feedback in the geochemical carbon cycle. *Geology* **25,** 955–956 (1997).

171. Bodin, T., Salmon, M., Kennett, B. & Sambridge, M. Probabilistic surface reconstruction from multiple data sets: An example for the Australian Moho. *Journal of Geophysical Research: Solid Earth* **117** (2012).

172. Zhao, Y., Guo, Z. & Wang, Y. Asthenospheric Flow From East Asia to the Philippine Sea Plate Revealed by Rj-MCMC Inversion of Surface Waves. *Geochemistry, Geophysics, Geosystems* **23,** e2022GC010342 (2022).

173. Hopcroft, P. O. & Gallagher, K. Global variability in multi-century ground warming inferred from geothermal data. *Geophysical Research Letters* **50,** e2023GL104631 (2023).

174. Cox, A. A. & Keller, C. B. A Bayesian inversion for emissions and export productivity across the end-Cretaceous boundary. *Science* **381,** 1446–1451 (2023).

175. Lasaga, A. C. & Berner, R. A. Fundamental aspects of quantitative models for geochemical cycles. *Chemical Geology* **145,** 161–175 (1998).

176. Li, H. *et al. Research on overfitting of deep learning* in *2019 15th international conference on computational intelligence and security (CIS)* (2019), 78–81.

177. Zhou, Z.-H. Open-environment machine learning. *National Science Review* **9,** nwac123 (2022).

178. Domhan, T., Springenberg, J. T., Hutter, F., *et al. Speeding up automatic hyperparameter optimization of deep neural networks by extrapolation of learning curves.* in *IJCAI* **15** (2015), 3460–8.

179. Montavon, G. in *Machine learning meets quantum physics* 37–62 (Springer, 2020).

180. Bergen, K. J., Johnson, P. A., de Hoop, M. V. & Beroza, G. C. Machine learning for data-driven discovery in solid Earth geoscience. *Science* **363,** eaau0323 (2019).

181. Raissi, M., Perdikaris, P. & Karniadakis, G. E. Physics-informed neural networks: A deep learning framework for solving forward and inverse problems involving nonlinear partial differential equations. *Journal of Computational physics* **378,** 686–707 (2019).

182. Milanković, M., Benny, B. & Meroz, I. Canon of insolation and the ice-age problem:(Kanon der Erdbestrahlung und seine Anwendung auf das Eiszeitenproblem) Belgrade, 1941. *(No Title)* (1969).

183. Denton, G. H. & Hughes, T. J. Milankovitch theory of ice ages: Hypothesis of ice-sheet linkage between regional insolation and global climate. *Quaternary Research* **20,** 125–144 (1983).

184. Huybers, P. & Denton, G. Antarctic temperature at orbital timescales controlled by local summer duration. *Nature Geoscience* **1,** 787–792 (2008).

185. Clark, P. U. *et al.* The middle Pleistocene transition: characteristics, mechanisms, and implications for long-term changes in atmospheric pCO2. *Quaternary Science Reviews* **25,** 3150–3184 (2006).

186. Lisiecki, L. E. Links between eccentricity forcing and the 100,000-year glacial cycle. *Nature geoscience* **3,** 349–352 (2010).

187. Stott, L. Glacial terminations or glacial interruptions? *Earth-Science Reviews* **252,** 104756 (2024).

188. Imbrie, J. *et al.* On the structure and origin of major glaciation cycles 2. The 100,000-year cycle. *Paleoceanography* **8,** 699–735 (1993).

189. Nie, J., King, J. & Fang, X. Late Pliocene-early Pleistocene 100-ka problem. *Geophysical Research Letters* **35** (2008).

190. Berends, C., Köhler, P., Lourens, L. & Van de Wal, R. *On the cause of the mid-Pleistocene transition* 2021.

191. Gildor, H. & Tziperman, E. A sea ice climate switch mechanism for the 100-kyr glacial cycles. *Journal of Geophysical Research: Oceans* **106,** 9117–9133 (2001).

192. Bintanja, R. & Van de Wal, R. North American ice-sheet dynamics and the onset of 100,000-year glacial cycles. *Nature* **454,** 869–872 (2008).

193. Zeng, N. Quasi-100 ky glacial-interglacial cycles triggered by subglacial burial carbon release. *Climate of the Past* **3,** 135–153 (2007).

194. Farmer, J. *et al.* Deep Atlantic Ocean carbon storage and the rise of 100,000-year glacial cycles. *Nature Geoscience* **12,** 355–360 (2019).

195. Praetorius, S. *et al.* Interaction between climate, volcanism, and isostatic rebound in Southeast Alaska during the last deglaciation. *Earth and Planetary Science Letters* **452,** 79–89 (2016).

196. Sternai, P., Caricchi, L., Castelltort, S. & Champagnac, J.-D. Deglaciation and glacial erosion: A joint control on magma productivity by continental unloading. *Geophysical Research Letters* **43,** 1632–1641 (2016).

197. Armitage, J. J., Ferguson, D. J., Petersen, K. D. & Creyts, T. T. The importance of Icelandic ice sheet growth and retreat on mantle CO2 flux. *Geophysical Research Letters* **46,** 6451–6458 (2019).

198. Cabaniss, H. E., Gregg, P. M. & Grosfils, E. B. The role of tectonic stress in triggering large silicic caldera eruptions. *Geophysical Research Letters* **45,** 3889–3895 (2018).

199. Lucas, L. C., Albright, J. A., Gregg, P. M. & Zhan, Y. The impact of ice caps on the mechanical stability of magmatic systems: implications for forecasting on human timescales. *Frontiers in Earth Science* **10,** 868569 (2022).

200. Jellinek, A. M., Manga, M. & Saar, M. O. Did melting glaciers cause volcanic eruptions in eastern California? Probing the mechanics of dike formation. *Journal of Geophysical Research: Solid Earth* **109** (2004).

201. Beaulieu, E., Goddéris, Y., Donnadieu, Y., Labat, D. & Roelandt, C. High sensitivity of the continental-weathering carbon dioxide sink to future climate change. *Nature Climate Change* **2,** 346–349 (2012).

202. Yu, Z., Colin, C., Bassinot, F., Wan, S. & Bayon, G. Climate-driven weathering shifts between highlands and floodplains. *Geochemistry, Geophysics, Geosystems* **21,** e2020GC008936 (2020).

203. Barth, A. M., Clark, P. U., Bill, N. S., He, F. & Pisias, N. G. Climate evolution across the Mid-Brunhes transition. *Climate of the Past* **14,** 2071–2087 (2018).

204. Broecker, W. S. & Denton, G. H. What drives glacial cycles? *Scientific American* **262,** 48–43 (1990).

205. Jansen, J., Kuijpers, A. & Troelstra, S. A mid-Brunhes climatic event: Long-term changes in global atmosphere and ocean circulation. *Science* **232,** 619–622 (1986).

206. Spratt, R. M. & Lisiecki, L. E. A Late Pleistocene sea level stack. *Climate of the Past* **12,** 1079–1092 (2016).

207. Xu, X. *et al.* Records of the Mid-Brunhes Event in Chinese loess-paleosol sequences. *Palaeogeography, Palaeoclimatology, Palaeoecology* **543,** 109596 (2020).

208. Ao, H. *et al.* Two-stage mid-Brunhes climate transition and mid-Pleistocene human diversification. *Earth-Science Reviews* **210,** 103354 (2020).

209. Belmaker, M. in *Sourcebook of Paleolithic transitions: Methods, theories, and interpretations* 211–227 (Springer, 2009).

210. Holden, P., Edwards, N., Wolff, E. W., Valdes, P. J. & Singarayer, J. S. The Mid-Brunhes event and West Antarctic ice sheet stability. *Journal of Quaternary Science* **26,** 474–477 (2011).

211. Kemp, A., Grigorov, I., Pearce, R. B. & Garabato, A. N. Migration of the Antarctic Polar Front through the mid-Pleistocene transition: evidence and climatic implications. *Quaternary Science Reviews* **29,** 1993–2009 (2010).

212. Meng, X. *et al.* Significant influence of Northern Hemisphere high latitude climate on appeared precession rhythm of East Asian summer monsoon after Mid-Brunhes Transition interglacials recorded in the Chinese loess. *Catena* **197,** 105002 (2021).

213. Köhler, P. & Fischer, H. Simulating low frequency changes in atmospheric CO 2 during the last 740 000 years. *Climate of the Past* **2,** 57–78 (2006).

214. Mitsui, T. & Boers, N. Machine learning approach reveals strong link between obliquity amplitude increase and the Mid-Brunhes transition. *Quaternary Science Reviews* **277,** 107344 (2022).

215. Dommenget, D. & Rezny, M. A caveat note on tuning in the development of coupled climate models. *Journal of Advances in Modeling Earth Systems* **10,** 78–97 (2018).

216. Masson-Delmotte, V. *et al.* EPICA Dome C record of glacial and interglacial intensities. *Quaternary Science Reviews* **29,** 113–128 (2010).

217. Liro, C. R., Adams, E. E. & Herzog, H. J. Modeling the release of CO2 in the deep ocean. *Energy Conversion and Management* **33,** 667–674 (1992).

218. Lawrence, K. T., Herbert, T. D., Brown, C. M., Raymo, M. E. & Haywood, A. M. High-amplitude variations in North Atlantic sea surface temperature during the early Pliocene warm period. *Paleoceanography* **24** (2009).

219. Herbert, T. D., Peterson, L. C., Lawrence, K. T. & Liu, Z. Tropical ocean temperatures over the past 3.5 million years. *science* **328,** 1530–1534 (2010).

220. Lambert, F. *et al.* Dust-climate couplings over the past 800,000 years from the EPICA Dome C ice core. *Nature* **452,** 616–619 (2008).

221. Knutti, R., Flückiger, J., Stocker, T. & Timmermann, A. Strong hemispheric coupling of glacial climate through freshwater discharge and ocean circulation. *Nature* **430,** 851–856 (2004).

222. Holden, P. *et al.* Interhemispheric coupling, the West Antarctic ice sheet and warm Antarctic interglacials. *Climate of the Past* **6,** 431–443 (2010).

223. Barker, S. *et al.* 800,000 years of abrupt climate variability. *science* **334,** 347–351 (2011).

224. Cronin, T. M. *et al.* Enhanced Arctic amplification began at the Mid-Brunhes Event˜ 400,000 years ago. *Scientific Reports* **7,** 14475 (2017).

225. Grinsted, A., Moore, J. C. & Jevrejeva, S. Application of the cross wavelet transform and wavelet coherence to geophysical time series. *Nonlinear processes in geophysics* **11,** 561–566 (2004).

226. Kutterolf, S. *et al.* A detection of Milankovitch frequencies in global volcanic activity. *Geology* **41,** 227–230 (2013).

227. Köhler, P. & Munhoven, G. Late Pleistocene carbon cycle revisited by considering solid Earth processes. *Paleoceanography and Paleoclimatology* **35,** e2020PA004020 (2020).

228. Sottili, G. & Palladino, D. M. When volcanoes record Milankovitch cycles. *Frontiers in Earth Science* **13,** 1569128 (2025).

229. Sternai, P. in *Dynamics of plate tectonics and mantle convection* 271–294 (Elsevier, 2023).

230. Maclennan, J., Jull, M., McKenzie, D., Slater, L. & Grönvold, K. The link between volcanism and deglaciation in Iceland. *Geochemistry, Geophysics, Geosystems* **3,** 1–25 (2002).

231. Burley, J. M. *Magmatism and glacial cycles: coupled oscillations?* (University of Oxford (United Kingdom), 2017).

232. Cerpa, N. G., Jones, D. W. R. & Katz, R. F. Consequences of glacial cycles for magmatism and carbon transport at mid-ocean ridges. *Earth and Planetary Science Letters* **528,** 115845 (2019).

233. Thatcher, W. & Hill, D. P. A simple model for the fault-generated morphology of slow-spreading mid-oceanic ridges. *Journal of Geophysical Research: Solid Earth* **100,** 561–570 (1995).

234. Karson, J. *et al.* Along-axis variations in seafloor spreading in the MARK area. *Nature* **328,** 681–685 (1987).

235. Huybers, P. *et al.* Influence of late Pleistocene sea-level variations on midocean ridge spacing in faulting simulations and a global analysis of bathymetry. *Proceedings of the National Academy of Sciences* **119,** e2204761119 (2022).

236. Boulahanis, B. *et al.* Do sea level variations influence mid-ocean ridge magma supply? A test using crustal thickness and bathymetry data from the East Pacific Rise. *Earth and Planetary Science Letters* **535,** 116121 (2020).

237. Cerling, T. E., Ehleringer, J. R. & Harris, J. M. Carbon dioxide starvation, the development of C4 ecosystems, and mammalian evolution. *Philosophical Transactions of the Royal Society of London. Series B: Biological Sciences* **353,** 159–171 (1998).

238. Boutin, S. & Lane, J. E. Climate change and mammals: evolutionary versus plastic responses. *Evolutionary applications* **7,** 29–41 (2014).

239. Erwin, D. H. Climate as a driver of evolutionary change. *Current Biology* **19,** R575–R583 (2009).

240. Tierney, J. E. *et al.* Spatial patterns of climate change across the Paleocene–Eocene Thermal Maximum. *Proceedings of the national academy of sciences* **119,** e2205326119 (2022).

241. Steinthorsdottir, M. *et al.* The Miocene: The future of the past. *Paleoceanography and Paleoclimatology* **36,** e2020PA004037 (2021).

242. Foster, G. L., Hull, P., Lunt, D. J. & Zachos, J. C. *Placing our current 'hyperthermal'in the context of rapid climate change in our geological past* 2018.

243. Steinhorsdottir, M., Jardine, P. & Rember, W. Near-future pCO2 during the hot Miocene climatic optimum. *Paleoceanography and Paleoclimatology* **36,** e2020–PA003900 (2021).

244. Guo, Z., Wilson, M., Dingwell, D. B. & Liu, J. India-Asia collision as a driver of atmospheric CO2 in the Cenozoic. *Nature Communications* **12,** 3891 (2021).

245. Zachos, J. C. *et al.* Rapid acidification of the ocean during the Paleocene-Eocene thermal maximum. *science* **308,** 1611–1615 (2005).

246. Anagnostou, E. *et al.* Changing atmospheric CO2 concentration was the primary driver of early Cenozoic climate. *Nature* **533,** 380–384 (2016).

247. Henehan, M. J. *et al.* Revisiting the Middle Eocene Climatic Optimum "Carbon Cycle Conundrum" with new estimates of atmospheric pCO2 from boron isotopes. *Paleoceanography and Paleoclimatology* **35,** e2019PA003713 (2020).

248. Mudelsee, M., Bickert, T., Lear, C. H. & Lohmann, G. Cenozoic climate changes: A review based on time series analysis of marine benthic δ18O records. *Reviews of Geophysics* **52,** 333–374 (2014).

249. Consortium*†, C. C. P. I. P. (*et al.* Toward a Cenozoic history of atmospheric CO2. *Science* **382,** eadi5177 (2023).

250. Müller, R. D. *et al.* Evolution of Earth's tectonic carbon conveyor belt. *Nature* **605,** 629–639 (2022).

251. Goddéris, Y., Donnadieu, Y. & Mills, B. What models tell us about the evolution of carbon sources and sinks over the Phanerozoic. *Annual Review of Earth and Planetary Sciences* **51,** 471–492 (2023).

252. Berner, R. A. & Kothavala, Z. GEOCARB III: a revised model of atmospheric CO 2 over Phanerozoic time. *American Journal of Science* **301,** 182–204 (2001).

253. Lenton, T. M., Daines, S. J. & Mills, B. J. COPSE reloaded: an improved model of biogeochemical cycling over Phanerozoic time. *Earth-Science Reviews* **178,** 1–28 (2018).

254. Birks, H. H. & Birks, H. J. B. Multi-proxy studies in palaeolimnology. *Vegetation history and Archaeobotany* **15,** 235–251 (2006).

255. Schroeter, N. *et al.* How to deal with multi-proxy data for paleoenvironmental reconstructions: Applications to a Holocene lake sediment record from the Tian Shan, Central Asia. *Frontiers in Earth Science* **8,** 353 (2020).

256. Emiliani, C. Pleistocene temperatures. *The Journal of geology* **63,** 538–578 (1955).

257. Hansen, J. E. *et al.* Global warming in the pipeline. *Oxford Open Climate Change* **3,** kgad008 (2023).

258. Westerhold, T. *et al.* An astronomically dated record of Earth's climate and its predictability over the last 66 million years. *science* **369,** 1383–1387 (2020).

259. Sen, G. Generation of Deccan trap magmas. *Journal of Earth System Science* **110,** 409–431 (2001).

260. Gutjahr, M. *et al.* Very large release of mostly volcanic carbon during the Palaeocene–Eocene Thermal Maximum. *Nature* **548,** 573–577 (2017).

261. Oglesby, R. J. A GCM study of Antarctic glaciation. *Climate Dynamics* **3,** 135–156 (1989).

262. Hodel, F. *et al.* Drake Passage gateway opening and Antarctic Circumpolar Current onset 31 Ma ago: The message of foraminifera and reconsideration of the Neodymium isotope record. *Chemical Geology* **570,** 120171 (2021).

263. Livermore, R., Nankivell, A., Eagles, G. & Morris, P. Paleogene opening of Drake passage. *Earth and Planetary Science Letters* **236,** 459–470 (2005).

264. Coxall, H. K., Wilson, P. A., Pälike, H., Lear, C. H. & Backman, J. Rapid stepwise onset of Antarctic glaciation and deeper calcite compensation in the Pacific Ocean. *Nature* **433,** 53–57 (2005).

265. Thorn, V. C. & DeConto, R. Antarctic climate at the Eocene/Oligocene boundary—climate model sensitivity to high latitude vegetation type and comparisons with the palaeobotanical record. *Palaeogeography, Palaeoclimatology, Palaeoecology* **231,** 134–157 (2006).

266. Mills, B., Daines, S. J. & Lenton, T. M. Changing tectonic controls on the long-term carbon cycle from M esozoic to present. *Geochemistry, Geophysics, Geosystems* **15,** 4866–4884 (2014).

267. Pagani, M. *et al.* The role of carbon dioxide during the onset of Antarctic glaciation. *science* **334,** 1261–1264 (2011).

268. McKenzie, N. R. *et al.* Continental arc volcanism as the principal driver of icehouse-greenhouse variability. *Science* **352,** 444–447 (2016).

269. Seton, M. *et al.* Global continental and ocean basin reconstructions since 200 Ma. *Earth-Science Reviews* **113,** 212–270 (2012).

270. Hoareau, G. *et al.* Did high Neo-Tethys subduction rates contribute to early Cenozoic warming? *Climate of the Past* **11,** 1751–1767 (2015).

271. Yin, A. & Harrison, T. M. Geologic evolution of the Himalayan-Tibetan orogen. *Annual review of earth and planetary sciences* **28,** 211–280 (2000).

272. Storey, M., Duncan, R. A. & Swisher III, C. C. Paleocene-Eocene thermal maximum and the opening of the northeast Atlantic. *Science* **316,** 587–589 (2007).

273. Boschman, L. M., van Hinsbergen, D. J., Torsvik, T. H., Spakman, W. & Pindell, J. L. Kinematic reconstruction of the Caribbean region since the Early Jurassic. *Earth-Science Reviews* **138,** 102–136 (2014).

274. Gans, P. B. *Synextensional magmatism in the Basin and Range province: A case study from the eastern Great Basin* (Geological Society of America, 1989).

275. Vaes, B., Van Hinsbergen, D. J. & Boschman, L. M. Reconstruction of subduction and back-arc spreading in the NW Pacific and Aleutian Basin: Clues to causes of Cretaceous and Eocene plate reorganizations. *Tectonics* **38,** 1367–1413 (2019).

276. Yamanouchi, T. & Charlock, T. P. Effects of clouds, ice sheet, and sea ice on the Earth radiation budget in the Antarctic. *Journal of Geophysical Research: Atmospheres* **102,** 6953–6970 (1997).

277. Ding, L. *et al.* Timing and mechanisms of Tibetan Plateau uplift. *Nature Reviews earth & environment* **3,** 652–667 (2022).

278. Hay, W. W., Soeding, E., DeConto, R. M. & Wold, C. N. The Late Cenozoic uplift–climate change paradox. *International Journal of Earth Sciences* **91,** 746–774 (2002).

279. Persico, D. & Villa, G. Eocene–Oligocene calcareous nannofossils from Maud Rise and Kerguelen Plateau (Antarctica): paleoecological and paleoceanographic implications. *Marine Micropaleontology* **52,** 153–179 (2004).

280. Lear, C. H., Elderfield, H. & Wilson, P. A Cenozoic seawater Sr/Ca record from benthic foraminiferal calcite and its application in determining global weathering fluxes. *Earth and Planetary Science Letters* **208,** 69–84 (2003).

281. Longman, J., Mills, B. J., Donnadieu, Y. & Goddéris, Y. Assessing volcanic controls on Miocene climate change. *Geophysical Research Letters* **49,** e2021GL096519 (2022).

282. De Leeuw, A., Bukowski, K., Krijgsman, W. & Kuiper, K. F. Age of the Badenian salinity crisis; impact of Miocene climate variability on the circum-Mediterranean region. *Geology* **38,** 715–718 (2010).

283. Haywood, A. M. *et al.* Are there pre-Quaternary geological analogues for a future greenhouse warming? *Philosophical Transactions of the Royal Society A: Mathematical, Physical and Engineering Sciences* **369,** 933–956 (2011).

284. Scotese, C. R. An atlas of Phanerozoic paleogeographic maps: the seas come in and the seas go out. *Annual Review of Earth and Planetary Sciences* **49,** 679–728 (2021).

285. Saltzman, M. R. Silicate weathering, volcanic degassing, and the climate tug of war. *Geology* **45,** 763–764 (2017).

286. Kasting, J. F. The Goldilocks planet? How silicate weathering maintains Earth "just right". *Elements: An International Magazine of Mineralogy, Geochemistry, and Petrology* **15,** 235–240 (2019).

287. Macdonald, F. A., Swanson-Hysell, N. L., Park, Y., Lisiecki, L. & Jagoutz, O. Arc-continent collisions in the tropics set Earth's climate state. *Science* **364,** 181–184 (2019).

288. Lee, C.-T. A. *et al.* Continental arc–island arc fluctuations, growth of crustal carbonates, and long-term climate change. *Geosphere* **9,** 21–36 (2013).

289. Jagoutz, O., Macdonald, F. A. & Royden, L. Low-latitude arc–continent collision as a driver for global cooling. *Proceedings of the National Academy of Sciences* **113,** 4935–4940 (2016).

290. Brune, S., Williams, S. E. & Müller, R. D. Potential links between continental rifting, CO2 degassing and climate change through time. *Nature Geoscience* **10,** 941–946 (2017).

291. Ernst, R. E. & Youbi, N. How Large Igneous Provinces affect global climate, sometimes cause mass extinctions, and represent natural markers in the geological record. *Palaeogeography, palaeoclimatology, palaeoecology* **478,** 30–52 (2017).

292. Lacis, A. A., Schmidt, G. A., Rind, D. & Ruedy, R. A. Atmospheric CO2: Principal control knob governing Earth's temperature. *Science* **330,** 356–359 (2010).

293. Lee, C.-T. A., Jiang, H., Dasgupta, R. & Torres, M. A framework for understanding whole-Earth carbon cycling (2019).

294. Tian, L. *et al.* Phanerozoic oceanic and climatic perturbations in the context of Tethyan evolution. *Science China Earth Sciences* **66,** 2791–2806 (2023).

295. Cao, W., Lee, C.-T. A. & Lackey, J. S. Episodic nature of continental arc activity since 750 Ma: A global compilation. *Earth and Planetary Science Letters* **461,** 85–95 (2017).

296. Merdith, A. S., Williams, S. E., Brune, S., Collins, A. S. & Müller, R. D. Rift and plate boundary evolution across two supercontinent cycles. *Global and planetary change* **173,** 1–14 (2019).

297. Müller, R. D. *et al.* A global plate model including lithospheric deformation along major rifts and orogens since the Triassic. *Tectonics* **38,** 1884–1907 (2019).

298. Nance, R. D., Murphy, J. B. & Santosh, M. The supercontinent cycle: a retrospective essay. *Gondwana Research* **25,** 4–29 (2014).

299. Zaffos, A., Finnegan, S. & Peters, S. E. Plate tectonic regulation of global marine animal diversity. *Proceedings of the National Academy of Sciences* **114,** 5653–5658 (2017).

300. Royer, D. L., Berner, R. A., Montañez, I. P., Tabor, N. J., Beerling, D. J., *et al.* Co˜ 2 as a primary driver of phanerozoic climate. *GSA today* **14,** 4–10 (2004).

301. Hansen, J., Sato, M., Russell, G. & Kharecha, P. Climate sensitivity, sea level and atmospheric carbon dioxide. *Philosophical Transactions of the Royal Society A: Mathematical, Physical and Engineering Sciences* **371,** 20120294 (2013).

302. Lee, H. *et al.* Massive and prolonged deep carbon emissions associated with continental rifting. *Nature Geoscience* **9,** 145–149 (2016).

303. Berner, R. A. Models for carbon and sulfur cycles and atmospheric oxygen; application to Paleozoic geologic history. *American Journal of Science* **287,** 177–196 (1987).

304. Berner, R. A. A model for atmospheric CO sub 2 over phanerozoic time. *American Journal of Science;(United States)* **291** (1991).

305. Mills, B. J. *et al.* Modelling the long-term carbon cycle, atmospheric CO2, and Earth surface temperature from late Neoproterozoic to present day. *Gondwana Research* **67,** 172–186 (2019).

306. Falkowski, P. G. *et al.* The rise of oxygen over the past 205 million years and the evolution of large placental mammals. *Science* **309,** 2202–2204 (2005).

307. Arvidson, R. S., Mackenzie, F. T. & Guidry, M. W. Geologic history of seawater: a MAGic approach to carbon chemistry and ocean ventilation. *Chemical Geology* **362,** 287–304 (2013).

308. Royer, D. L. Atmospheric CO2 and O2 during the Phanerozoic: Tools, patterns, and impacts. *Treatise on geochemistry,* 251–267 (2014).

309. Mills, B. J., Belcher, C. M., Lenton, T. M. & Newton, R. J. A modeling case for high atmospheric oxygen concentrations during the Mesozoic and Cenozoic. *Geology* **44,** 1023–1026 (2016).

310. Foster, G. L., Royer, D. L. & Lunt, D. J. Future climate forcing potentially without precedent in the last 420 million years. *Nature communications* **8,** 14845 (2017).

311. Krause, A. *et al.* Large uncertainty in carbon uptake potential of land-based climate-change mitigation efforts. *Global Change Biology* **24,** 3025–3038 (2018).

312. Schachat, S. R. *et al.* Phanerozoic p O2 and the early evolution of terrestrial animals. *Proceedings of the Royal Society B: Biological Sciences* **285,** 20172631 (2018).

313. Miller, K. G. *et al.* Cenozoic sea-level and cryospheric evolution from deep-sea geochemical and continental margin records. *Science advances* **6,** eaaz1346 (2020).

314. Misra, S. & Froelich, P. N. Lithium isotope history of Cenozoic seawater: changes in silicate weathering and reverse weathering. *science* **335,** 818–823 (2012).

315. Crowley, T. Significance of tectonic boundary conditions for paleoclimate simulations. *Oxford Monographs on Geology and Geophysics* **39,** 3–20 (1998).

316. Cather, S. M., Dunbar, N. W., McDowell, F. W., McIntosh, W. C. & Scholle, P. A. Climate forcing by iron fertilization from repeated ignimbrite eruptions: The icehouse–silicic large igneous province (SLIP) hypothesis. *Geosphere* **5,** 315–324 (2009).

317. Van Der Meer, D. G. *et al.* Plate tectonic controls on atmospheric CO2 levels since the Triassic. *Proceedings of the National Academy of Sciences* **111,** 4380–4385 (2014).

318. Rowley, D. B. Rate of plate creation and destruction: 180 Ma to present. *Geological Society of America Bulletin* **114,** 927–933 (2002).

319. Coltice, N., Seton, M., Rolf, T., Müller, R. D. & Tackley, P. J. Convergence of tectonic reconstructions and mantle convection models for significant fluctuations in seafloor spreading. *Earth and Planetary Science Letters* **383,** 92–100 (2013).

320. Voosen, P. *Slowdown in plate tectonics may have led to ice sheets* 2021.

321. Williams, S., Wright, N. M., Cannon, J., Flament, N. & Müller, R. D. Reconstructing seafloor age distributions in lost ocean basins. *Geoscience Frontiers* **12,** 769–780 (2021).

322. Marty, B. & Tolstikhin, I. N. CO2 fluxes from mid-ocean ridges, arcs and plumes. *Chemical Geology* **145,** 233–248 (1998).

323. Cogné, J.-P. & Humler, E. Temporal variation of oceanic spreading and crustal production rates during the last 180 My. *Earth and Planetary Science Letters* **227,** 427–439 (2004).

324. Seton, M., Gaina, C., Müller, R. & Heine, C. Mid-Cretaceous seafloor spreading pulse: Fact or fiction? *Geology* **37,** 687–690 (2009).

325. Johnston, F. K., Turchyn, A. V. & Edmonds, M. Decarbonation efficiency in subduction zones: Implications for warm Cretaceous climates. *Earth and Planetary Science Letters* **303,** 143–152 (2011).

326. Burton, M. R., Sawyer, G. M. & Granieri, D. Deep carbon emissions from volcanoes. *Reviews in Mineralogy and Geochemistry* **75,** 323–354 (2013).

327. Dasgupta, R. Ingassing, storage, and outgassing of terrestrial carbon through geologic time. *Reviews in Mineralogy and Geochemistry* **75,** 183–229 (2013).

328. Lee, C.-T. A. & Lackey, J. S. Global continental arc flare-ups and their relation to long-term greenhouse conditions. *Elements* **11,** 125–130 (2015).

329. Marcilly, C. M., Torsvik, T. H., Domeier, M. & Royer, D. L. New paleogeographic and degassing parameters for long-term carbon cycle models. *Gondwana Research* **97,** 176–203 (2021).

330. O'Neill, C., Lenardic, A. & Condie, K. Earth's punctuated tectonic evolution: cause and effect (2015).

331. Hilton, R. G. & West, A. J. Mountains, erosion and the carbon cycle. *Nature Reviews Earth & Environment* **1,** 284–299 (2020).

332. Ebinger, C. & Scholz, C. A. Continental rift basins: the East African perspective. *Tectonics of sedimentary basins: Recent advances,* 183–208 (2011).

333. Foley, S. F. & Fischer, T. P. An essential role for continental rifts and lithosphere in the deep carbon cycle. *Nature Geoscience* **10,** 897–902 (2017).

334. Garzanti, E. *et al.* Weathering and relative durability of detrital minerals in equatorial climate: sand petrology and geochemistry in the East African Rift. *The Journal of Geology* **121,** 547–580 (2013).

335. Sternai, P. *et al.* Effects of asthenospheric flow and orographic precipitation on continental rifting. *Tectonophysics* **820,** 229120 (2021).

336. Fioraso, M. *et al.* Miocene climate cooling and aridification of Antarctica may have enhanced syn-extensional magmatism in the western Ross Sea. *Global and Planetary Change* **240,** 104538 (2024).

337. Youbi, N. *et al.* Preliminary appraisal of a correlation between glaciations and large igneous provinces over the past 720 million years. *Large Igneous Provinces: A driver of global environmental and biotic changes,* 169–190 (2021).

338. Frings, P. J. Palaeoweathering: how do weathering rates vary with climate? *Elements: An International Magazine of Mineralogy, Geochemistry, and Petrology* **15,** 259–265 (2019).

339. Park, Y., Swanson-Hysell, N. L., Lisiecki, L. E. & Macdonald, F. A. Evaluating the relationship between the area and latitude of large igneous provinces and Earth's long-term climate state. *Large igneous provinces: A driver of global environmental and biotic changes,* 153–168 (2021).

340. Svensen, H. *et al.* Release of methane from a volcanic basin as a mechanism for initial Eocene global warming. *Nature* **429,** 542–545 (2004).

341. He, T., Kemp, D. B., Li, J. & Ruhl, M. Paleoenvironmental changes across the Mesozoic–Paleogene hyperthermal events. *Global and Planetary Change* **222,** 104058 (2023).

342. Boulila, S., Laskar, J., Haq, B. U., Galbrun, B. & Hara, N. Long-term cyclicities in Phanerozoic sea-level sedimentary record and their potential drivers. *Global and Planetary Change* **165,** 128–136 (2018).

343. Zhang, R. *et al.* Long-term cycles of the Solar System concealed in the Mesozoic sedimentary basin record. *Science China Earth Sciences* **66,** 358–376 (2023).

344. Jellinek, A., Lenardic, A. & Pierrehumbert, R. Ice, fire, or fizzle: The climate footprint of Earth's supercontinental cycles. *Geochemistry, Geophysics, Geosystems* **21,** e2019GC008464 (2020).

345. Nance, R. D. The supercontinent cycle and Earth's long-term climate. *Annals of the New York Academy of Sciences* **1515,** 33–49 (2022).

346. Farnsworth, A. *et al.* Climate extremes likely to drive land mammal extinction during next supercontinent assembly. *Nature Geoscience* **16,** 901–908 (2023).

347. Lenton, T. M., Crouch, M., Johnson, M., Pires, N. & Dolan, L. First plants cooled the Ordovician. *Nature Geoscience* **5,** 86–89 (2012).

348. Wang, R. *et al.* The coupling of Phanerozoic continental weathering and marine phosphorus cycle. *Scientific reports* **10,** 5794 (2020).

349. Merdith, A. S. *et al.* Extending full-plate tectonic models into deep time: Linking the Neoproterozoic and the Phanerozoic. *Earth-Science Reviews* **214,** 103477 (2021).

350. Agard, P. *et al.* Slabitization: Mechanisms controlling subduction development and viscous coupling. *Earth-Science Reviews* **208,** 103259 (2020).

351. Krissansen-Totton, J. & Catling, D. C. Constraining climate sensitivity and continental versus seafloor weathering using an inverse geological carbon cycle model. *Nature communications* **8,** 15423 (2017).

352. Wright, N. M., Seton, M., Williams, S. E., Whittaker, J. M. & Müller, R. D. Sea-level fluctuations driven by changes in global ocean basin volume following supercontinent break-up. *Earth-Science Reviews* **208,** 103293 (2020).

353. Korchinski, M., Teyssier, C., Rey, P. F., Whitney, D. L. & Mondy, L. Single-phase vs two-phase rifting: Numerical perspectives on the accommodation of extension during continental break-up. *Marine and Petroleum Geology* **123,** 104715 (2021).